

mean difference for all rubric score elements was rejected. Univariate statistical tests of the observed mean differences between the teaching-and-research and research-only conditions indicated significant results for the rubric score elements “testability of hypotheses” [mean difference = 0.272, $P = 0.006$; CI = (.106, 0.526)] with the null hypothesis rejected in 99.3% of generated data samples (Fig. 1) and “research/experimental design” [mean difference = 0.317, $P = 0.002$; CI = (.106, 0.522)] with the null hypothesis rejected in 100% of generated data samples (Fig. 2).

These findings indicate a medium effect size for teaching and research experiences’ impact on participants’ abilities to generate testable hypotheses (Cohen’s $d = 0.40$) and valid research designs (Cohen’s $d = 0.478$) in the context of written research proposals (27.4 and 32.9% nonoverlap between teaching-and-research and research-only distributions for hypotheses and experimental design, respectively) (27). Differences in overall writing quality cannot account for the observed effects because only specific skills showed differential outcomes as a function of experience type.

These data provide direct, performance-based evidence of improvement on specific research skills associated with teaching experiences that complement traditional graduate research training. As such, they hold substantial implications for both the programmatic graduate training in STEM and the challenges that universities face as they strive to meet increased demand for instruction with fewer resources. The reframing of teaching experience as a value-added component of graduate research training suggests several substantial changes for the culture and practice of graduate education in STEM disciplines. Further, if teach-

ing becomes a more commonly supported facet of STEM graduate education then students’ instructional training and experiences would alleviate persistent concerns that current programs underprepare future STEM faculty to perform their teaching responsibilities (28, 29).

References and Notes

- W. A. Anderson *et al.*, *Science* **331**, 152 (2011).
- J. A. Bianchini, D. J. Whitney, T. D. Breton, B. A. Hilton-Brown, *Sci. Educ.* **86**, 42 (2001).
- C. E. Brawner, R. M. Felder, R. Allen, R. Brent, “1999–2000 SUCCEED Faculty Survey of Teaching Practices and Perceptions of Institutional Attitudes Toward Teaching” (ERIC Document Reproduction Service Report ED 461510, 2002).
- J. Robertson, C. H. Bond, *High. Educ. Res. Dev.* **20**, 5 (2001).
- A. E. Austin *et al.*, *N. Dir. Teach. Learn.* **117**, 83 (2009).
- D. H. Wulff, A. E. Austin, J. D. Nyquist, J. Sprague, in *Paths to the Professoriate: Strategies for Enriching the Preparation of Future Faculty*, D. H. Wulff, A. E. Austin, Eds. (Jossey-Bass, San Francisco, 2004), pp. 46–73.
- B. Berardi-Coletta, L. S. Buyer, R. L. Dominowski, E. R. Rellinger, *J. Exp. Psychol. Learn. Mem. Cogn.* **21**, 205 (1995).
- M. T. H. Chi, N. de Leeuw, M. H. Chiu, C. Lavancher, *Cogn. Sci.* **18**, 439 (1994).
- K. VanLehn, R. Jones, M. T. H. Chi, *J. Learn. Sci.* **2**, 1 (1992).
- S. L. Adamson *et al.*, *J. Res. Sci. Teach.* **40**, 939 (2003).
- S. Delamont, P. Atkinson, *Soc. Stud. Sci.* **31**, 87 (2001).
- D. French, C. Russell, *Bioscience* **52**, 1036 (2002).
- The NSF GK-12 program provides funding for graduate students in STEM disciplines so as to gain experiences teaching in K-12 classrooms during their degree programs—often by co-teaching with a full-time credentialed instructor.
- N. M. Trautmann, M. E. Krasny, *Bioscience* **56**, 159 (2006).
- V. L. Williams, “Merging University Students into K-12 Science Education Reform” (RAND, Santa Monica, CA, 2002).
- C. A. Ethington, A. Pisani, *Res. Higher Educ.* **34**, 343 (1993).
- R. E. Nisbett, T. D. Wilson, *Psychol. Rev.* **84**, 231 (1977).
- C. L. Townsend, E. Heit, *Mem. Cognit.* **39**, 204 (2011).
- D. F. Feldon, M. Maher, B. Timmerman, *Science* **329**, 282 (2010).
- B. Timmerman *et al.*, *Assess. Eval. High. Educ.* **36**, 509 (2011).
- No outcome differences were detected as a function of the type of teaching experience (TA or GK-12) within the sample population participating in both research and teaching.
- Materials and methods are available as supporting material on Science Online.
- R. L. Johnson, J. Penny, B. Gordon, *Appl. Meas. Educ.* **13**, 121 (2000).
- R. J. A. Little, *J. Am. Stat. Assoc.* **83**, 1198 (1988).
- C. K. Enders, *Applied Missing Data Analysis* (Guilford, New York, 2010).
- L. K. Muthén, B. O. Muthén, “Mplus User’s Guide” (UCLA, Los Angeles, ed. 6, 2010).
- J. Cohen, *Statistical Power Analysis for the Behavioral Sciences* (Erlbaum, Hillsdale, NJ), ed. 2, 1988.
- C. M. Golde, T. M. Dore, “At cross purposes: What the experiences of doctoral students reveal about doctoral education” (Pew Charitable Trusts, Philadelphia, 2001); www.phd-survey.org.
- A. S. Pruitt-Logan, J. G. Gaff, in *Paths to the Professoriate: Strategies for Enriching the Preparation of Future Faculty*, D. H. Wulff, A. E. Austin, Eds. (Jossey-Bass, San Francisco, 2004), pp.177–193.

Acknowledgments: This work is supported by a grant from the National Science Foundation to D.F., M.M., B.E.T., J. Lyons, and S. Thompson (NSF-0723686). The views expressed do not necessarily represent the views of the supporting funding agency. Data used to conduct the reported analyses can be found in (22).

Supporting Online Material

www.sciencemag.org/cgi/content/full/333/6045/1037/DC1
Materials and Methods
SOM Text
Figs. S1 to S4
Tables S1 to S5
Database S1

10 February 2011; accepted 21 June 2011
10.1126/science.1204109

Mutational Inactivation of *STAG2* Causes Aneuploidy in Human Cancer

David A. Solomon,¹ Taeyeon Kim,¹ Laura A. Diaz-Martinez,² Joshlean Fair,¹ Abdel G. Elkahoul,³ Brent T. Harris,⁴ Jeffrey A. Toretsky,¹ Steven A. Rosenberg,⁵ Neerav Shukla,⁶ Marc Ladanyi,⁶ Yardena Samuels,³ C. David James,⁷ Hongtao Yu,² Jung-Sik Kim,¹ Todd Waldman^{1*}

Most cancer cells are characterized by aneuploidy, an abnormal number of chromosomes. We have identified a clue to the mechanistic origins of aneuploidy through integrative genomic analyses of human tumors. A diverse range of tumor types were found to harbor deletions or inactivating mutations of *STAG2*, a gene encoding a subunit of the cohesin complex, which regulates the separation of sister chromatids during cell division. Because *STAG2* is on the X chromosome, its inactivation requires only a single mutational event. Studying a near-diploid human cell line with a stable karyotype, we found that targeted inactivation of *STAG2* led to chromatid cohesion defects and aneuploidy, whereas in two aneuploid human glioblastoma cell lines, targeted correction of the endogenous mutant alleles of *STAG2* led to enhanced chromosomal stability. Thus, genetic disruption of cohesin is a cause of aneuploidy in human cancer.

One of the hallmarks of cancer is chromosomal instability, which leads to aneuploidy, translocations, loss of heterozygosity, and other chromosomal aberrations (1, 2). Chromosomal instability is an early event in cancer

pathogenesis and is thought to generate the large number of genetic lesions required for a cell to undergo malignant transformation (3). It has been hypothesized that this instability is due to inactivating mutations in genes that control the mitotic

checkpoint and chromosome segregation (4, 5). However, in the vast majority of human tumors the molecular basis of chromosomal instability and the aneuploidy it produces remains unknown.

To explore this question, we followed up on previous studies in which we used Affymetrix 250K single-nucleotide polymorphism (SNP) arrays to identify novel regions of amplification and deletion in human glioblastoma cell lines (6–8). In U138MG cells, we identified a region

¹Department of Oncology, Lombardi Comprehensive Cancer Center, Georgetown University School of Medicine, Washington, DC 20057, USA. ²Howard Hughes Medical Institute and Department of Pharmacology, University of Texas Southwestern Medical Center, Dallas, TX 75390, USA. ³Cancer Genetics Branch, National Human Genome Research Institute, National Institutes of Health, Bethesda, MD 20892, USA. ⁴Departments of Neurology and Pathology, Georgetown University School of Medicine, Washington, DC 20057, USA. ⁵Surgery Branch, National Cancer Institute, National Institutes of Health, Bethesda, MD 20892, USA. ⁶Department of Pathology, Memorial Sloan-Kettering Cancer Center, New York, NY 10065, USA. ⁷Department of Neurological Surgery, Brain Tumor Research Center, Helen Diller Comprehensive Cancer Center, University of California at San Francisco, San Francisco, CA 94143, USA.

*To whom correspondence should be addressed. E-mail: waldmant@georgetown.edu

of genomic deletion on the X chromosome containing the “stromal antigen” *STAG2* gene (Fig. 1A and fig. S1). *STAG2* encodes a 141-kD subunit of cohesin, a multimeric protein complex that is required for cohesion of sister chromatids after DNA replication and that is cleaved at the metaphase-to-anaphase transition to enable chromosome segregation (5, 9, 10). Occasional deletions of chromosome Xq25 encompassing the *STAG2* locus have been observed in other cancer genome studies (11–13).

As expected, U138MG cells had no detectable *STAG2* protein (Fig. 1B). However, it was surprising that 42MGBA and H4 cells similarly lacked *STAG2* protein expression, despite no evidence of copy number loss by SNP microarray. To investigate whether point mutations might be responsible for the absence of *STAG2* expression in 42MGBA and H4 cells, we sequenced the 33 coding exons of *STAG2* and identified a 25–base pair (bp) insertion leading to frameshift in H4 cells and a nonsense mutation in 42MGBA cells (table S1 and fig. S2). We next sequenced the gene in 68 glioblastoma primary tumors and xenografts. These studies identified four additional mutations: a missense mutation in the stromalin conservative domain (SCD), a mutation of the canonical exon 9 splice acceptor, a 2-bp deletion causing a frame-

shift, and a point mutation in the exon 11 splice acceptor region (fig. S3).

Next, we performed Western blots on a panel of 135 additional human cancer cell lines from a variety of tumor types. This analysis identified 10 additional cell lines that had complete absence of *STAG2* expression (Fig. 1, C and D, and figs. S4 and S5). Sequencing of the *STAG2* gene revealed deletions or truncating mutations in 8 out of 10 of these samples (Fig. 1E and figs. S6 to S8). We then sequenced the *STAG2* gene in 48 melanoma and 24 Ewing’s sarcoma tumors and found a 6-bp insertion in the stromal antigen (STAG) domain and a point mutation 8 bp upstream of the initiating methionine (fig. S9). The mutations were somatic (i.e., tumor-specific) in all cases with available matched nonneoplastic tissue (table S1). Tumor-derived mutations in the *STAG2* gene caused aberrant localization of the protein product and altered chromatin association, consistent with functional inactivation (figs. S10 and S11). No mutations were identified in the *STAG2* paralog *STAG1*, nor was any compensatory up-regulation of *STAG1* detected in *STAG2*-deficient cells (fig. S12).

Four tumor samples harbored heterozygous mutations (table S1), despite complete absence of *STAG2* expression. Each of these samples was derived from a female patient, which suggested

that the remaining wild-type allele of *STAG2* was on the inactivated X chromosome. Sequencing of the *STAG2* mRNA from these four samples demonstrated that mRNA expression was derived exclusively from the mutant allele (Fig. 2A and fig. S8C). Treatment with the DNA methylase inhibitor 5-aza-2-deoxycytidine led to no reexpression of *STAG2* from the wild-type allele in TC-32 cells and only minimal reexpression in A4573 cells (fig. S13), which demonstrated that X chromosome inactivation (and not promoter methylation) was responsible for the “single-hit” inactivation of *STAG2* occurring in these tumors.

We next measured *STAG2* expression in diverse human primary tumor samples by immunohistochemistry. Details regarding experimental methods and validation of antibody specificity are in the Materials and Methods (8) and fig. S14 and S15. Robust *STAG2* expression was observed in all nonneoplastic tissues studied (fig. S16). In contrast, a significant fraction of glioblastomas, melanomas, and Ewing’s sarcomas had completely lost expression of *STAG2*, with occasional tumors demonstrating intratumoral heterogeneity (Fig. 2, B and C, and figs. S17 to S23). In tumors with *STAG2* loss, adjacent nonneoplastic stroma, perivascular endothelial cells, and infiltrating lymphocytes were uniformly *STAG2* positive (table

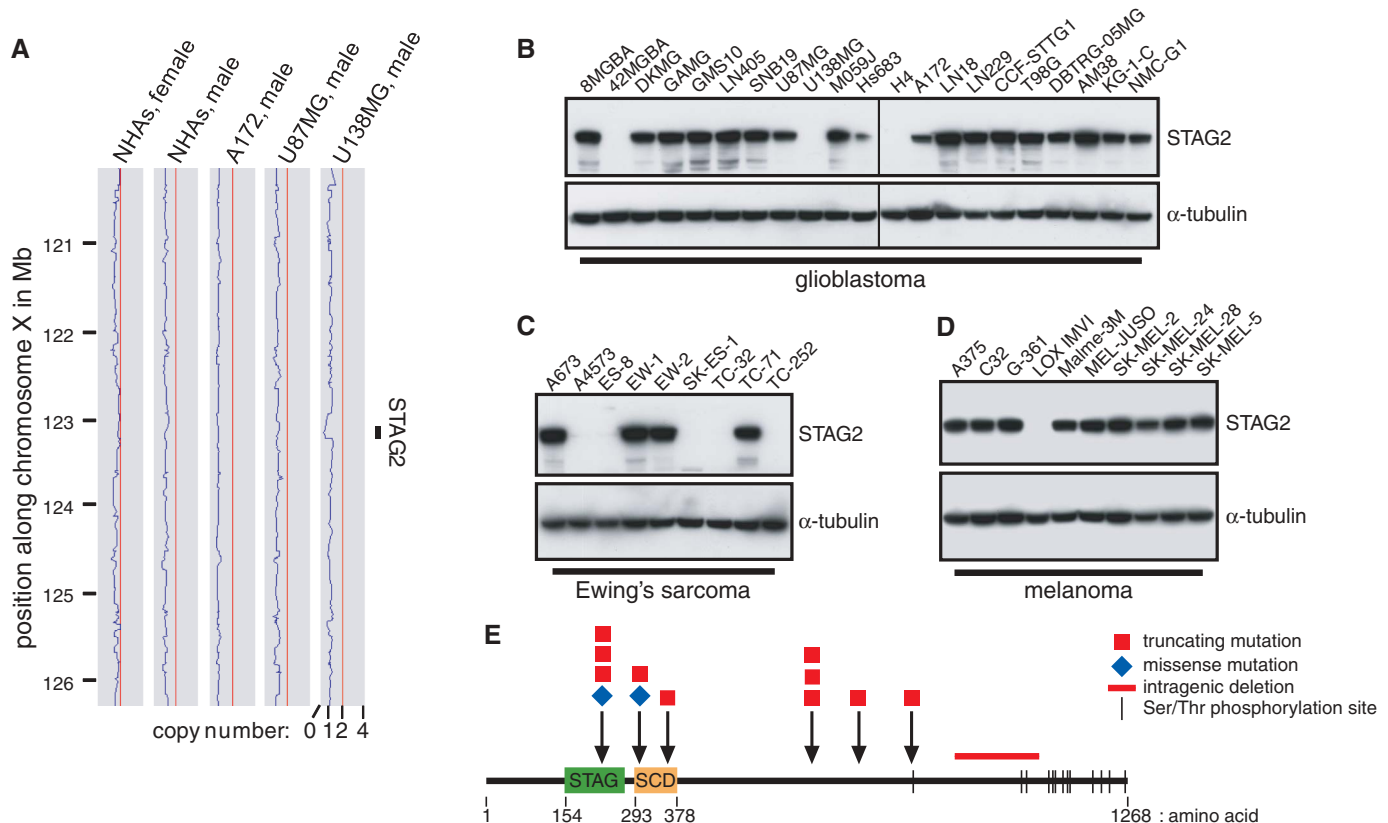


Fig. 1. *STAG2*, a gene encoding a subunit of cohesin—a protein complex that regulates sister chromatid separation during cell division—is frequently altered in diverse human cancers. **(A)** Copy-number plots along the X chromosome for normal human astrocytes (NHAs) and A172, U87MG, and U138MG glioblastoma cells. A genomic deletion between 122.930

and 123.226 Mb encompassing the *STAG2* gene is present in U138MG cells. **(B to D)** Western blots demonstrate complete loss of *STAG2* expression in 3 out of 21 glioblastoma, 5 out of 9 Ewing’s sarcoma, and 1 out of 10 melanoma cell lines. **(E)** Diagram of the *STAG2* protein with mutations identified.

S2), which further demonstrated the somatic nature of *STAG2* inactivation in a substantial fraction of primary human cancers.

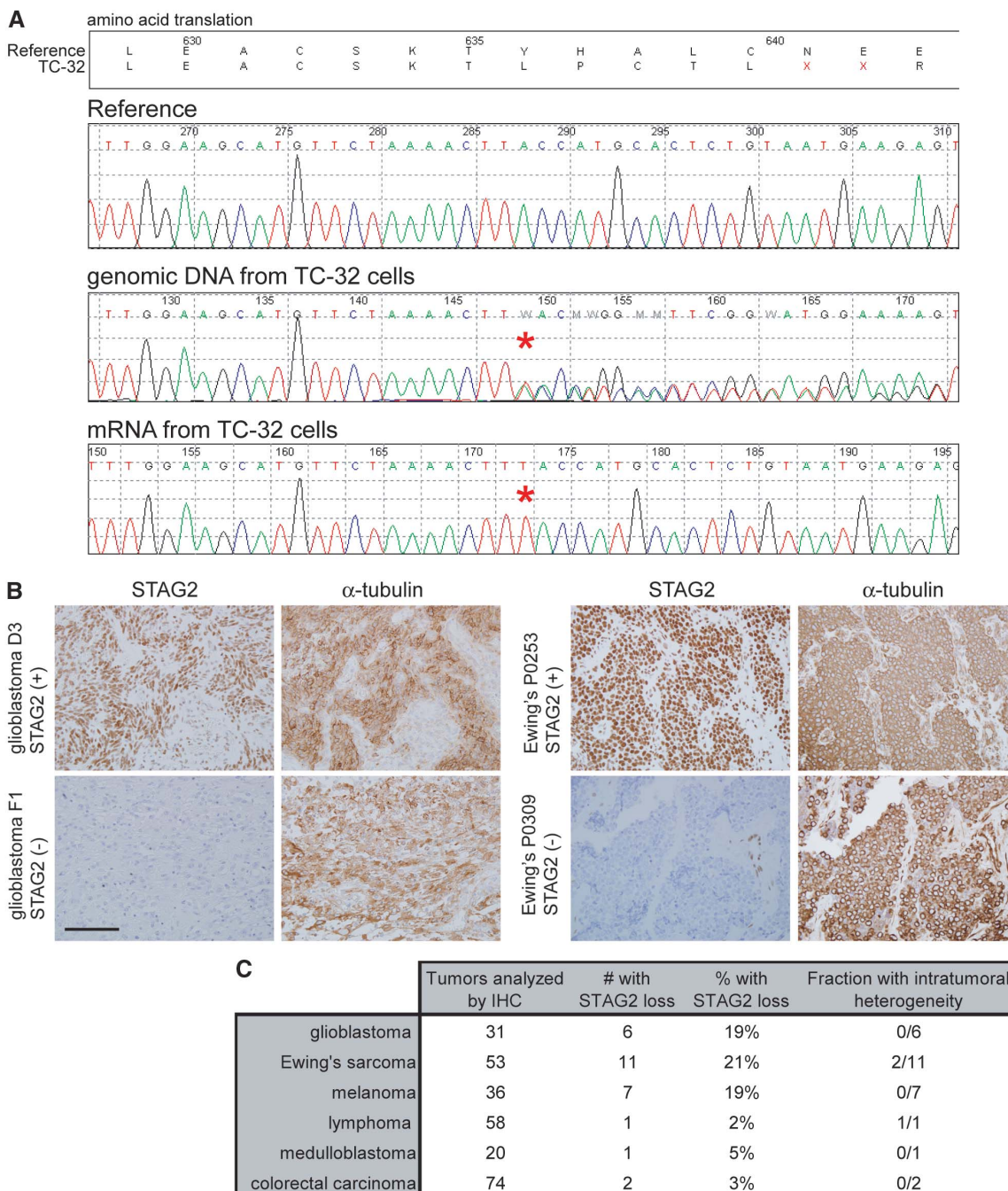
To determine whether endogenous mutations in *STAG2* cause chromosomal instability and aneuploidy, we used human somatic cell gene targeting to correct the endogenous mutant allele of *STAG2* in two aneuploid glioblastoma cell lines. H4 cells are reported to be hypertriploid with modal chromosome number 73 (range 63 to 78), and 42MGBA cells are hypertetraploid with modal chromosome number 89 (range 88 to 95). Adeno-associated virus (AAV) targeting vectors (14) were constructed and used to correct the

25-bp insertion mutation in exon 12 of H4 cells and the nonsense mutation in exon 20 of 42MGBA cells (Fig. 3A and figs. S24 and S25A). Western blots were then performed to document that correction of the mutations in H4 and 42MGBA cells led to reexpression of *STAG2* protein (Fig. 3B and fig. S26A). Similarly, somatic-cell gene targeting was used to introduce a nonsense mutation into the endogenous wild-type allele of *STAG2* in HCT116, a near-diploid human colorectal cancer cell line with stable karyotype (figs. S25B and S26B).

The cohesin complex plays several different roles in eukaryotic cell biology, including sister chromatid cohesion and regulation of chromatin

architecture and transcription (15–17). We initially tested whether mutational inactivation of the cohesin subunit *STAG2* contributes to improper sister chromatid cohesion using the *STAG2* knockin (KI, H4 and 42MGBA) and knockout (KO, HCT116) cells. Cells were treated with either taxol or nocodazole to induce mitotic arrest, chromatids were visualized by Giemsa staining, and the percentages of parallel or separated chromatids were scored in a blinded fashion (Fig. 3, C and D). *STAG2*-proficient HCT116 cells demonstrated virtually perfect sister chromatid cohesion that was markedly abrogated upon knockout of *STAG2*. In contrast, *STAG2*-deficient H4

Fig. 2. Single-hit genetic inactivation causes loss of *STAG2* in diverse human tumor types. **(A)** *STAG2* sequence traces from TC-32 Ewing's sarcoma cells derived from a female patient. Whereas the genomic DNA is heterozygous for a single nucleotide insertion (T), the mRNA is derived exclusively from the mutant allele on the active X chromosome. **(B)** Immunohistochemistry identifies frequent loss of *STAG2* expression in glioblastoma and Ewing's sarcoma primary tumors. Scale bar, 100 μ m. **(C)** Number of tumors successfully assessed by immunohistochemistry and the fraction demonstrating complete loss of *STAG2* expression.



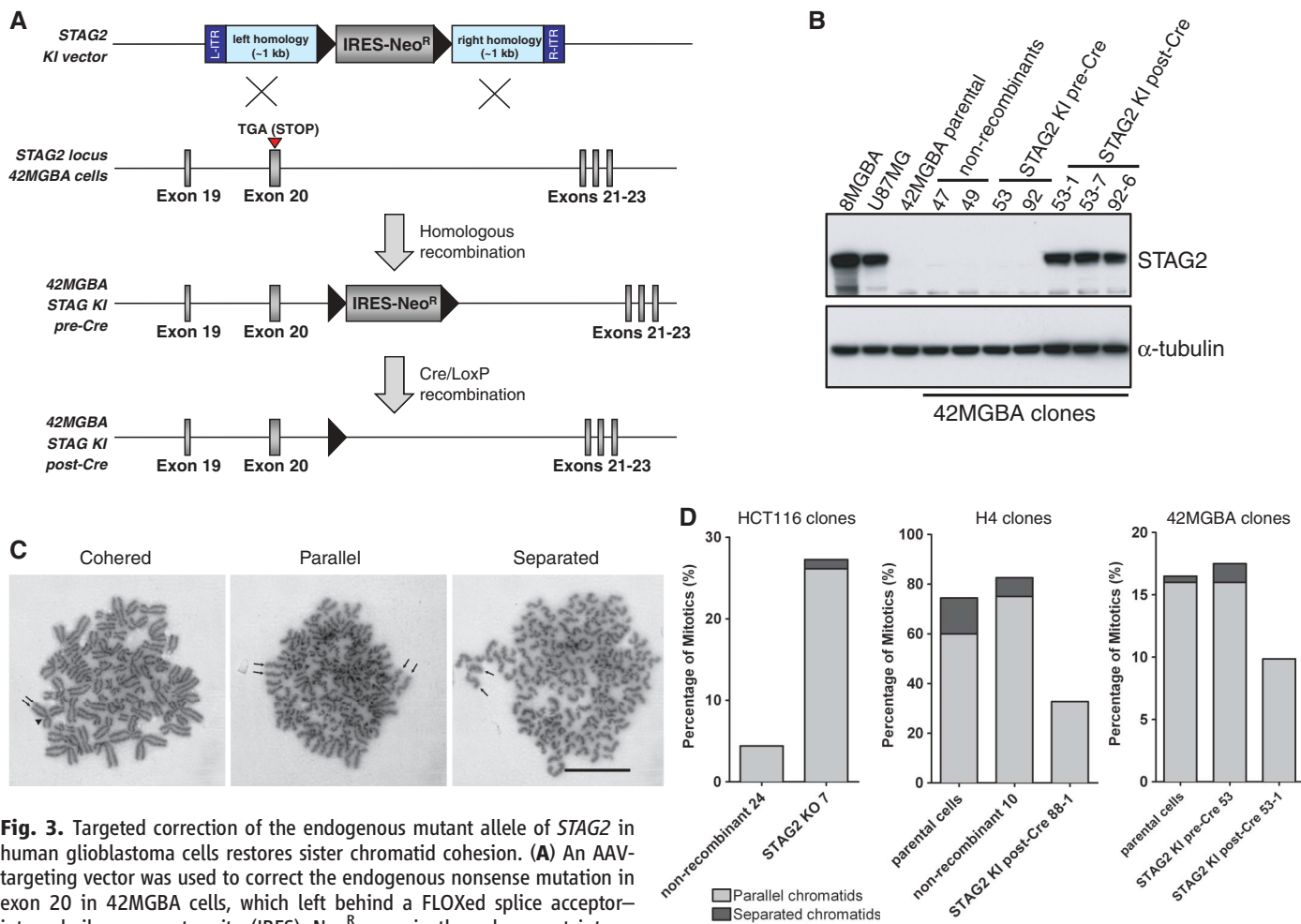


Fig. 3. Targeted correction of the endogenous mutant allele of *STAG2* in human glioblastoma cells restores sister chromatid cohesion. **(A)** An AAV-targeting vector was used to correct the endogenous nonsense mutation in exon 20 in 42MGBA cells, which left behind a FLOxed splice acceptor–internal ribosome entry site (IRES)–Neo^R gene in the subsequent intron. These “pre-Cre” clones were then infected with adenoviral Cre, which led to excision of the FLOxed splice acceptor–IRES–Neo^R gene in “post-Cre” clones. Black triangles indicate LoxP sites. **(B)** 42MGBA parental cells and two nonrecombinant clones fail to express STAG2 protein by Western blot. Two pre-Cre KI clones similarly fail to express STAG2 protein because the *STAG2* transcript gets spliced to the IRES–Neo^R gene. Three post-Cre KI clones express physiologic levels of corrected STAG2 protein, comparable to the levels in

and 42MGBA cells demonstrated substantial defects in sister chromatid cohesion that were largely reverted upon targeted correction of *STAG2*. Depletion of *STAG2* expression by lentiviral short hairpin RNA (shRNA) in HCT116 and additional near-diploid human cells with stable karyotypes led to similar defects in sister chromatid cohesion (fig. S27).

To explore whether *STAG2* regulates transcription in human cancer cells, we used expression microarrays to measure global gene expression profiles in the three different sets of isogenic *STAG2*-corrected and *STAG2* KO cells. As depicted in Fig. 4A, fig. S28, and tables S3 to S5, expression profiles of *STAG2*-proficient and deficient cells were remarkably similar [i.e., only 16 of 28,869 genes (0.06%) were modulated >1.5-fold in *STAG2*-corrected 42MGBA cells], which indicated that *STAG2* is not likely to be a major regulator of global gene expression in human cancer. Furthermore, no genes were recur-

rently up- or down-regulated by *STAG2* in more than one cell line. For example, Angiopoietin-2 expression was increased eightfold in multiple clones of *STAG2* KO HCT116 cells but was not correspondingly down-regulated in *STAG2* KI H4 or 42MGBA cells. These expression data suggest that the role of *STAG2* in cancer pathogenesis is not due to a capacity to induce global transcriptional changes or to modulate the expression of specific tumor-promoting or suppressing genes.

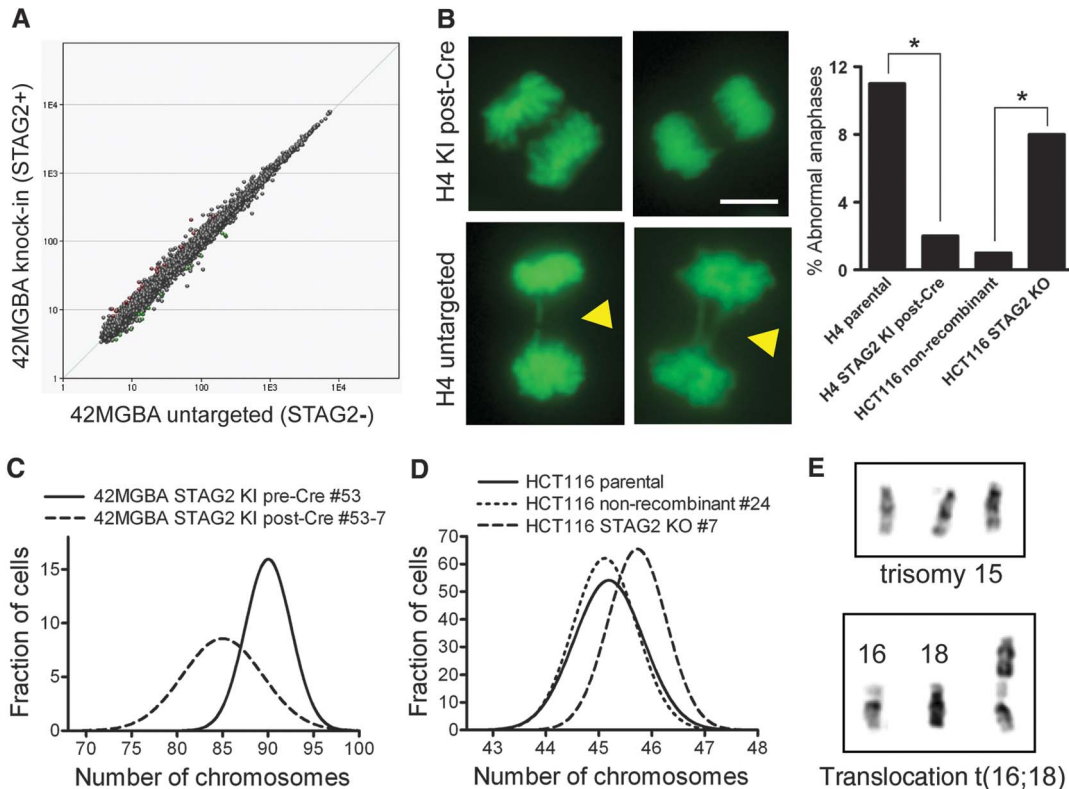
Cell cycle analysis demonstrated that *STAG2*-proficient and deficient cells had similar percentages of cells in both G₁ (2N) and G₂/M (4N) (fig. S29). However, the 2N and 4N peaks were substantially wider in each of the *STAG2*-deficient cell lines than in their isogenic *STAG2*-proficient counterparts, which suggested that *STAG2* inactivation resulted in altered chromosome counts (i.e., aneuploidy) in these cancer cells. Imaging of untreated asynchronous cells revealed the presence of abnormal mitotic figures, including lagging

8MGBA and U87MG glioblastoma cells with unmodified wild-type *STAG2* alleles. **(C)** Examples of mitotic chromosome spreads from *STAG2*-deficient H4 cells with cohered, parallel, and fully separated sister chromatids. Arrows indicate each sister chromatid in a mitotic chromosome. Arrowhead points to the centromere. Scale bar, 2 μ m. **(D)** Isogenic sets of *STAG2*-proficient and deficient cells were arrested in mitosis using taxol or nocodazole, Giemsa stained, and assayed for sister chromatid cohesion.

chromosomes and anaphase bridges in *STAG2*-deficient cells, characteristic of aneuploid divisions (Fig. 4B).

We next performed karyotypic analysis of these isogenic sets of cells. H4 cells had a wider distribution of chromosome counts than their *STAG2*-corrected derivatives (fig. S30A). Correction of mutant *STAG2* in 42MGBA cells led to a reduction in chromosome number per cell (Fig. 4C and fig. S30, B and C). Similarly, HCT116 *STAG2*-proficient cells had a modal chromosome count of 45, whereas their *STAG2*-deleted derivatives had a modal chromosome count of 46 and occasional cells with higher chromosome counts (Fig. 4D and fig. S30D). Importantly, each *STAG2*-deficient HCT116 cell with 46 chromosomes had a unique karyotype (Fig. E and fig. S31). shRNA depletion of *STAG2* in near-diploid cells with stable karyotype similarly led to altered chromosome counts (fig. S30E). Together, these results demonstrate that *STAG2* loss causes

Fig. 4. Correction of mutant *STAG2* alleles in human glioblastoma cells does not globally alter gene expression profile but reduces chromosomal instability. **(A)** Affymetrix GeneChip human gene 1.0 ST arrays were used to generate gene expression profiles in 42MGBA parental cells, two pre-Cre KI clones, and three post-Cre KI clones. The composite expression profile of the *STAG2*-mutant cells is plotted against the composite expression profile of the *STAG2*-corrected cells. **(B)** Imaging of chromosome dynamics using green fluorescent protein–histone H2B in untreated asynchronous cells (left) and quantification of abnormal mitotic figures in 100 anaphase cells (right) demonstrated lagging chromosomes and anaphase bridges (arrowheads) in *STAG2*-deficient cells. Scale bar, 5 μ m. **P* < 0.05. **(C and D)** Isogenic *STAG2*-proficient and deficient cells were arrested in prometaphase, and karyotypes were prepared using Wright’s stain. Chromosomes were counted in 100 cells for each cell line to determine the diversity of chromosome counts within the cell population. Chromosome counts are shown in fig. S30, and distribution curves from these data are shown here for *STAG2*-proficient and deficient 42MGBA cells (C) and HCT116 cells (D). **(E)** Examples of unique chromosomal aberrations present in individual HCT116 *STAG2* KO cells.



chromosomal instability and aneuploidy in human cancer cells.

It has long been thought that mutational inactivation of genes that control chromosomal segregation is responsible for aneuploidy in human cancer. Targeted overexpression or genetic inactivation of factors involved in chromatin condensation, mitotic checkpoint, and chromosome segregation has demonstrated that these genes can function to maintain chromosomal stability [examples in (18, 19, 20, 21)]. However, analysis of human cancer samples has yielded only a few examples of putative chromosome instability genes that are mutated or deleted at an appreciable frequency (22–24). We have shown here that diverse human cancers harbor mutations in the X-linked chromatid cohesion gene *STAG2* and that these mutations cause aneuploidy. We postulate that *STAG2* is likely to function as a “caretaker” tumor suppressor gene that when inactivated results in chromosomal instability, similar to other caretaker genes like *MLH1* and *MSH2* that, when inactivated, result in nucleotide instability (25).

References and Notes

1. D. Hanahan, R. A. Weinberg, *Cell* **144**, 646 (2011).
 2. C. Lengauer, K. W. Kinzler, B. Vogelstein, *Nature* **396**, 643 (1998).

3. L. A. Loeb, *Cancer Res.* **51**, 3075 (1991).
 4. D. P. Cahill *et al.*, *Nature* **392**, 300 (1998).
 5. K. Nasmyth, *Science* **297**, 559 (2002).
 6. D. A. Solomon *et al.*, *Cancer Res.* **68**, 2564 (2008).
 7. D. A. Solomon *et al.*, *Cancer Res.* **68**, 10300 (2008).
 8. Materials and methods are available as supporting material on Science Online.
 9. I. Sumara, E. Vorlaufer, C. Gieffers, B. H. Peters, J. M. Peters, *J. Cell Biol.* **151**, 749 (2000).
 10. C. H. Haering, A. M. Farcas, P. Arumugam, J. Metson, K. Nasmyth, *Nature* **454**, 297 (2008).
 11. M. J. Walter *et al.*, *Proc. Natl. Acad. Sci. U.S.A.* **106**, 12950 (2009).
 12. K. L. Gorringer *et al.*, *Genes Chromosomes Cancer* **48**, 931 (2009).
 13. J. Rocquain *et al.*, *Am. J. Hematol.* **85**, 717 (2010).
 14. J. S. Kim, C. Bonifant, F. Bunz, W. S. Lane, T. Waldman, *Nucleic Acids Res.* **36**, e127 (2008).
 15. E. Lara-Pezzi *et al.*, *J. Biol. Chem.* **279**, 6553 (2004).
 16. K. S. Wendt *et al.*, *Nature* **451**, 796 (2008).
 17. M. H. Kagey *et al.*, *Nature* **467**, 430 (2010).
 18. N. Zhang *et al.*, *Proc. Natl. Acad. Sci. U.S.A.* **105**, 13033 (2008).
 19. D. J. Baker, F. Jin, K. B. Jeganathan, J. M. van Deursen, *Cancer Cell* **16**, 475 (2009).
 20. P. V. Jallepalli *et al.*, *Cell* **105**, 445 (2001).
 21. R. Sotillo *et al.*, *Cancer Cell* **11**, 9 (2007).
 22. H. Rajagopalan *et al.*, *Nature* **428**, 77 (2004).
 23. Z. Wang *et al.*, *Cancer Res.* **64**, 2998 (2004).
 24. T. D. Barber *et al.*, *Proc. Natl. Acad. Sci. U.S.A.* **105**, 3443 (2008).

25. K. W. Kinzler, B. Vogelstein, *Nature* **386**, 761, 763 (1997).

Acknowledgments: We thank K. Creswell, S. Sen, and Applied Genetics Laboratories for technical assistance; and M. White and the Brain Tumor Tissue Bank of Canada, S. Baker, F. Bunz, J.-M. Peters, and the Children’s Oncology Group for reagents and tumor samples. This research was supported by NIH grants R01CA115699 (T.W.), R21CA143282 (T.W.), SPORE grant CA097257 (C.D.J.), and American Cancer Society grant RSG0619101 (T.W.). Georgetown University has filed a patent application relating to the application of the mutations described in this work to the diagnosis and treatment of cancer. Y.S. is supported by the Intramural Research Programs of the National Human Genome Research Institute, NIH. Primer sequences are in table S6. For copy number arrays: the scanned array images and processed data sets have been deposited in the Gene Expression Omnibus (www.ncbi.nlm.nih.gov/geo, dataset GSE13021). For expression microarrays: the scanned array images and processed data sets have been deposited in the Gene Expression Omnibus (www.ncbi.nlm.nih.gov/geo, dataset GSE28214).

Supporting Online Material

www.sciencemag.org/cgi/content/full/333/6045/1039/DC1
 Materials and Methods
 Figs. S1 to S31
 Tables S1 to S6
 References

31 January 2011; accepted 30 June 2011
 10.1126/science.1203619



Supporting Online Material for

Mutational Inactivation of *STAG2* Causes Aneuploidy in Human Cancer

David A. Solomon, Taeyeon Kim, Laura A. Diaz-Martinez, Joshlean Fair, Abdel G. Elkahloun, Brent T. Harris, Jeffrey Toretsky, Steven A. Rosenberg, Neerav Shukla, Marc Ladanyi, Yardena Samuels, C. David James, Hongtao Yu, Jung-Sik Kim, Todd Waldman*

*To whom correspondence should be addressed. E-mail: waldmant@georgetown.edu

Published 19 August 2011, *Science* **333**, 1039 (2011)
DOI: 10.1126/science.1203619

This PDF file includes

Materials and Methods
Figs. S1 to S31
Tables S1 to S6
References

Materials and Methods

Tumor tissues. A panel of 21 glioblastoma cell lines was obtained from the American Type Culture Collection (U87MG, U138MG, M059J, Hs683, H4, A172, LN18, LN229, CCF-STTG1, T98G, DBTRG-05MG), DSMZ (8MGBA, 42MGBA, DKMG, GAMG, GMS10, LN405, SNB19), and the Japan Health Sciences Foundation Health Science Research Resources Bank (AM38, NMC-G1, KG-1-C). Normal human astrocytes (NHAs) were obtained from Clonetics and AllCells. A panel of 20 subcutaneous xenografts in immunodeficient mice was generated directly from primary glioblastoma surgical specimens at the Mayo Clinic and the University of California San Francisco Brain Tumor Research Center. Generation and characterization of these primary xenografts has been previously described (1,2,3). A panel of 48 snap-frozen primary glioblastoma tumors and paired blood samples was obtained from the Brain Tumour Tissue Bank (London Health Sciences Centre, Ontario, Canada) funded by the Brain Tumour Foundation of Canada. A panel of 48 malignant melanomas and paired blood samples was obtained from patients undergoing resection at the National Cancer Institute. Melanoma primary cultures were generated from these surgical specimens by mechanical or enzymatic dispersion of tumor cells followed by expansion for 5-15 passages, and have been previously described (4). A panel of 24 Ewing's sarcoma tumors and paired normal tissue was obtained from patients undergoing resection at the Memorial Sloan-Kettering Cancer Center. In each case, tumor pathology has been confirmed by PCR-based identification of either EWS-FLI1 or EWS-ERG fusion transcripts (5). Genomic DNA was isolated from tumor cells/tissues and peripheral blood mononuclear cells using standard proteinase K digestion, phenol-chloroform

extraction, and ethanol precipitation or using the DNeasy Blood & Tissue kit (Qiagen). Matching between blood and tumor DNA was verified by direct sequencing of 26 single nucleotide polymorphisms at 24 loci.

Copy number arrays. Genomic DNA derived from 21 glioblastoma cell lines was interrogated with Affymetrix 250K Nsp I Human GeneChip Arrays. The scanned array images and processed data sets have been deposited in the Gene Expression Omnibus (<http://www.ncbi.nlm.nih.gov/geo>, dataset GSE13021), and the analysis of this data has been previously described (6,7,8).

Western blot. Primary antibodies used were STAG2 clone J-12 (Santa Cruz Biotechnology, sc-81852), α -tubulin Ab-2 clone DM1A (Neomarkers), STAG1 clone LL-16 (Santa Cruz Biotechnology, sc-81851), SGOL1 clone 3C11 (Novus Biologicals, H00151648), RASSF1A clone 3F3 (Santa Cruz Biotechnology, sc-58470), and GFP clone B-2 (Santa Cruz Biotechnology, sc-9996). Protein was isolated from 156 human cancer cell lines in RIPA buffer, resolved by SDS-PAGE, and immunoblotted following standard biochemical techniques. Cells were cultured in 10 μ M 5-aza-2-deoxycytidine (Sigma) for 96 hours and harvested in RIPA buffer.

DNA and mRNA sequencing. Individual exons of STAG2 were PCR amplified from genomic DNA using conditions and primer pairs described by Sjoblom *et al.* (9). Total RNA was purified from cultured cells using TRIZOL (Invitrogen). RT-PCR was performed using the Superscript III Platinum One-Step RT-PCR System (Invitrogen). PCR products were purified using the Exo/SAP method followed by a Sephadex spin column. Sequencing reactions were performed using Big Dye v3.1 (Applied Biosystems)

using an M13F primer, and analyzed on an Applied Biosystems 3730XL capillary sequencer. Sequences were analyzed using Mutation Surveyor (Softgenetics). Traces with putative mutations were re-amplified and sequenced from both tumor and matched normal DNA from blood when available. All primer sequences are available upon request.

Generation of GFP-STAG2. A full-length wild-type human STAG2 cDNA (provided by Jan-Michael Peters) was excised from pFastBac1 with Sall + XhoI and cloned in-frame into the XhoI site of the pEGFP-C3 vector (Clontech), thereby resulting in fusion of GFP to the N-terminus of STAG2. Tumor-derived mutations were introduced into the pEGFP-STAG2 expression vector by site-directed mutagenesis (Stratagene) and confirmed by DNA sequencing.

Immunohistochemistry. To verify the specificity of a STAG2 antibody for immunohistochemistry (IHC), STAG2-deficient H4 cells and a STAG2-corrected H4 clone were immersed in Histogel, embedded in paraffin, and then sectioned. IHC was performed on these sections following a standard protocol using STAG2 clone J-12 mouse monoclonal antibody (Santa Cruz Biotechnology). Two consecutive sections from glioblastoma (GL806), lymphoma (LY1501), melanoma (ME1002), medulloblastoma (BC17012), and colorectal adenocarcinoma (CO1922) tissue microarrays were obtained from U.S. Biomax. The glioblastoma arrays contained 35 cases spotted in duplicate. The lymphoma array contained 43 cases of B-cell lymphoma, 17 T-cell lymphoma, 1 Lennert lymphoma, 4 non-Hodgkin's lymphoma, and 5 Hodgkin's lymphoma, and 5 normal lymph node tissue cores all spotted in duplicate. The melanoma array contained 45 cases of malignant melanoma and 5 normal dermis

tissue cores all spotted in duplicate. The medulloblastoma array contained 20 cases spotted in triplicate. The colorectal adenocarcinoma array contained 96 cases spotted in duplicate. One Ewing's sarcoma tissue microarray was provided by the Children's Oncology Group and the Cooperative Human Tissue Network of the National Cancer Institute. This array contained 30 cases of Ewing's sarcoma spotted in duplicate and has been previously described (10). A second Ewing's sarcoma tissue microarray generated at Memorial Sloan-Kettering Cancer Center containing 25 cases of primary tumor tissue spotted in multiple replicates that has been previously described was also used (5). IHC was performed with the STAG2 antibody at a 1:50 dilution to determine the fraction of tumors that had lost expression of STAG2. IHC was simultaneously performed on a consecutive slide from each tissue microarray using α -tubulin Ab-2 clone DM1A mouse monoclonal antibody (Neomarkers) at a 1:500 dilution using an identical procedure and reagents to serve as a positive control, thereby demonstrating that any STAG2-negative cores were accessible to antibody for staining. Cores with poor tissue quality, failure to stain with α -tubulin antibody, or significant melanin pigment that interfered with interpretation of staining were excluded from the analysis.

Human somatic cell gene targeting. Homology arms for creation of STAG2 KI and KO vectors were created by high fidelity PCR from a human BAC template using Phusion DNA Polymerase (New England Biolabs) as described by the manufacturer. All homology arms were ~1 kb in size. For the H4 STAG2 KI vector, the left arm was composed of intron 11/exon 12/intron 12/exon 13/intron 13, and the right arm was composed of intron 13, as defined by ENSEMBL transcript ENST00000218089. For the 42MGBA STAG2 KI vector, the left arm was composed of intron 19/exon 20/intron 21,

and the right arm was composed of intron 21. For the HCT116 STAG2 KO vector, the left arm was composed of intron 2/exon 3/intron 3, and the right arm was composed of intron 3. The PCR products were cloned into pCR-Blunt II-TOPO (Invitrogen) and sequenced. For the HCT116 KO vector, the cloned left homology arm was then mutagenized (Quikchange, Stratagene) to introduce a stop mutation into codon 6. The sequence of all PCR and mutagenesis primers is available upon request. For all three vectors, the PCR product composing the left homology arm was then digested with Age I and Sac I, and the PCR product composing the right homology arm was digested with Eco RI and Sal I. These left and right arms were then gel purified and simultaneously cloned via four-way ligation into the pAAV-SEPT-Acceptor vector (11) that had been digested with Age I, Sac I, Eco RI and Sal I, and then gel purified. Ligation products were then transformed into chemically-competent TOP10 cells (Invitrogen), plasmid DNA was isolated, and correct clones identified by restriction analysis followed by DNA sequencing of all junctions. Next, transient stocks of AAV-2 virions were created by cotransfection of 293T cells with STAG2 KI and KO vectors together with pAAV-RC (Stratagene) and pHELPER (Stratagene) using FUGENE 6 (Roche). Two days after transfection, media was aspirated and cell monolayers were scraped into 1 mL PBS and subjected to four cycles of freeze/thaw (consisting of 10 min freeze in a dry-ice ethanol bath and 10 min thaw in a 37°C water bath, vortexing after each thaw). The lysate was then clarified by centrifugation at 12,000 rpm for 10 min in a benchtop microfuge to remove cell debris, and the virus-containing supernatant was aliquoted and stored at -80°C. 100 µL of virus was then used to infect cells in T25 tissue culture flask, and cells were passaged at limiting dilution into 96-well plates in the presence of G418 one

day after infection. The concentrations of G418 used were as follows: 1.0 mg/mL for H4 and 42MGBA cells and 0.6 mg/mL for HCT116 cells. Individual G418-resistant clones were expanded and used for the preparation of genomic DNA. Clones were tested for homologous integration of the targeting vector using a primer pair specific for the targeted allele. Once homologous recombinant clones were identified in this way, they were infected with a Cre-expressing adenovirus. Individual clones were expanded by limiting dilution and tested for the restoration of G418-sensitivity. STAG2 Western blots were then performed to confirm the restoration of STAG2 expression in H4 and 42MGBA STAG2 KI cells and the loss of STAG2 expression in HCT116 STAG2 KO cells.

Lentiviral shRNA knockdown. Five unique short hairpin RNAs (shRNA) to the STAG2 mRNA in the pLKO.1-Puro lentiviral expression vector were obtained from Open Biosystems. To make the virus, empty pLKO.1-Puro or each of these five shRNA clones were cotransfected into 293T cells with pVSV-G (Addgene) and pHR'-CMV Δ 8.2 (Addgene) helper plasmids using Fugene 6 (Roche). Virus-containing conditioned medium was harvested 48 h after transfection, filtered, and used to infect recipient cells in the presence of 8 μ g/mL of polybrene. Infected cells were selected with 2 or 10 μ g/mL of puromycin until all mock-infected cells were dead and then maintained in puromycin.

Sister chromatid cohesion assay. Cells were arrested in mitosis by culturing in the presence of 220 nM taxol or 500 nM nocodazole. Chromosome spreads were then performed by subjecting the cells to hypotonic treatment, followed by fixation with Carnoy's fixative, spreading on glass slides, and Giemsa staining as previously

described (12). Micrographs were obtained using a DeltaVision microscope (Applied Precision) fitted with a U-PlanApo 100X Oil Objective, 1.40 NA, 0.12 mm WD (Olympus) and a CoolSnap HQ2 camera (Photometrics). The incubation periods and number of cells counted per experiment are as follows: HCT116 cells and KO derivatives - 6 hours, at least 70 mitotic cells were counted per treated cell line/cell clone; H4 cells and KI derivatives - 10 hours, at least 90 mitotic cells were counted per treated cell line/cell clone; 42MGBA cells and KI derivatives - 18 hours, at least 200 mitotic cells were counted per treated cell line/cell clone; HCT116, CAL-51 and DLD-1 cells and lenti-shRNA derivatives - 6 hours, at least 200 mitotic cells were counted per cell line.

Expression microarrays. Total RNA was purified from asynchronously proliferating STAG2-proficient and deficient cells using TRIZOL (Invitrogen) according to the manufacturer's instructions. RNA was further purified using the RNeasy MinElute Cleanup kit (Qiagen). RNA quality was verified using a Bioanalyzer (Agilent) and concentration was measured using a NanoDrop (Thermo Scientific). 300 ng of total RNA was used for labeling. The hybridization cocktail containing the fragmented and labeled cDNAs were hybridized to Affymetrix Human GeneChip 1.0 ST microarrays. The microarrays were washed and stained in an Affymetrix Fluidics Station using standard Affymetrix protocols. The probe arrays were stained with streptavidin-phycoerythrin solution (Molecular Probes) and enhanced using an antibody solution containing 0.5 mg/mL of biotinylated anti-streptavidin (Vector Laboratories). An Affymetrix Gene Chip Scanner 3000 was used to scan the probe arrays. Gene expression intensities were calculated using GeneChip Command Console Software (AGCC). .cel files generated by the Affymetrix AGCC program were imported in the

Affymetrix Expression Console software and RMA (Robust Multichip Analysis) normalization was performed to generate the .chp files. The .chp files were normalized, log₂ transformed, and summarized. Pairwise comparisons within GeneSifter software (VizX Labs) were performed on the .chp files, and t-test comparison and Benjamin and Hochberg correction were applied. The scanned array images and processed data sets have been deposited in the Gene Expression Omnibus (<http://www.ncbi.nlm.nih.gov/geo>, dataset GSE28214)

Flow cytometry. Asynchronously proliferating cells were trypsinized and collected by centrifugation. Cells were resuspended in PBS and fixed in cold ethanol to a final concentration of 75% ethanol. Cells were then stained with 3 μ M propidium iodide for 2 hours and analyzed by flow cytometry in a BD FACSort instrument using FCS Express v.3 software (DeNovo Software).

Fluorescent microscopy. Cells were grown on glass coverslips coated with poly-L-lysine (Sigma). The pEGFP-Histone H2B expression vector has been previously described (13). pEGFP-STAG2 and pEGFP-Histone H2B were transfected into cells using Fugene 6 (Roche). Cells were fixed in 4% formaldehyde and stained with Hoechst 33342 (Molecular Probes) before mounting on slides. As indicated, extraction of soluble proteins was performed using 0.1% Triton X-100 in PBS for 5 min on ice prior to formaldehyde fixation. Imaging was performed on an Olympus IX71 epifluorescent microscope with Olympus PlanApo objectives and Olympus DP70 CCD camera.

Karyotyping. Cultured cells were treated with 0.02 μ g/ml colcemid for 55 minutes at 37°C. The cells were then trypsinized, centrifuged for 7 minutes at 200 x g, and the cell

pellet resuspended in warmed hypotonic solution and incubated at 37°C for 11 minutes. The swollen cells were then centrifuged and the pellet resuspended in 8 mL of Carnoy's fixative (3:1 methanol:glacial acetic acid). After incubation in fixative at room temperature for 96 minutes, the cell suspension was centrifuged and washed twice in Carnoy's fixative. After the last centrifugation, the cells were resuspended in 1 to 3 mL of freshly prepared fixative to produce an opalescent cell suspension. Drops of the final cell suspension were placed on clean slides and air-dried. Slides were stained with a 1:3 mixture of Wright's stain and 0.06 M phosphate buffer for 4-10 minutes, washed with tap water for 5 seconds, and then air-dried. One hundred cells in metaphase were examined for chromosome count.

Statistical analysis. Statistical analysis was performed using GraphPad Prism software. Two-tailed unpaired t-tests were performed for comparison of means analysis.

Supplementary Figure and Table Legends

Supplementary Figure 1. PCR confirmation of STAG2 genomic deletion in U138MG glioblastoma cells. PCR for multiple STAG2 exons using genomic DNA from U138MG cells as template resulted in no amplification products, whereas PCR using genomic DNA from A172 and U87MG glioblastoma cells with intact STAG2 loci yielded amplification products at the expected molecular weight. PCR for the WTX gene that resides 60 Mb centromeric to the STAG2 gene on the X chromosome yielded amplification products at the predicted molecular weight in all three glioblastoma cell lines.

Supplementary Table 1. Genetic lesions of STAG2 identified in diverse human tumor types including zygosity of genetic lesions, mechanism of biallelic inactivation, and known karyotypic aberrations in these tumor samples.

Supplementary Figure 2. STAG2 mutations identified in glioblastoma cells. **(A)** H4 cells have a 25 bp insertion/duplication in exon 12 resulting in a frameshift and early truncation of the encoded STAG2 protein. **(B)** 42MGBA cells have a nonsense mutation in codon 653 in exon 20 resulting in early truncation of the encoded STAG2 protein.

Supplementary Figure 3. STAG2 mutations identified in glioblastoma tumor samples. **(A)** GBM p785 has a somatic missense mutation at codon 299 in exon 11, resulting in an aspartic acid to alanine change in the stromalin conservative domain (SCD) of STAG2. **(B)** GBM 14 has a G>C mutation in the canonical splice acceptor of exon 9. **(C)** GBM 44 has a two bp deletion (AA) in exon 9 causing a frameshift and early

truncation of the encoded STAG2 protein. **(D)** SF7300 has a C>T mutation in the splice acceptor of exon 11.

Supplementary Figure 4. (A-C) Western blots demonstrate complete loss of STAG2 expression in 2/20 hematologic, 1/6 cervical, and 1/4 kidney cancer cell lines.

Supplementary Figure 5. Human cancer cell lines in which no loss of STAG2 expression was observed. **(A-I)** Western blots for STAG2 and α -tubulin on protein isolated from 6 neuroblastoma, 14 lung, 13 colorectal, 3 gastric, 5 pancreatic, 7 gynecologic, 6 prostate, 5 bone, and 27 breast cancer cell lines.

Supplementary Figure 6. Homozygous genomic deletion of STAG2 in ES-8 Ewing's sarcoma and LOX IMVI melanoma cells. **(A)** PCR for exon 1 in the 5' untranslated region of the STAG2 gene using ES-8 genomic DNA as template resulted in no amplification product at the correct molecular weight. PCR for all coding exons of STAG2 using genomic DNA from LOX IMVI cells as template yielded no amplification products at the correct molecular weight. PCR using genomic DNA from A172 and U87MG cells with intact STAG2 loci yielded amplification products at the expected molecular weight for each STAG2 exon. **(B)** Subsequent analysis of Affymetrix SNP 6.0 copy number array data for ES-8 and LOX IMVI cells revealed focal homozygous deletions encompassing the STAG2 locus. These copy number data were obtained from the Wellcome Trust Sanger Institute Cancer Genome Project (<http://www.sanger.ac.uk/genetics/CGP>).

Supplementary Figure 7. Intragenic deletion of STAG2 coding exons 28-30 in SR immunoblastic lymphoma cells in which no STAG2 protein was detected. **(A)** PCR for STAG2 coding exons 28-30 on genomic DNA from SR cells resulted in no amplification

products, whereas PCR on genomic DNA from A172 and U87MG cells with intact STAG2 loci yielded amplification products at the expected molecular weight. PCR for STAG2 coding exons 27 and 31 yielded amplification products at the predicted molecular weight in all three cell lines. **(B)** RT-PCR amplification of STAG2 from total RNA isolated from SR cells revealed the absence of sequence from the deleted coding exons 28-30 and the inappropriate junction of exon 27 with exon 31 in the maturely spliced STAG2 mRNA.

Supplementary Figure 8. STAG2 mutations identified in Ewing's sarcoma and cervical carcinoma cells. **(A)** SK-ES-1 cells have a nonsense mutation in codon 735 in exon 23 resulting in early truncation of the encoded STAG2 protein. **(B)** TC-252 cells have a one bp insertion (T) in exon 20 causing a frameshift and early truncation of the encoded STAG2 protein. **(C)** A4573 cells have a heterozygous one bp deletion (A) in exon 25 causing a frameshift and early truncation of the encoded STAG2 protein. Sequencing of the STAG2 mRNA from A4573 cells demonstrated that only the mutant allele is expressed. **(D)** CaSki cells have a 20 bp deletion that includes the intron, splice acceptor, and coding sequence of exon 9 causing early truncation of the encoded STAG2 protein.

Supplementary Figure 9. STAG2 mutations identified in malignant melanoma and Ewing's sarcoma tumor samples. **(A)** MM 29T has a somatic 6 bp duplication, causing an insertion of Asp-Met at codon 225 in the stromal antigen (STAG) domain of the encoded STAG2 protein. **(B)** ES 37 has a somatic A>G mutation 8 bp upstream of the initiating methionine in the putative Kozak consensus sequence of STAG2.

Supplementary Figure 10. Generation and characterization of a green fluorescent protein (GFP)-STAG2 fusion protein. A full-length wild-type human STAG2 cDNA (provided by Jan-Michael Peters) was excised from pFastBac1 with Sall + XhoI and cloned in-frame into the XhoI site of the pEGFP-C3 vector (Clontech), thereby resulting in fusion of GFP to the N-terminus of STAG2. **(A)** Transfection of 293T cells with pEGFP-STAG2 resulted in expression of the GFP-STAG2 fusion protein at the expected molecular weight of 168 kDa detectable by both GFP and STAG2 antibodies, whereas transfection with empty pEGFP-C3 resulted in expression of free GFP at 27 kDa detectable only by GFP antibody. **(B)** Visualization of GFP-STAG2 in cells counterstained with Hoechst 33342 revealed localization in interphase cells exclusively in the nucleus (top panels). Consistent with previous reports of STAG2 dynamics, GFP-STAG2 was largely dissociated from condensed chromosomes in mitotic cells during late prophase (middle panels) and metaphase (bottom panels). **(C)** Extraction of soluble proteins with low concentration detergent (0.1% Triton X-100) for 5 min prior to formaldehyde fixation revealed that GFP-STAG2 resides largely as an insoluble nuclear protein in interphase cells, consistent with its function as a chromatin-bound cohesin subunit.

Supplementary Figure 11. Tumor-derived mutations disrupt STAG2 localization and nuclear dynamics. Mutations identified in human tumor samples were engineered into the coding sequence of the STAG2 cDNA in the pEGFP-STAG2 expression vector and confirmed by DNA sequencing. **(A)** Empty pEGFP-C3, GFP-STAG2 wild-type, and five tumor-derived mutants were transfected into 293T cells, and Western blot was performed with antibodies to GFP and STAG2 (which is recognized at an epitope in the

C-terminus between amino acids 1130-1231). The three truncating mutations (A223X, S653X, and Q735X) produced truncated STAG2 proteins detected only with the GFP antibody, whereas the two missense mutations (K225insNM and D299A) produced full-length STAG2 proteins detected by both GFP and STAG2 antibodies. **(B)** Visualization of GFP-STAG2 wild-type expression in cells counterstained with Hoechst 33342 revealed localization exclusively in the nucleus, whereas the three truncating mutations resulted in localization of GFP-STAG2 to the cytoplasm and exclusion from the nucleus. The two missense mutations resulted in GFP-STAG2 localization to the cell nucleus similar to wild-type protein (data not shown). **(C)** Extraction with 0.1% Triton X-100 for 5 min prior to formaldehyde fixation revealed that GFP-STAG2 wild-type resides largely as an insoluble nuclear protein, whereas the two missense mutations disrupt the nuclear interactions of GFP-STAG2 resulting in soluble detergent-extractable proteins.

Supplementary Figure 12. Expression of STAG1 and other genes involved in sister chromatid cohesion are not upregulated in response to STAG2 inactivation. **(A)** Western blot analysis of STAG1 levels in 21 glioblastoma cell lines, including three with mutational inactivation of STAG2. **(B)** Western blot analysis of STAG1 and SGOL1 levels in isogenic sets of STAG2 KO (HCT116) and KI (H4) human cancer cells. **(C)** Analysis of expression microarray data for genes known to regulate sister chromatid cohesion in isogenic sets of STAG2 KI (H4, 42MGBA) and KO (HCT116) human cancer cells.

Supplementary Figure 13. Loss of STAG2 expression in cancer cells with heterozygous mutations of STAG2 is not reversible by inhibition of DNA methylation. **(A)** TC-71 cells (derived from a male patient, harboring wild-type STAG2), TC-32 cells

(female patient, heterozygous frameshift mutation of STAG2), A4573 cells (female patient, heterozygous frameshift mutation of STAG2), and SK-ES-1 cells (male patient, homozygous nonsense mutation of STAG2) were cultured in the presence or absence of 10 μ M 5-aza-2-deoxycytidine for 96 hours. Total protein was harvested in RIPA buffer and assayed for STAG2 expression by Western blot. **(B)** Western blot for RASSF1A, known to be silenced by DNA methylation and induced by 5-aza-2-deoxycytidine in SK-ES-1 cells, is shown as a control.

Supplementary Figure 14. Validation of a STAG2 antibody for immunohistochemistry in formalin-fixed, paraffin-embedded tissue. **(A)** STAG2-deficient (H4 non-recombinant clone 10) and STAG2-proficient (H4 STAG2 KI post-Cre clone 8-1) cells were fixed in 4% formalin, immersed in Histogel, embedded in paraffin, and then sectioned onto the same slide for simultaneous staining. Immunohistochemistry was performed using the STAG2 clone J-12 mouse monoclonal antibody (Santa Cruz Biotechnology, sc-81852), which binds to an epitope near the C-terminus of the protein that is absent in cells with truncating mutations of the STAG2 gene (*e.g.* H4 cells). Antibody complexes were visualized by 3,3'-diaminobenzidine enzymatic reaction, and counterstaining with hematoxylin was performed. STAG2 staining was completely absent in non-recombinant H4 cells but was intensely present in the STAG2-corrected H4 clone. This staining was observed exclusively in the nucleus of each cell without significant cell-to-cell variation in expression level, consistent with previous reports on the localization and expression of STAG2. **(B)** Similar absence of STAG2 staining by immunohistochemistry was observed in additional cell lines harboring truncating mutations of STAG2, including 42MGBA cells shown here.

Supplementary Figure 15. Levels of STAG2 expression are not dependent on cell cycle stage. **(A)** Asynchronously proliferating HCT116 and 293T cells (both with unmodified wild-type STAG2 alleles) were cultured in the presence or absence of 200 ng/mL nocodazole for 12 hrs, stained with propidium iodide (PI), and assayed by flow cytometry. **(B)** Total cell lysate was collected from cells treated as in (A), and levels of STAG2 expression were measured by Western blot. These data indicate that cell-to-cell variation observed in immunohistochemistry of primary tumors is due to intratumoral genetic heterogeneity and not due to differences in cell cycle stage.

Supplementary Figure 16. Immunohistochemistry with STAG2 and α -tubulin antibodies to normal non-neoplastic tissue is shown from appendix, lymph node, skeletal muscle, thymus gland, and skin. Robust expression of STAG2 was ubiquitously observed in all non-neoplastic tissues studied.

Supplementary Table 2. Clinical and pathological characteristics of human primary tumors demonstrating STAG2 loss by immunohistochemistry.

Supplementary Figure 17. STAG2 immunohistochemistry of additional glioblastoma tumors. STAG2-expressing lymphocytes surround an island of STAG2-deficient tumor cells in glioblastoma C10, demonstrating the somatic nature of STAG2 loss in this patient's tumor.

Supplementary Figure 18. STAG2 immunohistochemistry of melanoma tumors.

Supplementary Figure 19. STAG2 immunohistochemistry of additional Ewing's sarcoma tumors. STAG2-expressing perivascular endothelial cells are present in both

STAG2-deficient Ewing's sarcoma tumors, demonstrating the somatic nature of STAG2 loss in these tumors.

Supplementary Figure 20. Intratumoral heterogeneity of STAG2 expression in two replicate cores of a Ewing's sarcoma.

Supplementary Figure 21. STAG2 immunohistochemistry of two STAG2-proficient lymphomas and two replicate cores of lymphoma A11/B11 with intratumoral heterogeneity for STAG2 loss.

Supplementary Figure 22. STAG2 immunohistochemistry of medulloblastoma tumors.

Supplementary Figure 23. STAG2 immunohistochemistry of colorectal (CRC) adenocarcinoma tumors. STAG2-expressing stromal fibroblasts and perivascular endothelial cells are present in both STAG2-deficient tumors, demonstrating the somatic nature of STAG2 loss in these tumors.

Supplementary Figure 24. PCR screen and DNA sequence confirmation of 42MGBA STAG2 knockin clones. **(A)** 42MGBA cells were infected with an AAV-STAG2 KI vector as depicted in Fig. 3A. Individual G418-resistant clones were established by limiting dilution in 96-well plates, genomic DNA prepared, and tested by PCR for homologous integration of the targeting vector. Clones with random integration of the targeting vector generate a single 1.3 kb band, whereas clones with targeted integration (53 and 92) generate a 1.0 kb band as well. **(B)** PCR products derived from the targeted allele were sequenced to demonstrate that the endogenous mutant STAG2 gene had been corrected via homologous recombination.

Supplementary Figure 25. Targeting strategy for correction of STAG2 mutation in H4 cells and introduction of a nonsense mutation in HCT116 cells. **(A)** Diagram depicting the targeted homologous recombination event for correcting the endogenous STAG2 25 bp insertion causing a frameshift at codon 357 in H4 cells. In the initial step, an AAV-based targeting vector was created for the purpose of correcting the exon 12 mutation, leaving behind a FLOXed splice acceptor-IRES-Neo^R gene in intron 13. Clones with targeted integration and mutation correction were identified by PCR and DNA sequencing. These cells (pre-Cre clones) were then transiently infected with a Cre-expressing adenovirus, and completed STAG2 knock-in (KI) clones in which the splice acceptor-IRES-Neo^R gene had been deleted by Cre/LoxP recombination were identified by screening for G418-sensitivity (post-Cre clones). **(B)** Diagram depicting the targeted homologous recombination event for introducing a nonsense mutation into codon 6 of the STAG2 gene in HCT116 cells. In the initial step, an AAV-based targeting vector was created for the purpose of introducing the mutation into exon 3, leaving behind a FLOXed splice acceptor-IRES-Neo^R gene in intron 3. Clones with targeted integration and introduction of the mutation were identified by PCR and DNA sequencing.

Supplementary Figure 26. Western blot confirmation of H4 and HCT116 STAG2 gene targeted cells. **(A)** H4 parental cells and two pre-Cre clones in which the STAG2 KI vector had integrated by homologous recombination but in which the splice acceptor-IRES-Neo^R had not yet been removed fail to express STAG2 protein. The pre-Cre clones fail to express STAG2 protein due to aberrant splicing between STAG2 exon 12 and the splice acceptor-IRES-Neo^R. Six STAG2 KI post-Cre clones in which the splice acceptor-IRES-Neo^R was successfully removed via Cre/LoxP recombination express

physiologic levels of corrected STAG2 protein, comparable to the levels in C33A and HeLa cells with unmodified wild-type STAG2 alleles. **(B)** Parental HCT116 cells and three clones in which the STAG2 KO vector integrated randomly (non-recombinants) express physiologic levels of STAG2 protein, comparable to DLD-1 cells. In contrast, four clones in which the STAG2 KO vector integrated via homologous recombination, introducing a nonsense mutation into codon 6, demonstrate abrogation of STAG2 expression. In these clones, a small amount of STAG2 appears to be expressed, presumably via re-initiation at a downstream methionine such as amino acid 70.

Supplementary Figure 27. Depletion of STAG2 expression via lentiviral shRNA in multiple human cell lines with stable karyotype leads to sister chromatid cohesion defects. **(A)** Two near-diploid human colon cancer cell lines (HCT116 and DLD-1) and one near-diploid human breast cancer cell line (CAL-51) with stable karyotypes were infected with lentivirus expressing two unique shRNAs to STAG2 or empty pLKO vector. Stably expressing pooled clones were established by puromycin selection and assayed for STAG2 expression by Western blot. shRNA 3782 effectively reduced the level of STAG2 protein by >99.9%. **(B)** STAG2-proficient and shRNA-depleted cells were arrested in mitosis using taxol for 6 hrs, Giemsa stained, and assayed for sister chromatid cohesion. The fraction of cells with cohered and parallel sister chromatids is plotted.

Supplementary Figure 28. Global gene expression profiling of isogenic sets of STAG2 gene targeted cells. **(A)** Affymetrix GeneChip Human Gene 1.0 ST arrays were used to generate gene expression profiles in parental H4 cells, two independently derived non-recombinant clones, and three independently derived STAG2 KI post-Cre clones.

Composite expression profiles of the three STAG2-mutant cells is plotted against the composite expression profiles of the three STAG2-corrected cells. **(B)** Identical composite expression profile comparison as in (A) using two non-recombinant HCT116 clones and two HCT116 STAG2 KO clones.

Supplementary Table 3. List of genes whose expression is modulated by STAG2 in H4 glioblastoma cells. Genes differentially expressed (>3.0-fold at $p < 0.05$) in STAG2-deficient (H4 parental cells and two non-recombinant clones) and STAG2-proficient H4 cells (three STAG2 KI post-Cre clones) are listed.

Supplementary Table 4. List of genes whose expression is modulated by STAG2 in 42MGBA glioblastoma cells. Genes differentially expressed (>1.5-fold at $p < 0.05$) in STAG2-deficient (42MGBA parental cells and two pre-Cre clones) and STAG2-proficient 42MGBA cells (three STAG2 KI post-Cre clones) are listed.

Supplementary Table 5. List of genes whose expression is modulated by STAG2 in HCT116 cells. Genes differentially expressed (>2.0-fold at $p < 0.05$) in STAG2-proficient (two HCT116 non-recombinant clones) and STAG2-deficient HCT116 cells (two STAG2 KO clones) are listed.

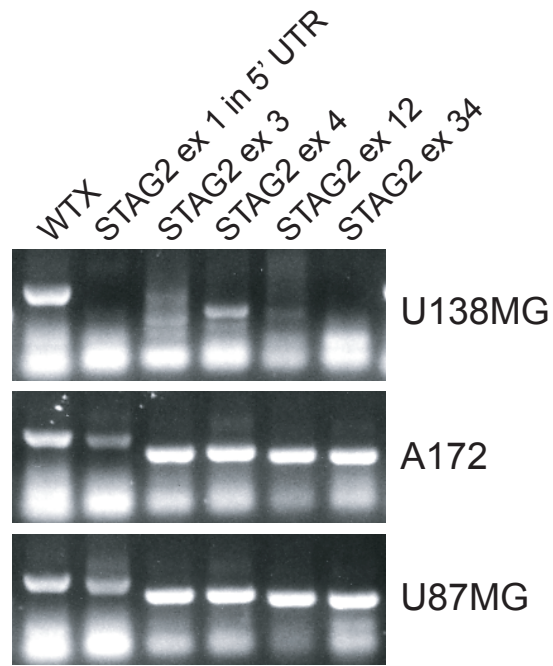
Supplementary Figure 29. (A) Asynchronously proliferating STAG2-deficient and proficient H4 cells were fixed in ethanol, stained with propidium iodide, and analyzed by flow cytometry. Representative histograms are shown with the DNA content of 17,600 cells plotted for both clones. The width of the 2N and 4N peaks is substantially greater in STAG2-deficient than in STAG2-corrected H4 cells. **(B)** Quantification of the coefficient of variance (a measure of variation in DNA content within a cell population) of

the 2N peak from asynchronously proliferating STAG2-deficient and proficient H4 and HCT116 cells is shown. *, $p < 0.05$.

Supplementary Figure 30. Karyotypic analysis of STAG2-proficient and deficient cells. Isogenic STAG2-proficient and deficient cells were arrested in mitosis and karyotypes prepared using Wright's Stain. Chromosomes were counted in 100 prometaphase cells for each cell line to determine the diversity of chromosome counts within the cell population. Chromosome counts and statistical analysis are shown for STAG2-proficient and deficient H4 **(A)**, 42MGBA **(B-C)**, HCT116 **(D)**, and DLD-1 cells **(E)**. Distribution curves derived from this data are depicted in Fig. 4C-D.

Supplementary Figure 31. (A-C) Three representative karyotypes from HCT116 STAG2 KO clone #7. Ten karyotypes were prepared by G-banding which demonstrated that each cell derived from this single cell clone contained unique chromosomal aberrations including trisomies, monosomies, translocations, and marker chromosomes (UC).

Supplementary Figure 1



Supplementary Table 1

Sample	Tumor type	Sample type	Mutation observed	Exon no. #	mRNA position #	Protein change #
KG-1	acute myelogenous leukemia	cell line	none identified	-	-	no protein
CaSki	cervical carcinoma	cell line	deletion TTTACTCTTTAAAAATAGCT	9	1072(-18)..1073	223A>truncation
A4573	Ewing's sarcoma	cell line	deletion A	25	2929	842N>frameshift
ES-8	Ewing's sarcoma	cell line	deletion of noncoding exons in 5' UTR	1,2	1..307	no protein
SK-ES-1	Ewing's sarcoma	cell line	C>T (nonsense)	23	2607	735Q>Stop
SK-NEP-1	Ewing's sarcoma	cell line	none identified	-	-	no protein
TC-252	Ewing's sarcoma	cell line	insertion T	20	2310..2311	636Y>frameshift
TC-32	Ewing's sarcoma	cell line	insertion T	20	2310..2311	636Y>frameshift
ES 37	Ewing's sarcoma	primary tumor	A>G, 8 bp upstream of initiating ATG	3	397	no protein
42MGBA	glioblastoma	cell line	C>G (nonsense)	20	2362	653S>Stop
H4	glioblastoma	cell line	insertion TACTGCTCTACAAGGGCTTTATTAT	12	1472..1473	357N>frameshift
U138MG	glioblastoma	cell line	whole gene deletion	1-35	1..6277	no protein
GBM p785	glioblastoma	primary tumor	A>C (missense)	11	1300	299D>A
GBM 14	glioblastoma	primary xenograft	G>C, splice acceptor	9	1072(-1)	223A>truncation
GBM 44	glioblastoma	primary xenograft	deletion AA	9	1110..1111	236N>frameshift
SF7300	glioblastoma	primary xenograft	C>T, splice acceptor	11	1298(-9)	undetermined
SR	immunoblastic lymphoma	cell line	intragenic deletion of exons 28-30	28-30	3180..3681	deletion 925-1092
LOX IMVI	melanoma	cell line	deletion of exons 3-35	3-35	308..6277	no protein
MM 29T	melanoma	primary culture	insertion TATGAA	9	1078..1079	225K>insertNM

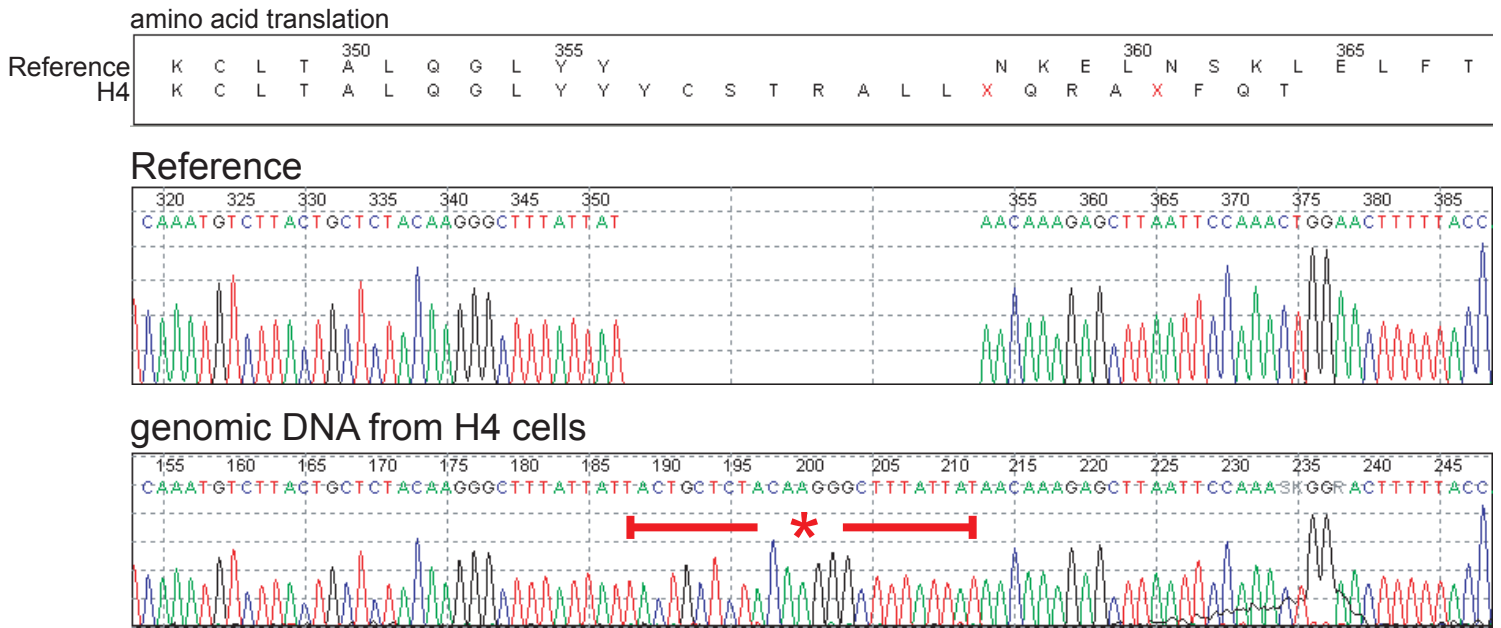
#The exon number, mRNA, and amino acid coordinates are annotated according to STAG2 transcript variant 1 mRNA GenBank Accession NM_001042749.1.

1. R.A. Pattillo *et al.*, *Science* **196**, 1456-8 (1977).
2. J. Whang-Peng *et al.*, *Cancer Genet. Cytogenet.* **21**, 185-208 (1986).
3. M.A. Smith *et al.*, *Pediatr. Blood Cancer* **50**, 703-6 (2008).
4. J.G. Hodgson *et al.*, *Neuro Oncol.* **11**, 477-87 (2009).
5. O. Fodstad *et al.*, *Int. J. Cancer* **41**, 442-9 (1988).

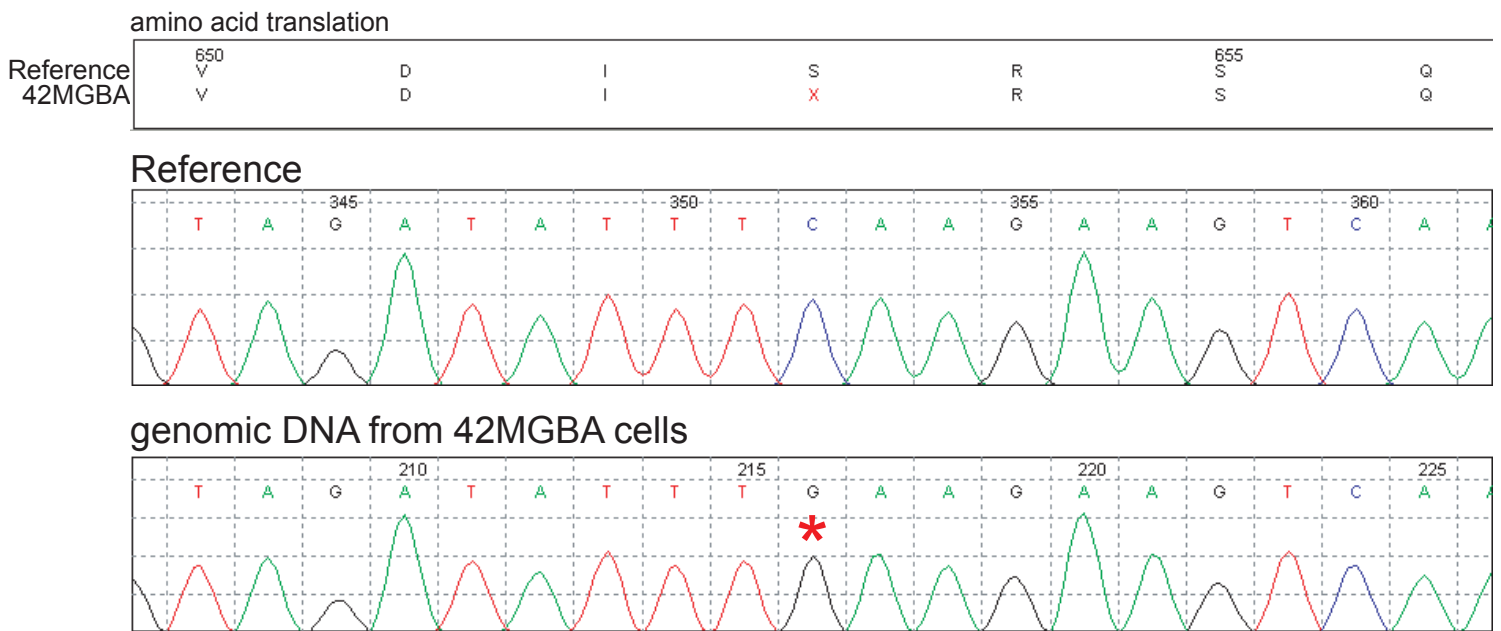
gDNA zygosity	mRNA zygosity	Somatic/germline	Patient age, sex	Tumor genotype	Mechanism of biallelic inactivation	Cytogenetic profile of tumor sample; Source of data
-	-	ND	59 M	XY	ND	modal number 47, monosomy 5,7,8,12,17; ATCC
Homozygous	-	ND	40 F	XX	loss of heterozygosity	hypotriploid, modal number 77, range 66-95; ref. 1
Heterozygous	Homozygous	ND	17 F	XX	X chromosome inactivation	hypertriploid, modal number 71, range 52-78; ref. 2
Homozygous	-	ND	10 M	XY	male patient w/ single allele	t(11;22) translocation, otherwise unknown
Homozygous	-	ND	18 M	X	male patient w/ single allele	hyperdiploid, modal number 49, range 44-51; ATCC
-	-	ND	25 F	XX	ND	hypotriploid, range 57-67; ref. 3
Heterozygous	Homozygous	ND	F	XX	X chromosome inactivation	t(11;22) translocation, otherwise unknown
Heterozygous	Homozygous	ND	17 F	XX	X chromosome inactivation	hyperdiploid, modal number 48, range 46-49; ref. 2
Homozygous	-	somatic	25 M	unknown	male patient	t(11;22) translocation, otherwise unknown
Homozygous	-	ND	63 M	XX	male patient w/ duplicated mutant allele	hypertetraploid, range 88-95; this study
Homozygous	-	ND	37 M	XXYY	male patient w/ duplicated mutant allele	hypertriploid, modal number 73, range 63-78; ATCC
Homozygous	-	ND	47 M	XY	male patient w/ single allele	hyperdiploid to pentaploid; ATCC
Homozygous	-	somatic	77 M	unknown	male patient	unknown
Homozygous	-	ND	M	XY	male patient w/ single allele	monosomy 10, LOH 9p; ref. 4
Heterozygous	Homozygous	ND	F	XX	X chromosome inactivation	trisomy 7, monosomy 10; ref. 4
Homozygous	-	ND	M	XY	male patient w/ single allele	unknown
Homozygous	-	ND	11 M	XY	male patient w/ single allele	unknown
Homozygous	-	ND	58 M	X	male patient w/ single allele	modal number 46, trisomy 7; ref. 5
Homozygous	-	somatic	51 M	unknown	male patient	unknown

Supplementary Figure 2

A

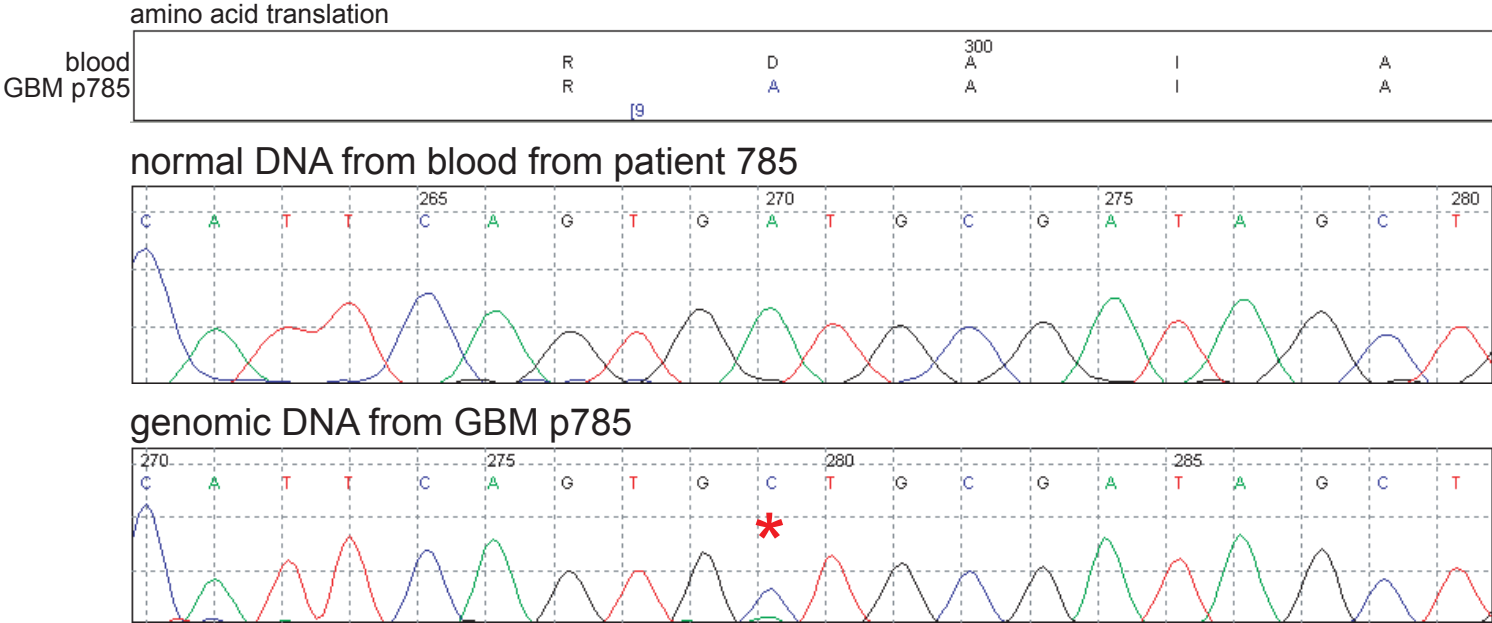


B

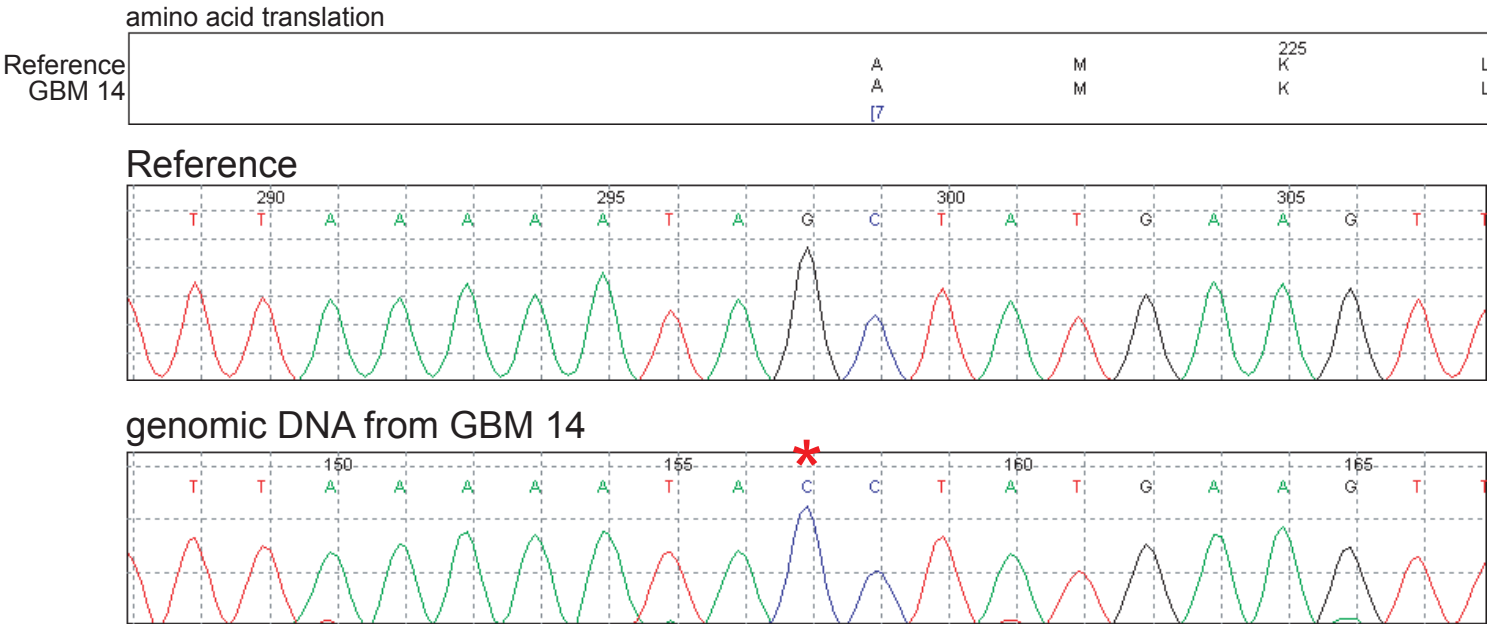


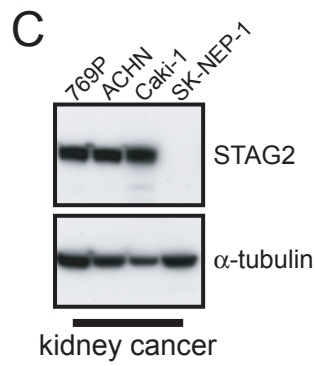
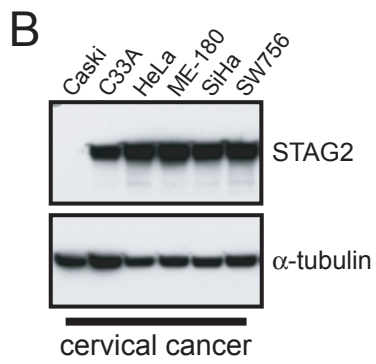
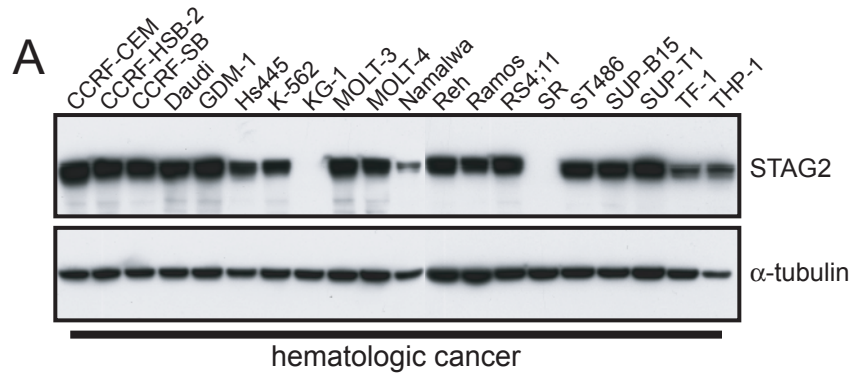
Supplementary Figure 3A-B

A

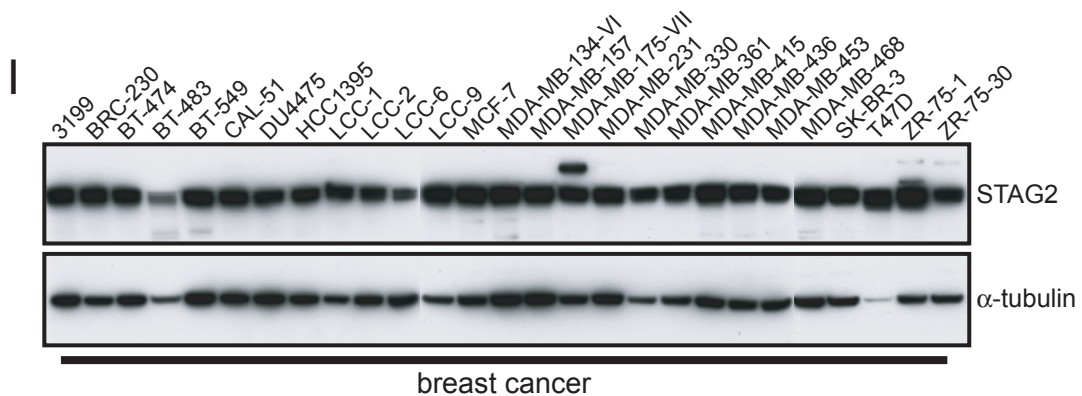
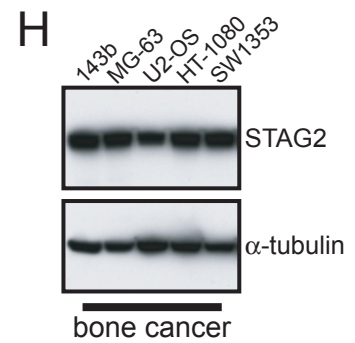
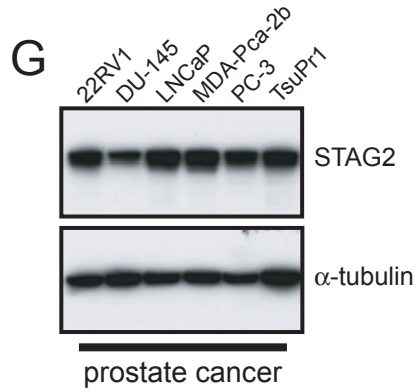
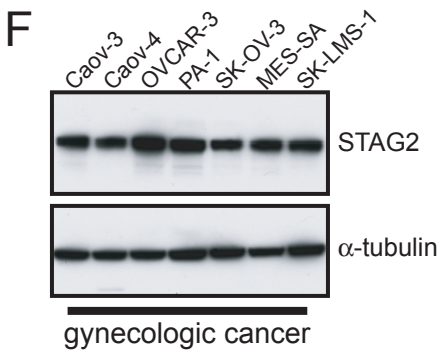
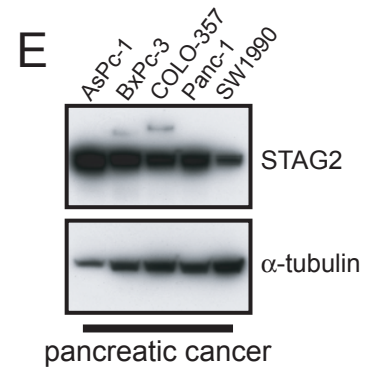
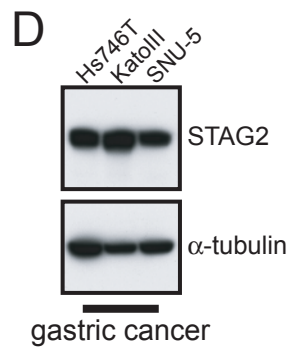
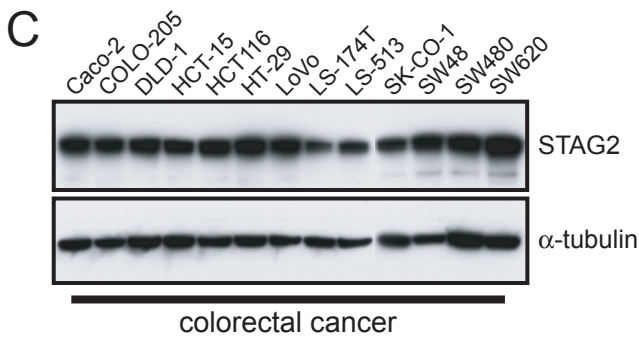
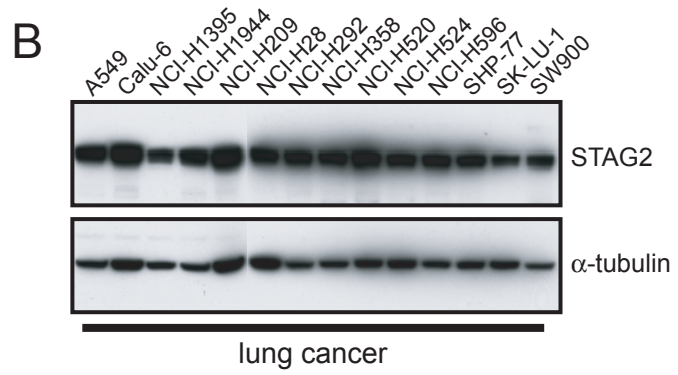
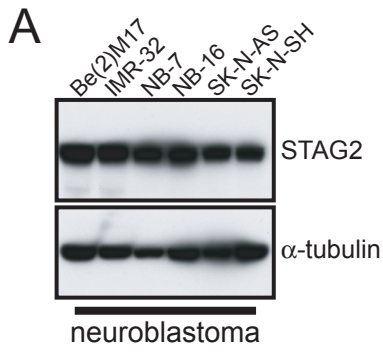


B

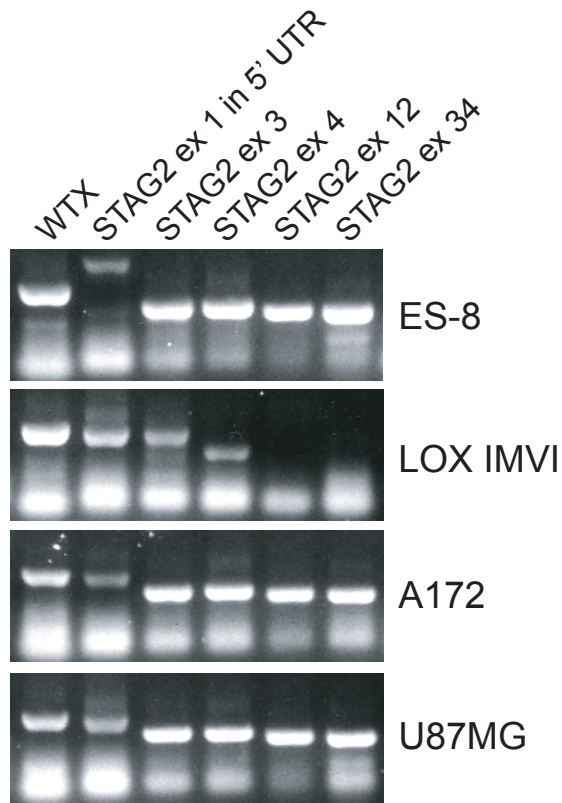




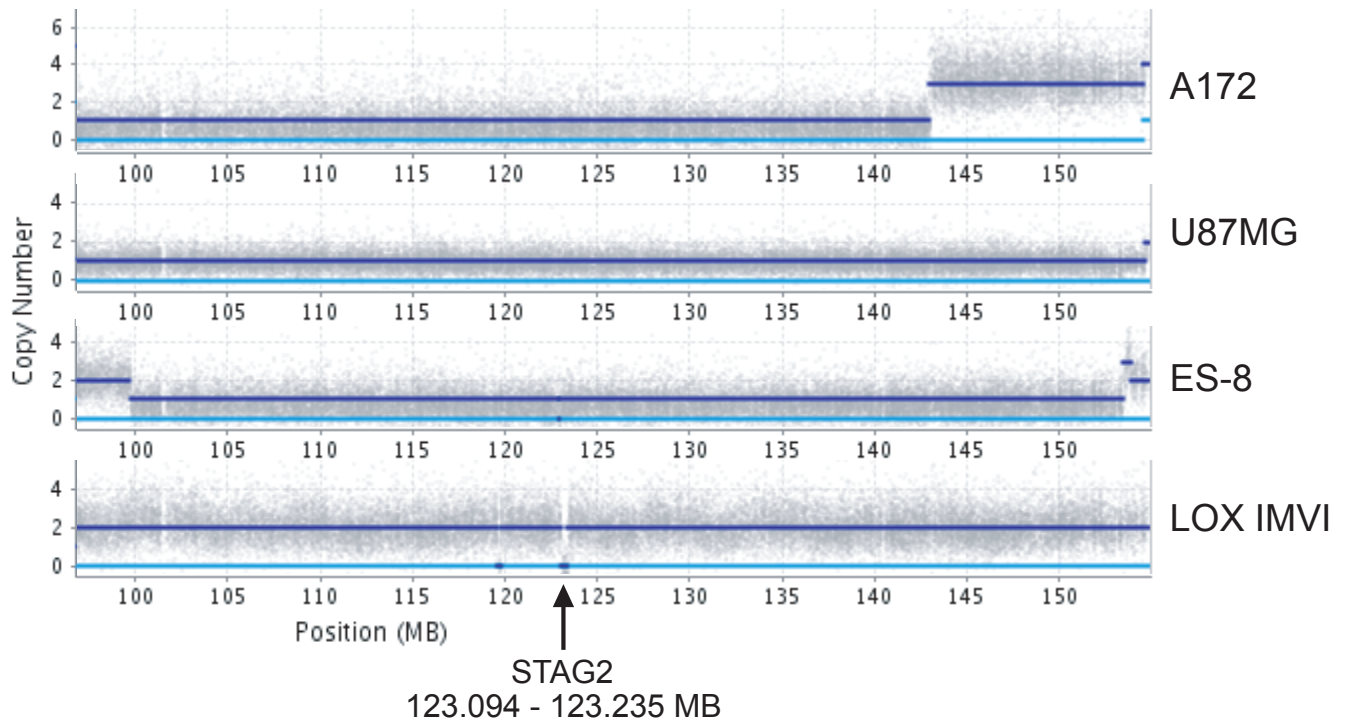
Supplementary Figure 5

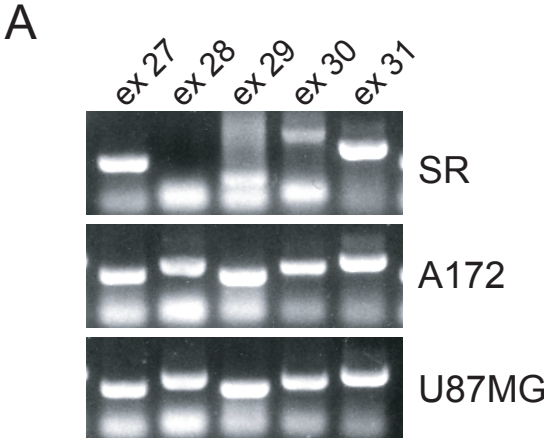


A



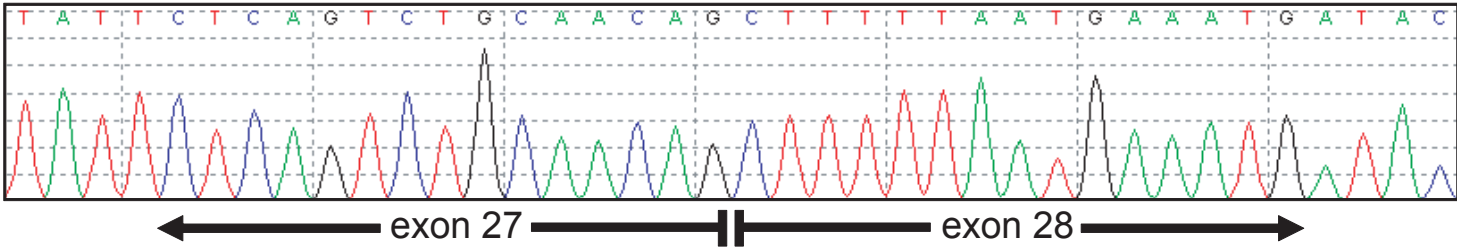
B



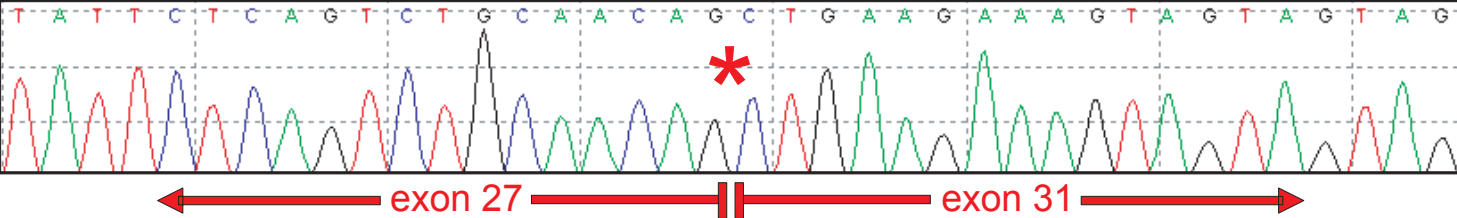


B

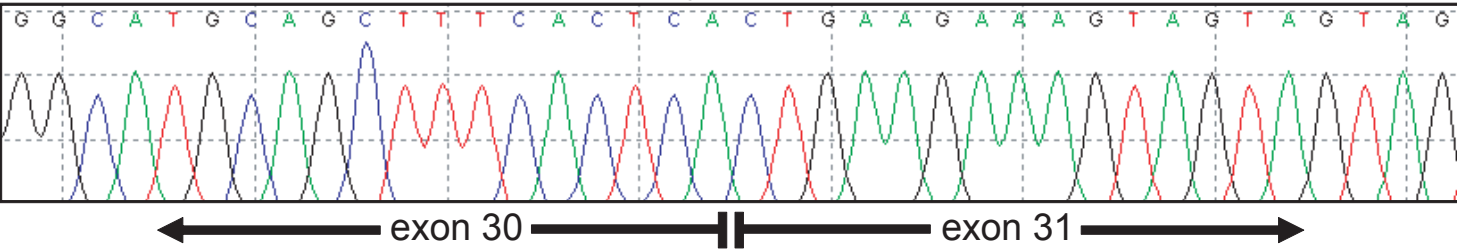
Reference mRNA over exon 27-28 splice junction



mRNA from SR cells

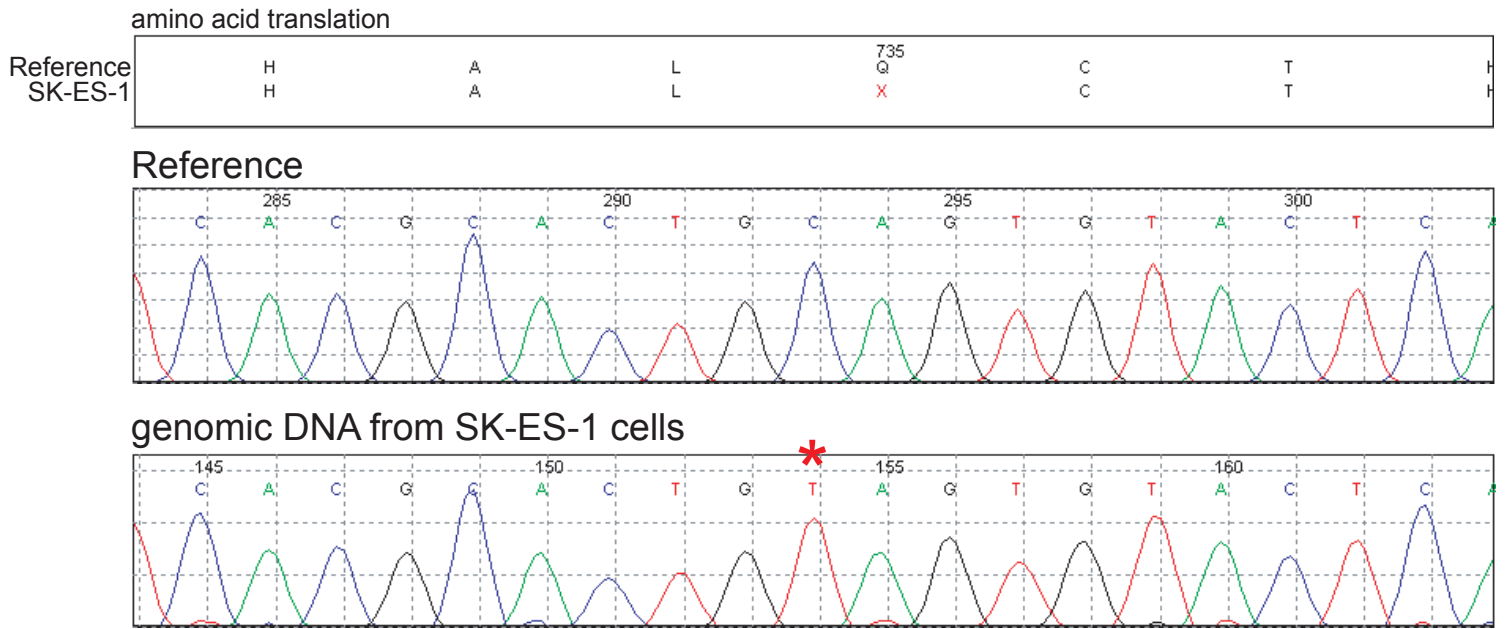


Reference mRNA over exon 30-31 splice junction

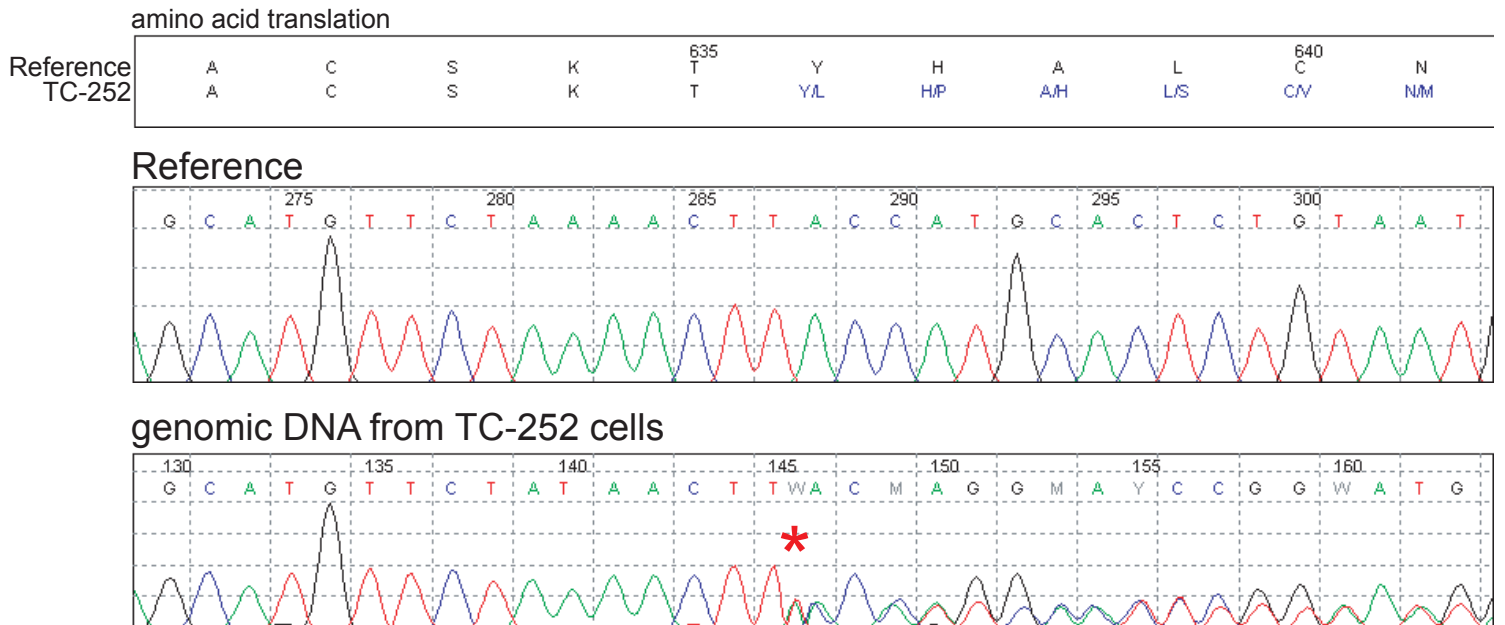


Supplementary Figure 8A-B

A



B



C

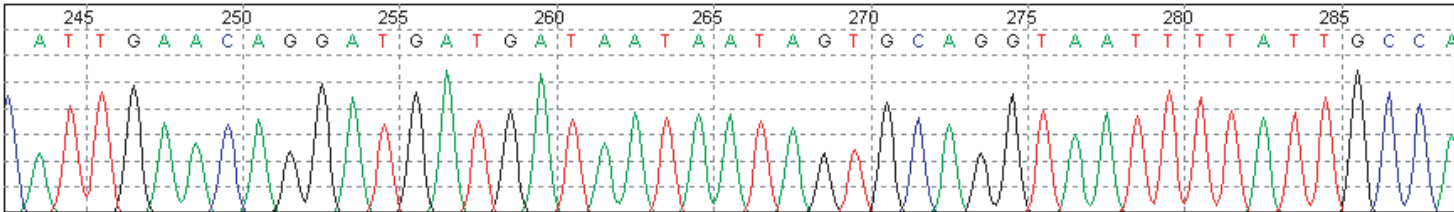
amino acid translation

Reference
A4573

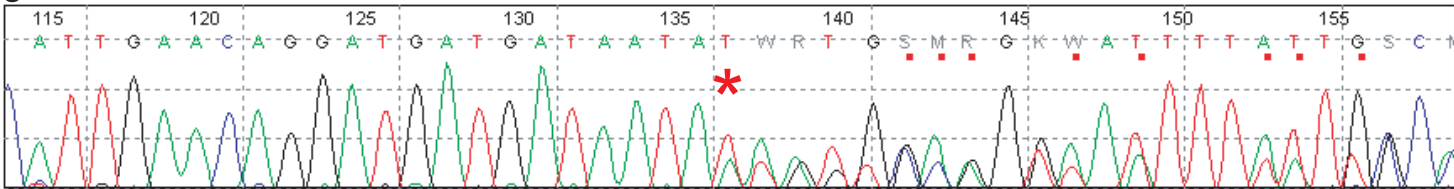
835	E	Q	D	D	840	N	N	S	A	D
I	E	Q	D	D	D	N	NI	SV	A	D

23]

Reference



genomic DNA from A4573 cells

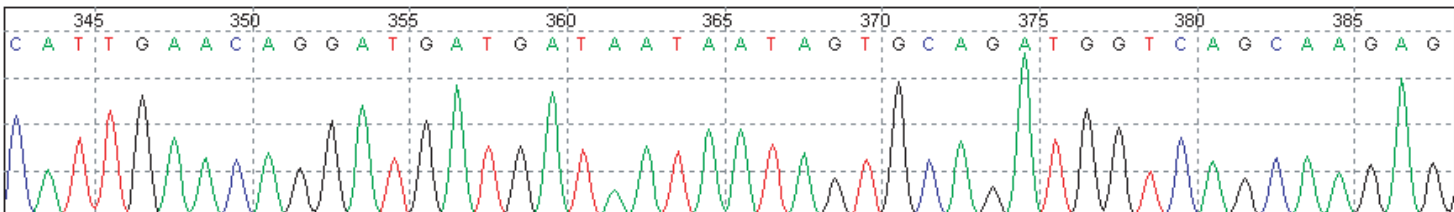


amino acid translation

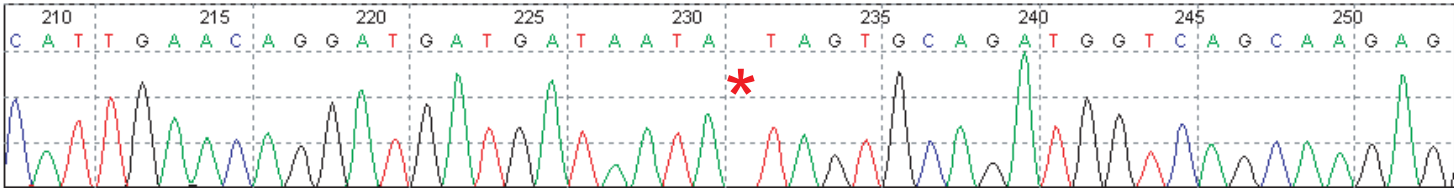
Reference
A4573

835	E	Q	D	D	840	N	N	S	A	845	G	Q	Q	E	
I	E	Q	D	D	D	N	I	V	Q	D	M	V	S	K	R

Reference

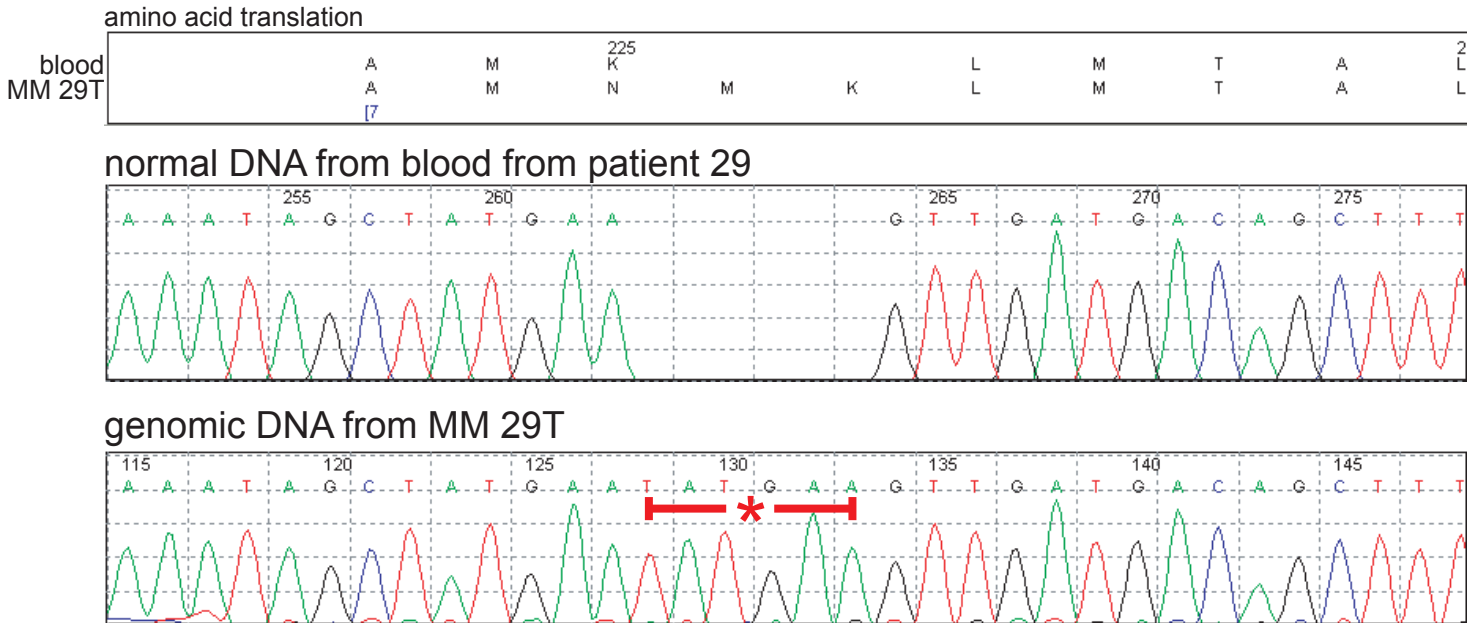


mRNA from A4573 cells

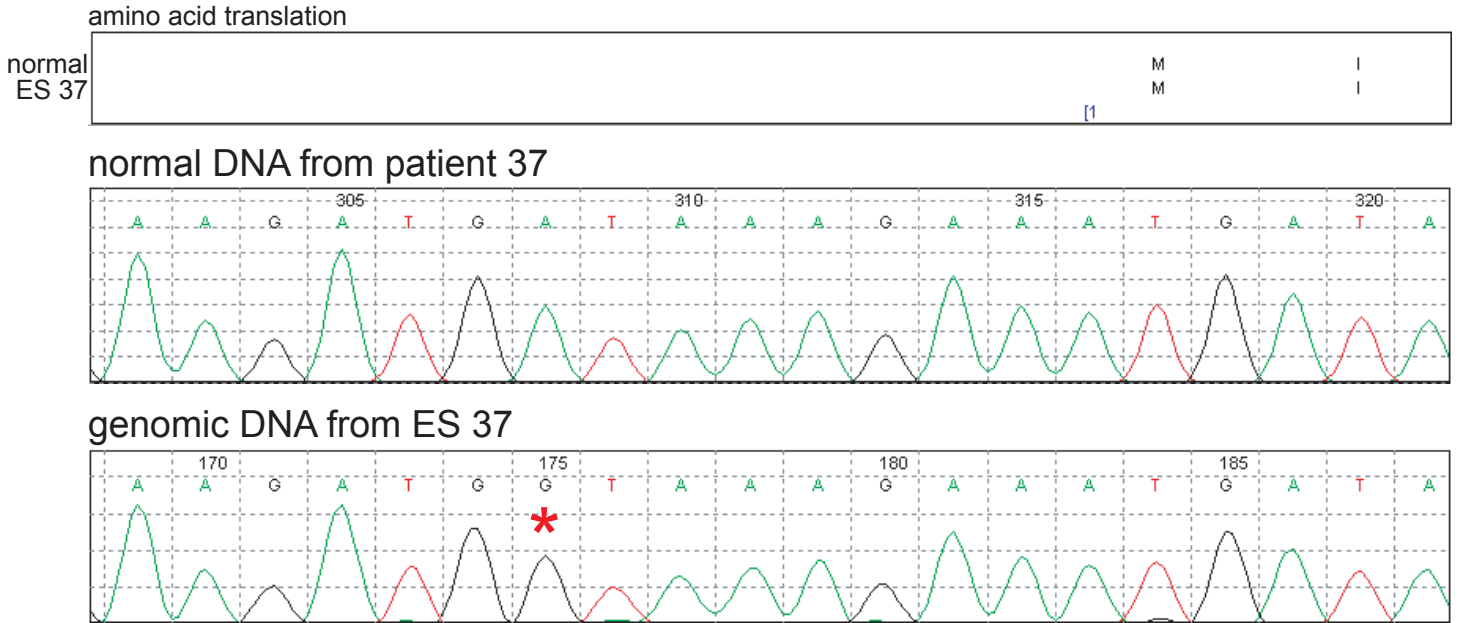


Supplementary Figure 9

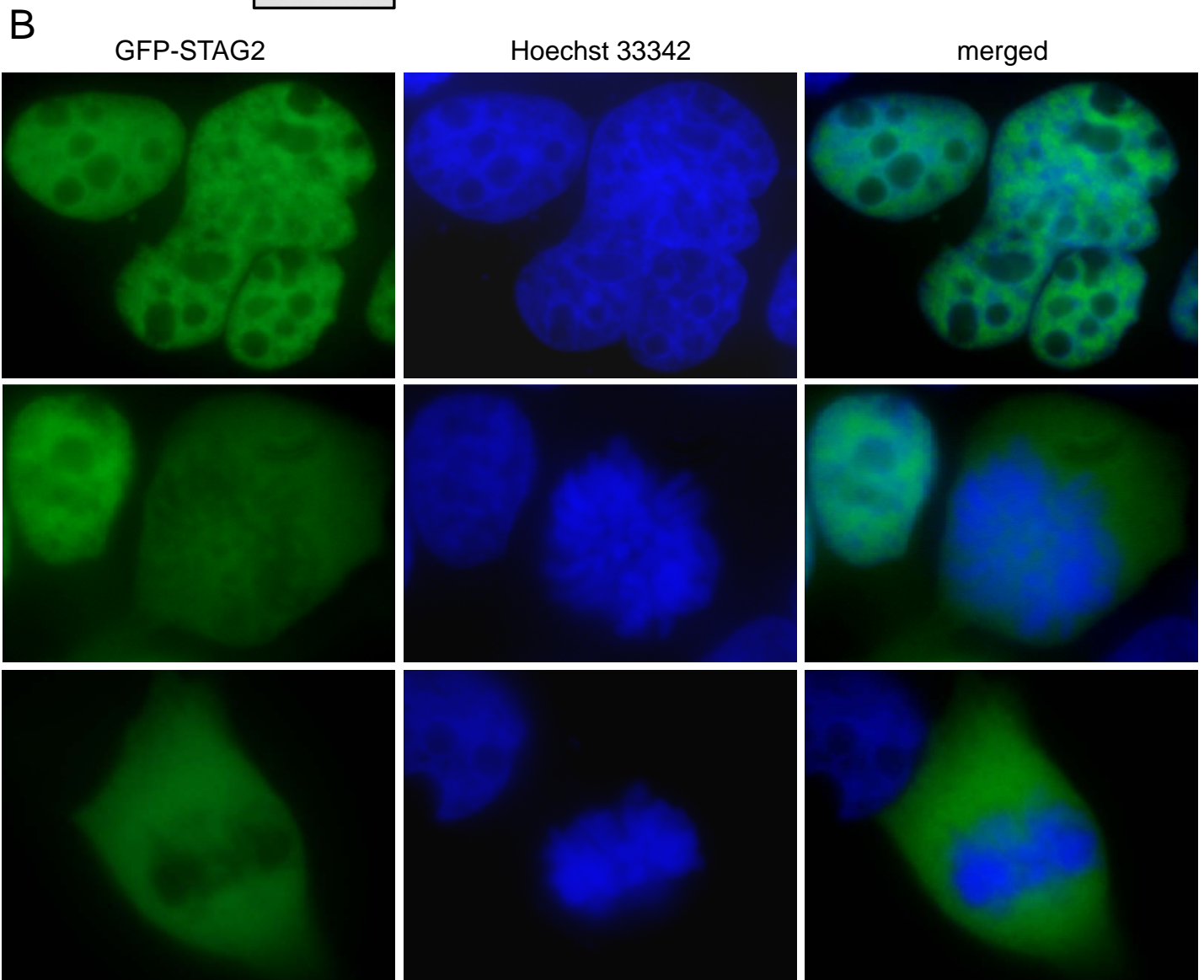
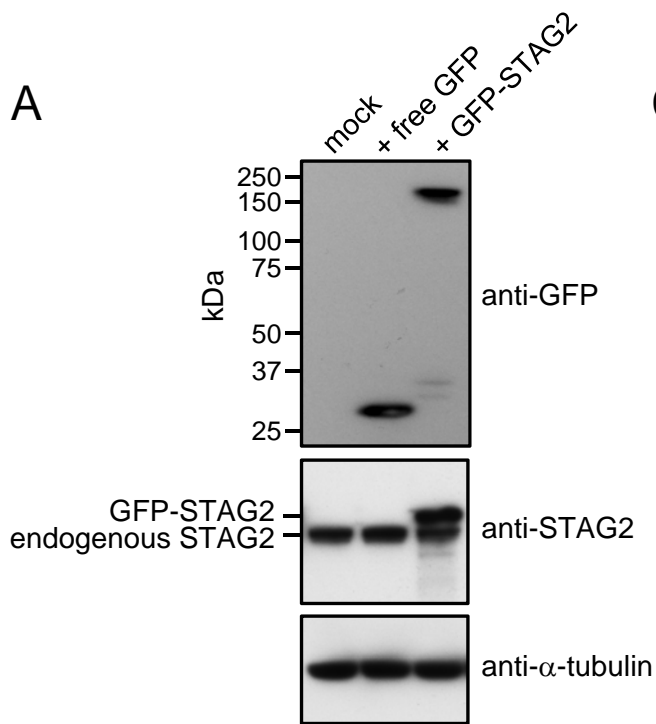
A



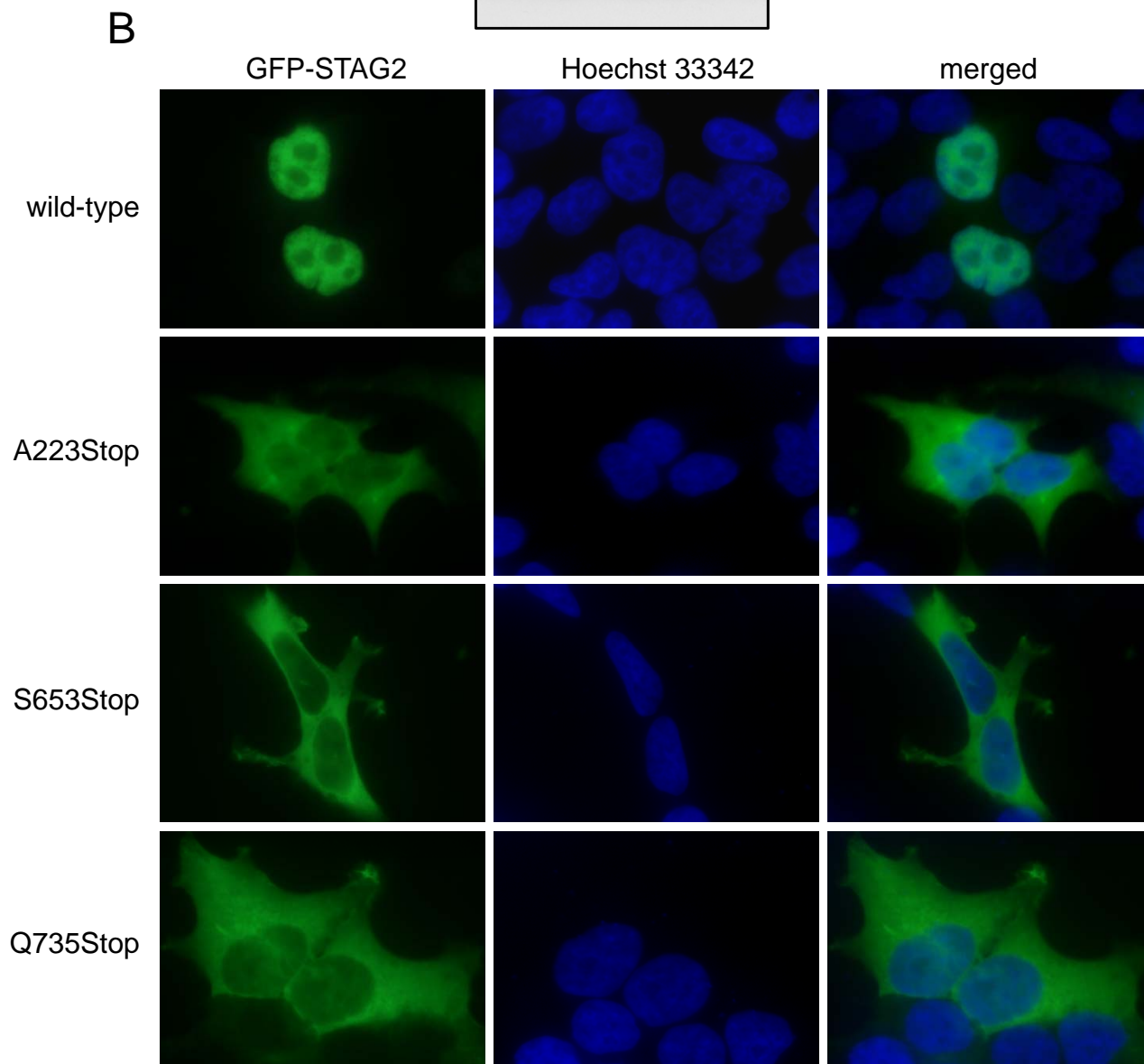
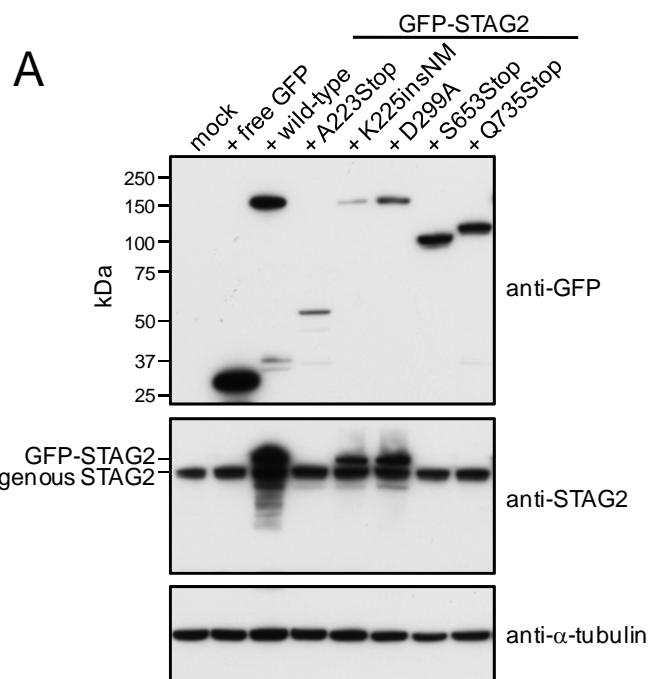
B



Supplementary Figure 10



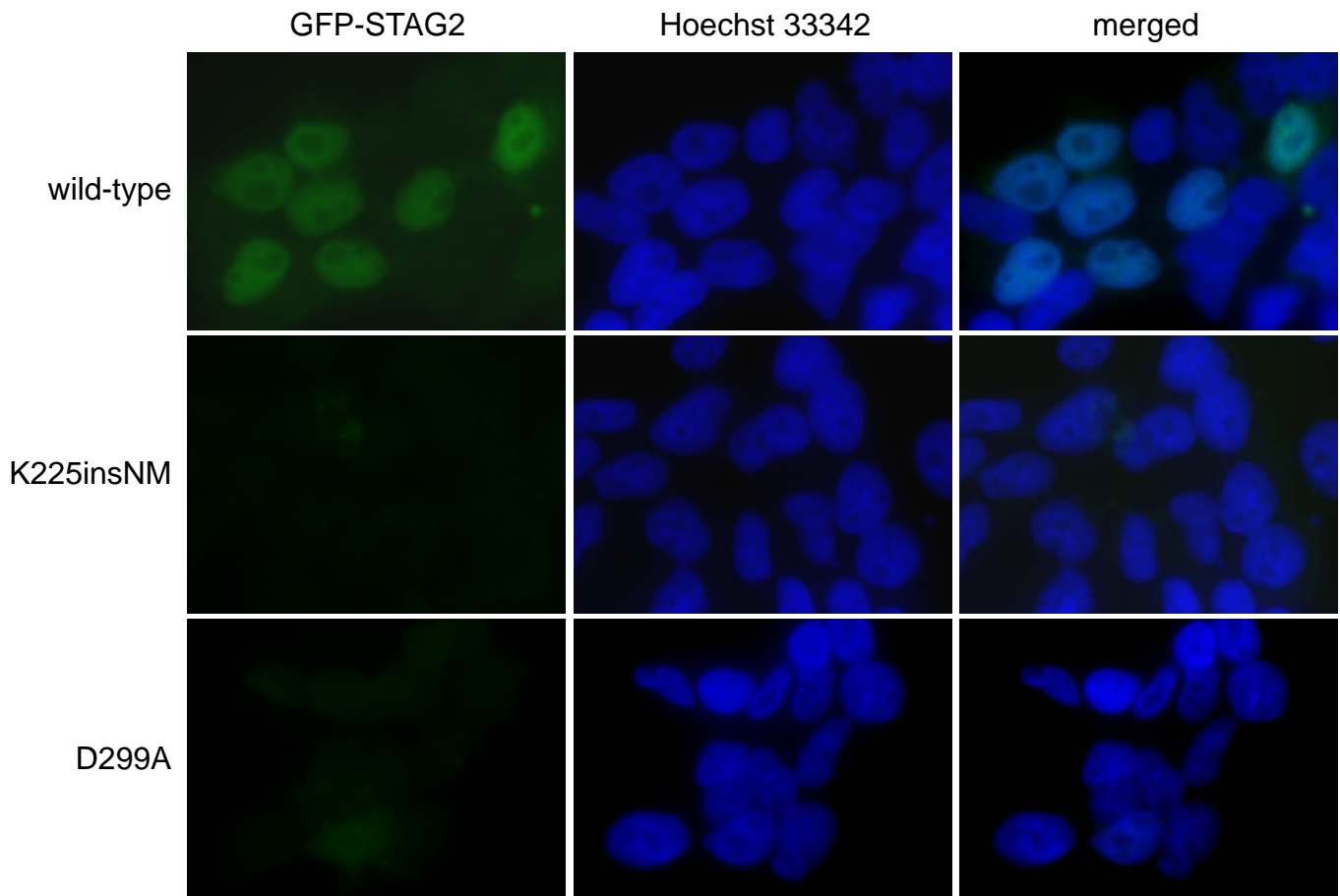
Supplementary Figure 11A-B



Supplementary Figure 11C

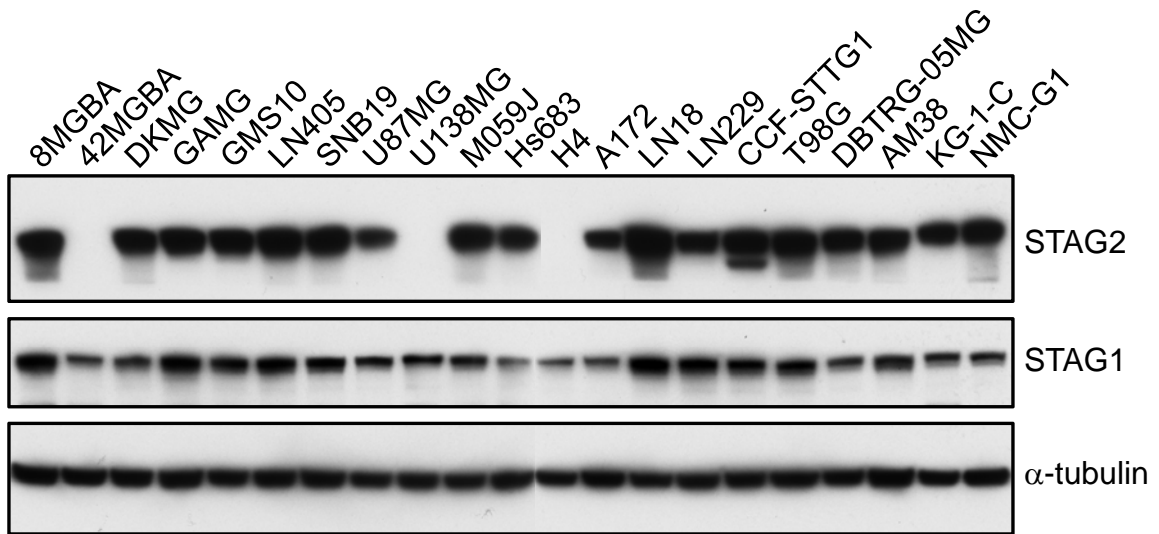
C

0.1% Triton X-100 extraction before fixation

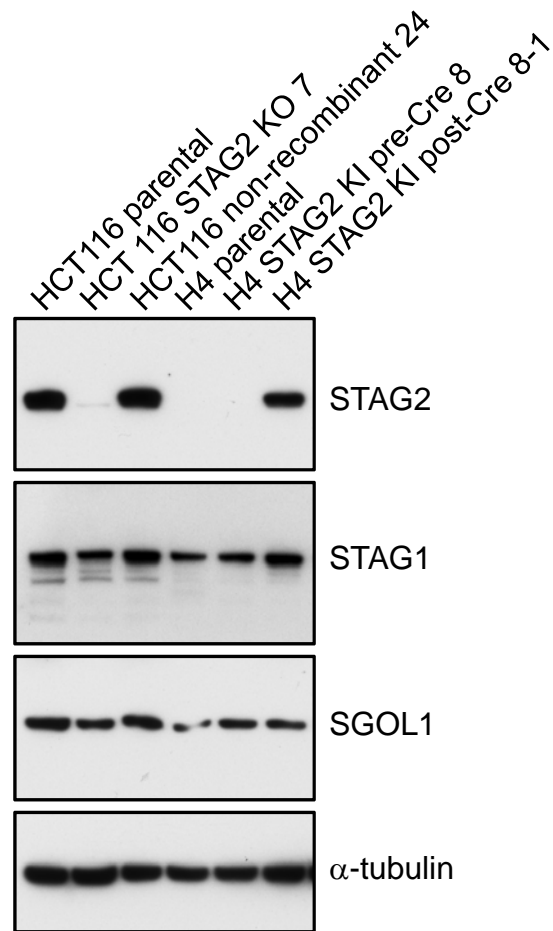


Supplementary Figure 12A-B

A



B

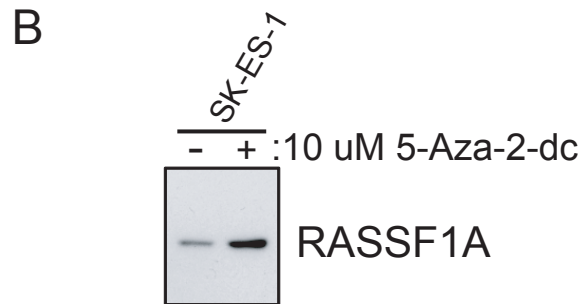
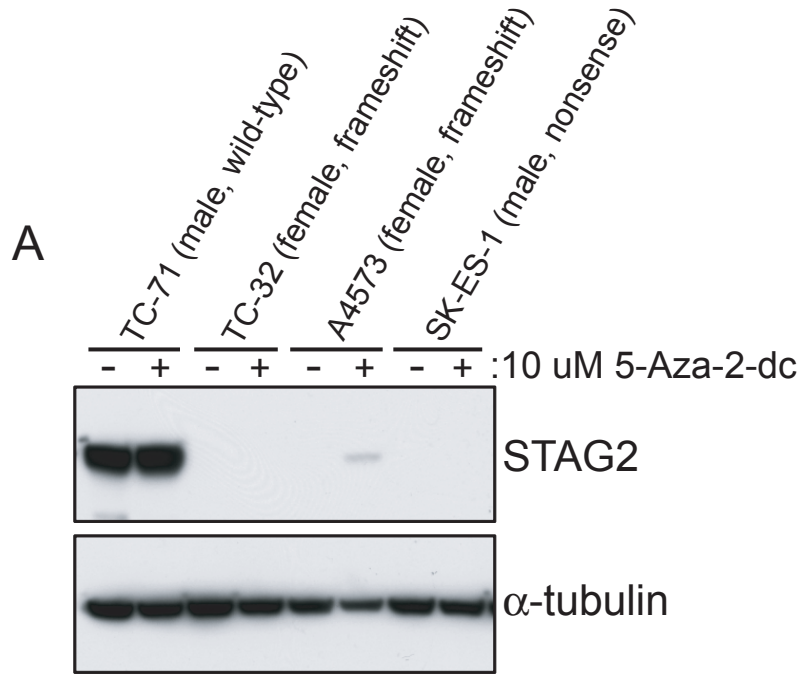


Supplementary Figure 12C

C

Gene ID	Gene name	Fold change in mRNA expression level		
		H4 STAG2 KI	42MGBA STAG2 KI	HCT116 STAG2 KO
STAG2	Stromal antigen 2	4.35	1.17	-5.97
STAG1	Stromal antigen 1	-1.23	-1.13	1.12
STAG3	Stromal antigen 3	-1.02	-1.06	1.03
SMC1A	Structural maintenance of chromosomes 1A	1.13	-1.06	-1.10
SMC1B	Structural maintenance of chromosomes 1B	-1.01	-1.14	1.09
SMC3	Structural maintenance of chromosomes 3	1.16	1.09	1.02
RAD21	Rad21 homolog	1.05	1.05	1.07
NIPBL	Nipped-B homolog	1.10	-1.09	1.25
PTTG1	Securin, Pituitary tumor transforming gene 1	1.05	-1.02	-1.08
ESCO1	Establishment of cohesion 1 homolog	-1.03	-1.02	1.18
ESPL1	Separase, Extra spindle poles-like 1	1.26	1.02	-1.05
PLK1	Polo-like kinase 1	-1.04	1.17	1.01
PDS5A	Regulator of cohesion maintenance homolog A	1.07	-1.01	-1.08
PDS5B	Regulator of cohesion maintenance homolog B	1.03	-1.04	1.04
WAPAL	Wings apart-like homolog	1.00	-1.00	-1.08
CDCA5	Sororin, Cell division cycle associated 5	-1.00	1.15	-1.19
SGOL1	Shugoshin-like 1	1.12	1.13	1.13
SGOL2	Shugoshin-like 2	1.13	-1.07	1.16

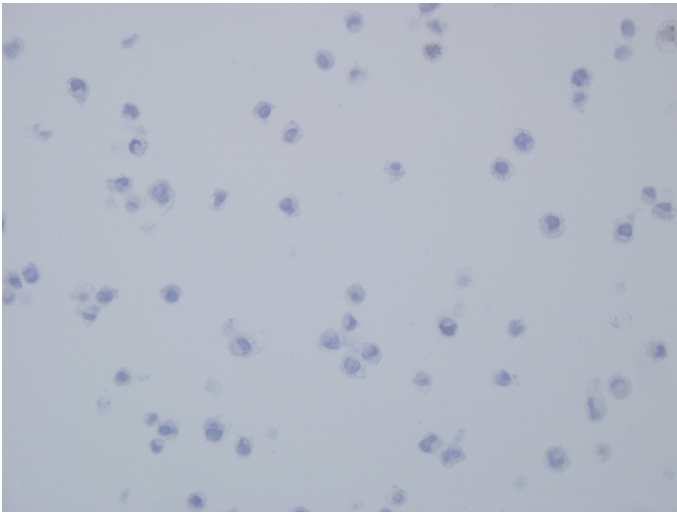
Supplementary Figure 13



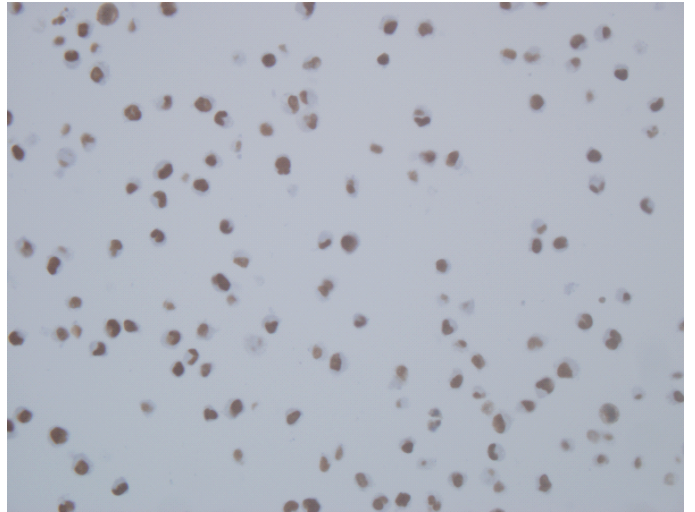
Supplementary Figure 14

A

H4 non-recombinant clone 10

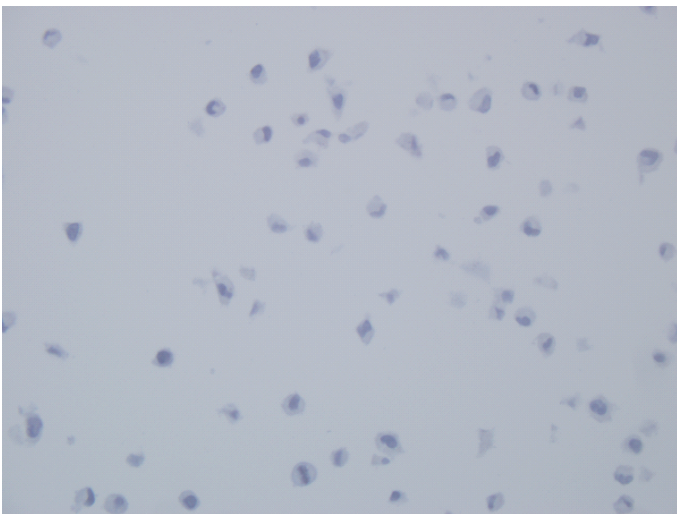


H4 STAG2 KI post-Cre clone 8-1



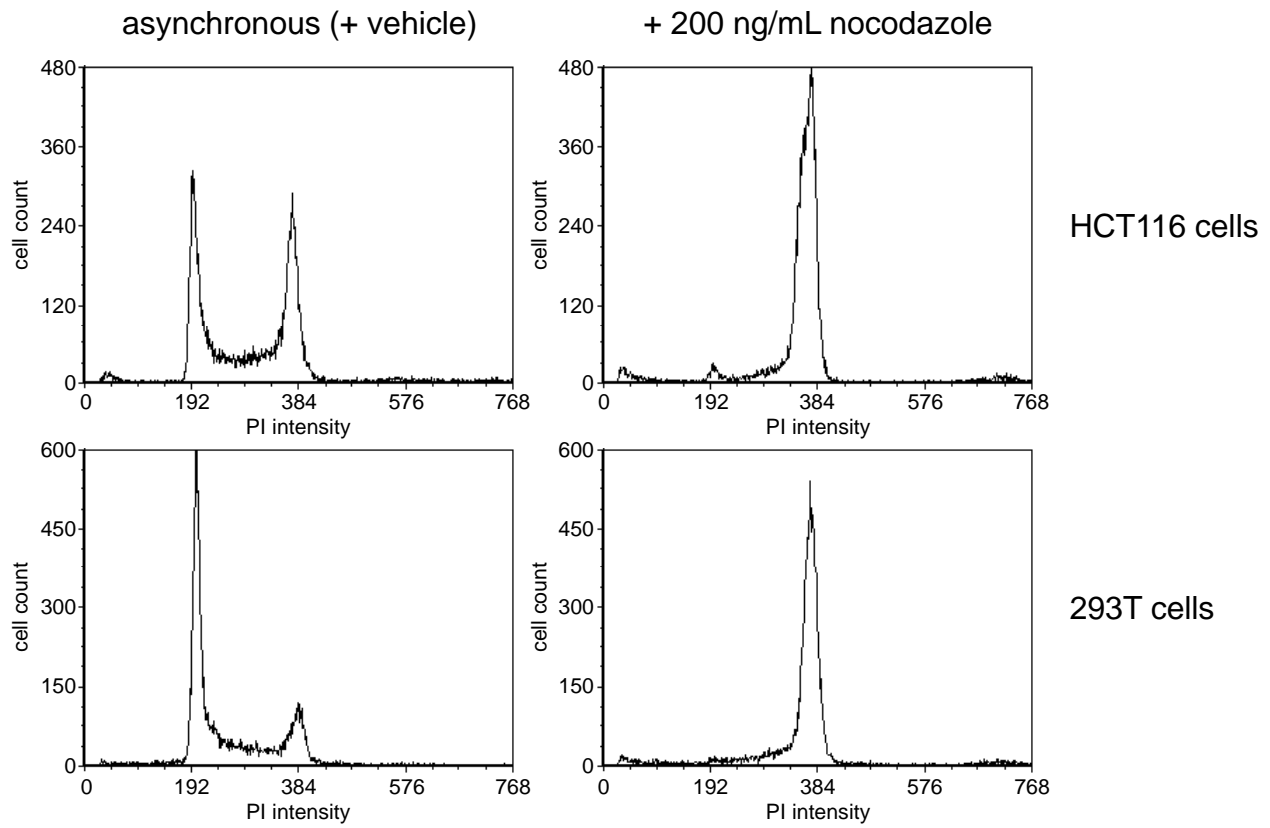
B

42MGBA cells

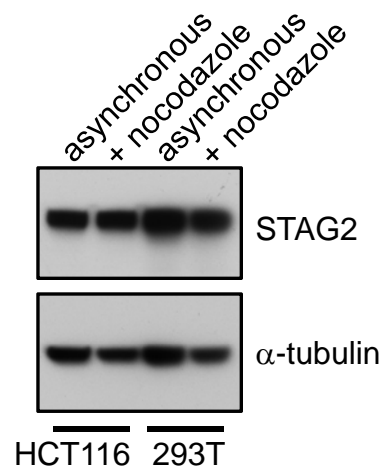


Supplementary Figure 15

A



B

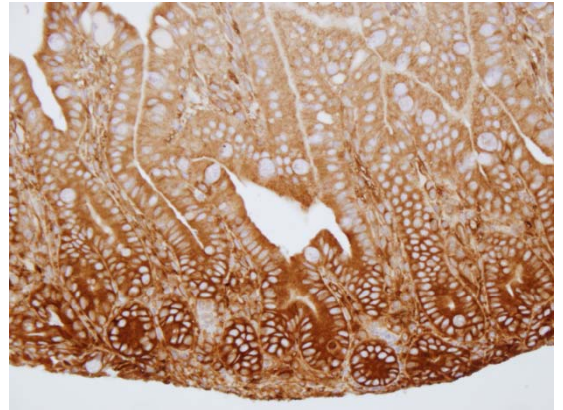
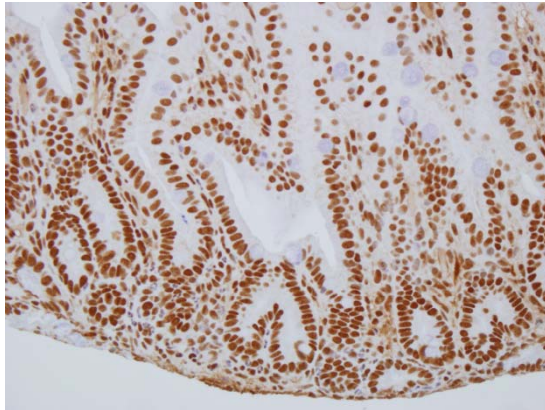


Supplementary Figure 16

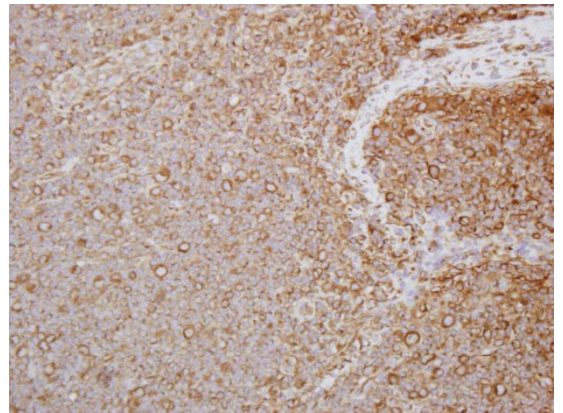
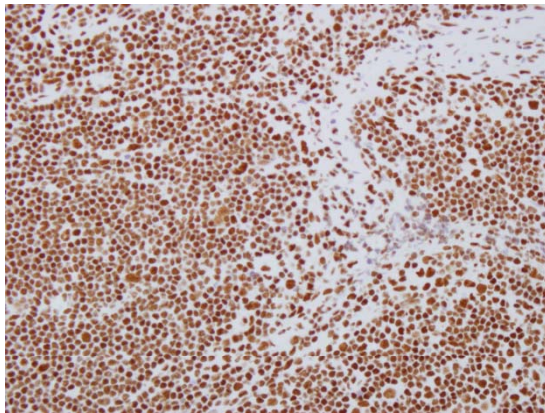
STAG2

α -tubulin

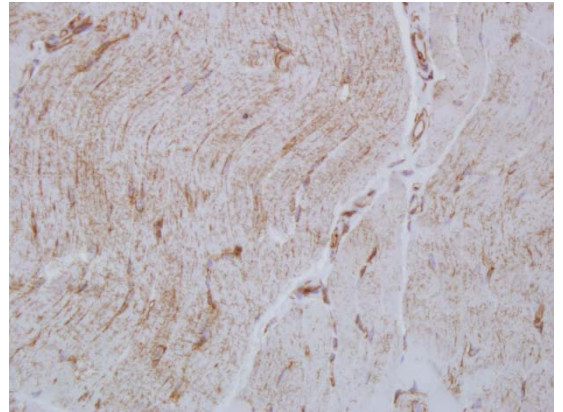
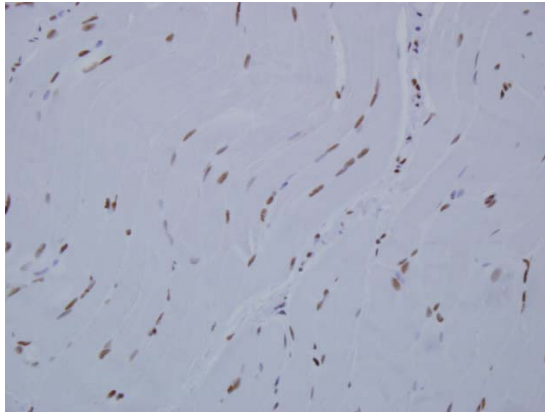
appendix



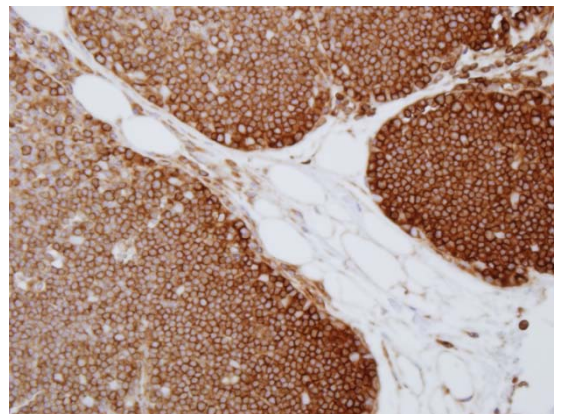
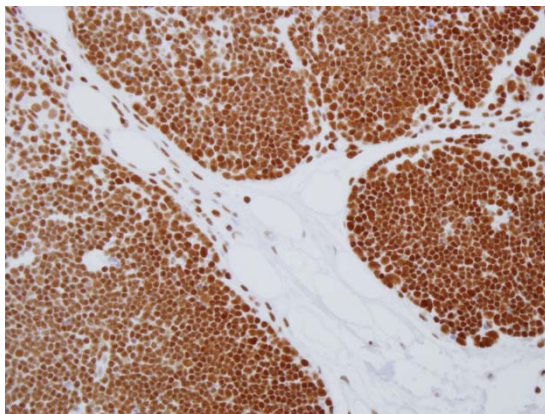
lymph node



skeletal muscle



thymus

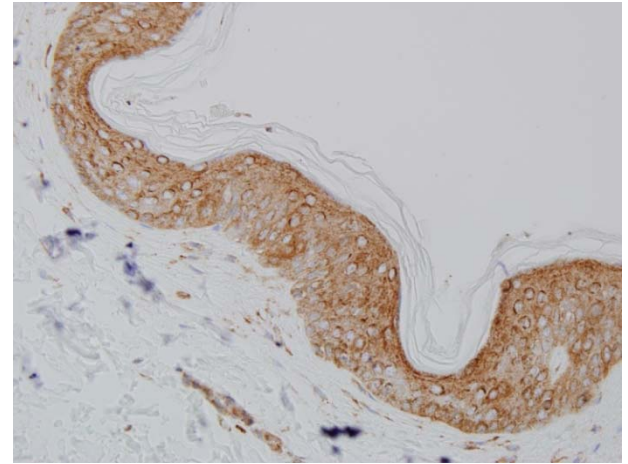
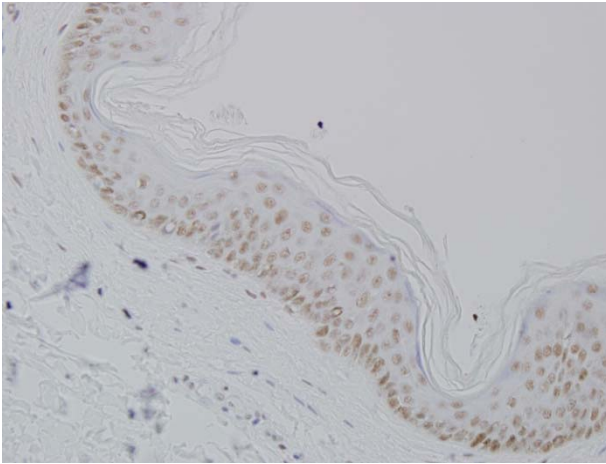


Supplementary Figure 16 continued

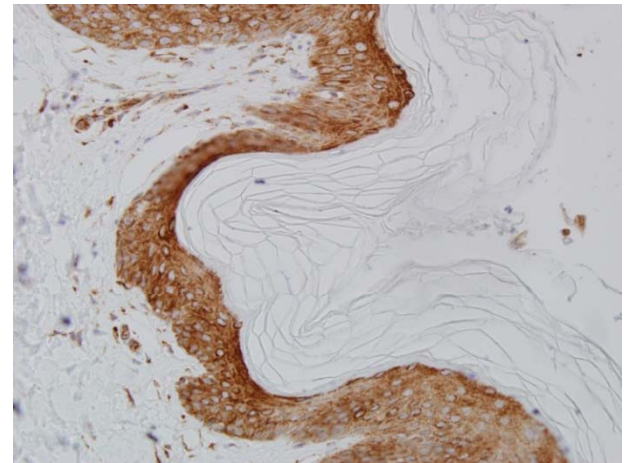
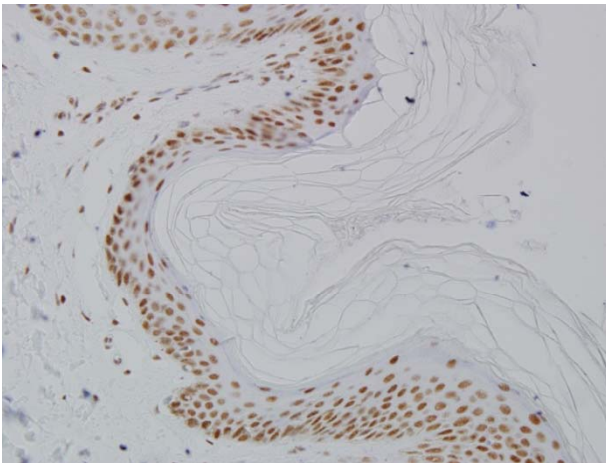
STAG2

α -tubulin

skin



skin



Supplementary Table 2

Tumor ID	Tissue array	Source	Pathology	Tissue site	Patient sex	Age at dx	# of replicate cores on TMA w/ STAG2 loss	Intratumoral heterogeneity of STAG2 loss
A7/A8	GL806	US Biomax	glioblastoma multiforme	cerebrum	M	20	2	no
B7/B8	GL806	US Biomax	glioblastoma multiforme	cerebrum	F	31	2	no
C9/C10	GL806	US Biomax	glioblastoma multiforme	cerebrum	M	44	2	no
E7/E8	GL806	US Biomax	glioblastoma multiforme	cerebrum	M	40	2	no
F1/F2	GL806	US Biomax	glioblastoma multiforme	cerebrum	F	41	2	no
F9/F10	GL806	US Biomax	glioblastoma multiforme	cerebrum	M	50	2	no
D9/D10	ME1002	US Biomax	melanoma	perianal skin	F	47	2	no
E1/E2	ME1002	US Biomax	melanoma	skin (heel)	M	62	2	no
F5/F6	ME1002	US Biomax	melanoma	vulva	F	52	2	no
G1/G2	ME1002	US Biomax	melanoma	skin (back)	M	36	2	no
G7/G8	ME1002	US Biomax	melanoma	dorsum of foot	M	35	2	no
H5/H6	ME1002	US Biomax	melanoma	perianal skin	M	45	2	no
H9/H10	ME1002	US Biomax	melanoma	vulva	F	45	2	no
A11/B11	LY1501	US Biomax	lymphoma, diffuse B-cell	left neck	F	48	2	yes
B4/B5/B6	BC17012	US Biomax	medulloblastoma	brain, 4th ventricle	M	11	3	no
CA7/DA7	CO1922	US Biomax	adenocarcinoma	colon	M	37	2	no
CD1/DD1	CO1922	US Biomax	adenocarcinoma	colon	F	66	2	no
A2/D4/F4	ES-1	Marc Ladanyi	Ewing's sarcoma	abdominal wall	F	72	3	no
A3/B3/C3	ES-1	Marc Ladanyi	Ewing's sarcoma	lumbar spine	M	25	3	no
D2/E2/F2	ES-1	Marc Ladanyi	Ewing's sarcoma	pubis	F	21	3	no
D8/E8/F8	ES-1	Marc Ladanyi	Ewing's sarcoma	tibia	M	15	3	no
G4/H4/I4	ES-1	Marc Ladanyi	Ewing's sarcoma	shoulder	F	30	3	no
H6/I6	ES-1	Marc Ladanyi	Ewing's sarcoma	fibula	M	10	2	no
G11/H11/I11	ES-1	Marc Ladanyi	Ewing's sarcoma	leg	F	34	3	yes
2004-06-P0309	3000-30-P8798	Children's Oncology Group	Ewing's sarcoma	right chest	F	17	3	no
97-06-P046	3000-30-P8798	Children's Oncology Group	Ewing's sarcoma	rib	M	14	1	yes
2005-09-P0748	3000-30-P8798	Children's Oncology Group	Ewing's sarcoma	pelvis	M	22	5	no
97-08-P076	3000-30-P8798	Children's Oncology Group	Ewing's sarcoma	right femur	M	11	1	no

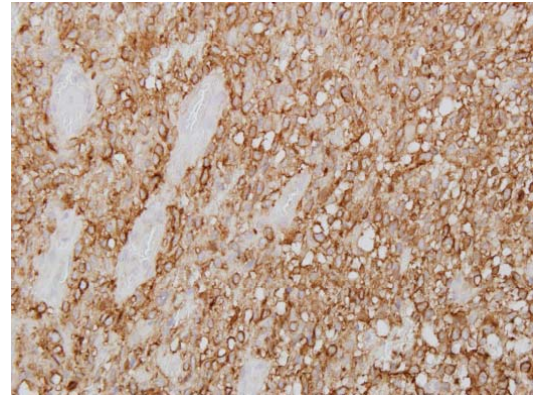
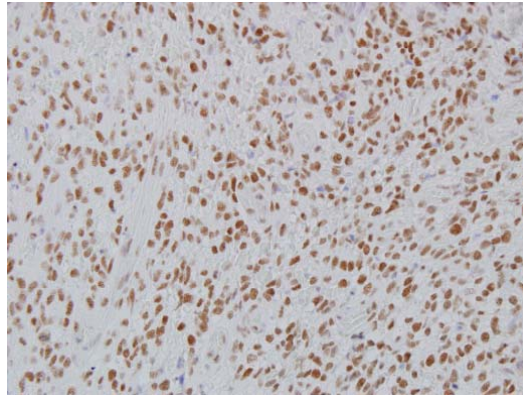
Evidence for somatic nature of STAG2 loss
Adjacent normal brain on original tumor block is STAG2 positive.
Admixed non-neoplastic perivascular endothelial cells are STAG2 positive.
Admixed non-neoplastic lymphocytes are STAG2 positive.
Adjacent normal brain on original tumor block is STAG2 positive.
Stroma and adjacent normal skin on original tumor block are STAG2 positive.
Adjacent block of non-neoplastic skin is STAG2 positive.
Intratumoral heterogeneity.
Admixed non-neoplastic perivascular endothelial cells are STAG2 positive.
Stroma and admixed non-neoplastic perivascular endothelial cells are STAG2 positive.
Stroma and admixed non-neoplastic lymphocytes and perivascular endothelial cells are STAG2 positive.
Admixed non-neoplastic perivascular endothelial cells are STAG2 positive.
Admixed non-neoplastic perivascular endothelial cells are STAG2 positive.
Stromal fibroblasts are STAG2 positive.
Intratumoral heterogeneity.
Admixed non-neoplastic perivascular endothelial cells are STAG2 positive.
Intratumoral heterogeneity.
Admixed non-neoplastic perivascular endothelial cells are STAG2 positive.
Block of non-neoplastic tissue from patient is STAG2 positive.

Supplementary Figure 17

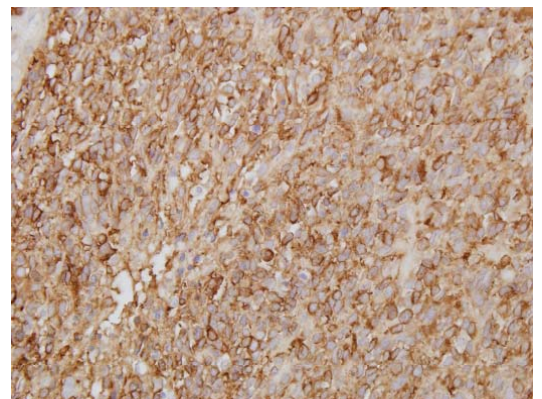
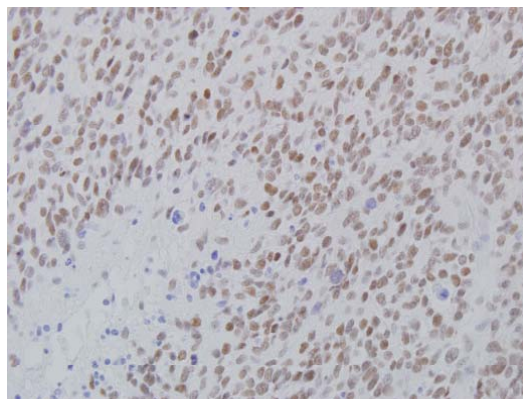
STAG2

α -tubulin

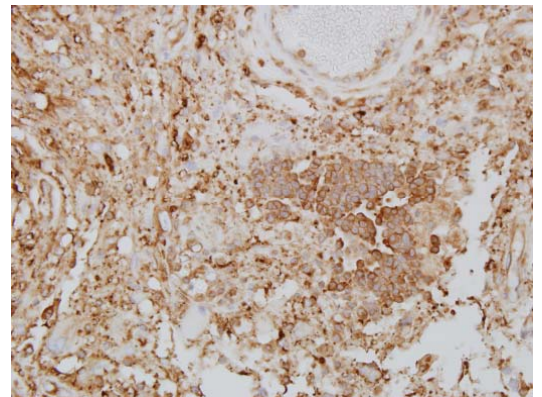
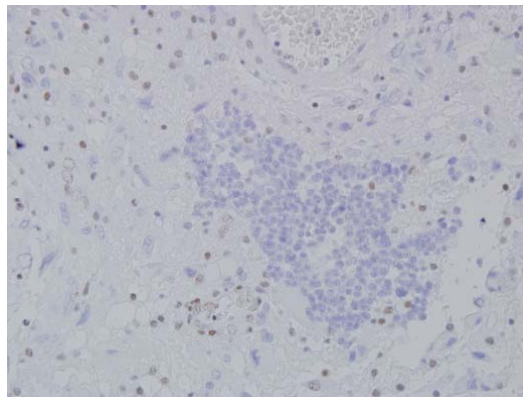
glioblastoma A2
STAG2 (+)



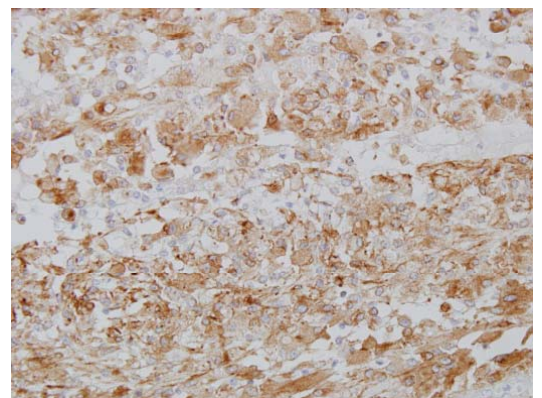
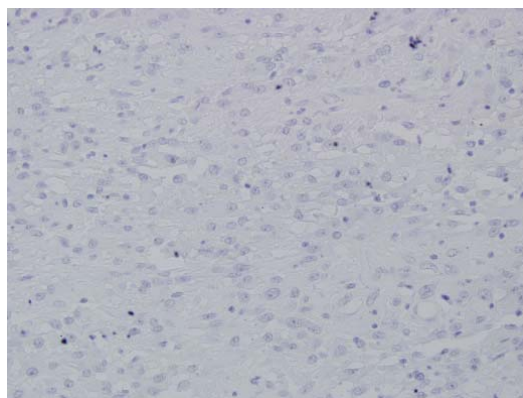
glioblastoma E10
STAG2 (+)



glioblastoma C10
STAG2 (-)



glioblastoma F2
STAG2 (-)

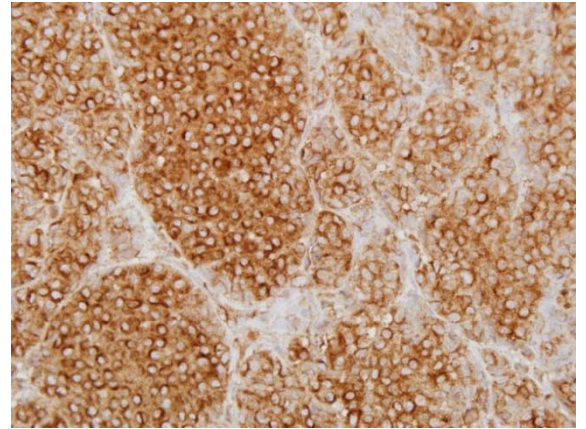
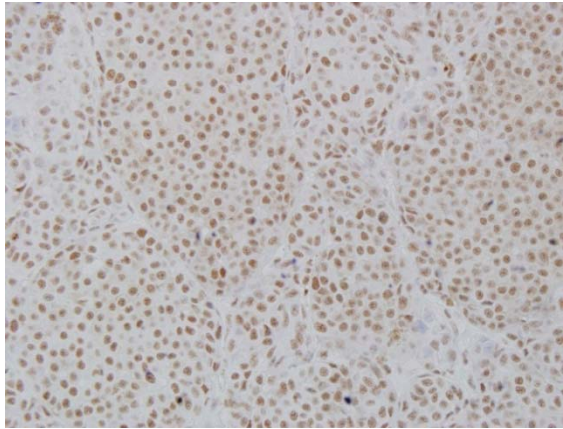


Supplementary Figure 18

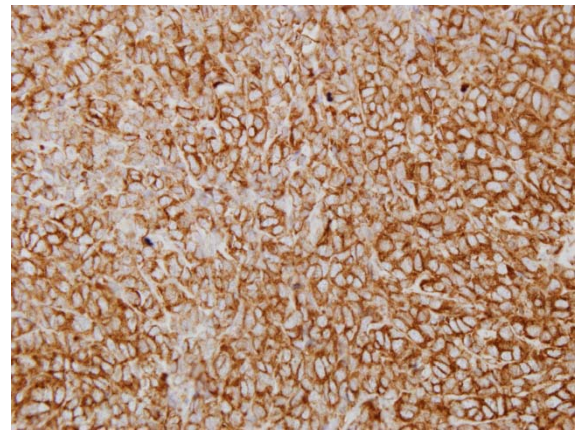
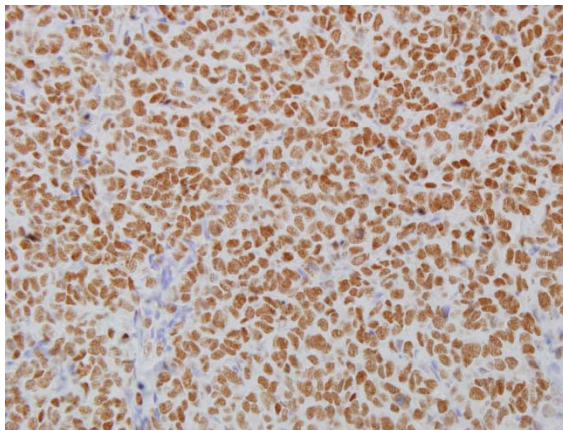
STAG2

α -tubulin

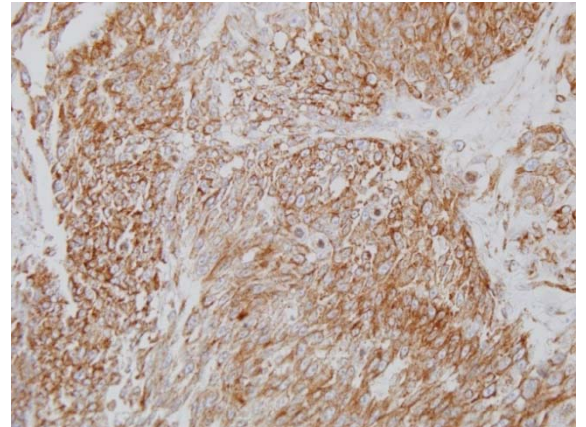
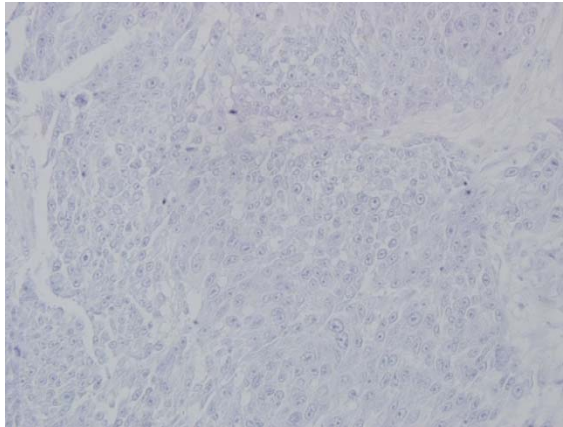
melanoma A2
STAG2 (+)



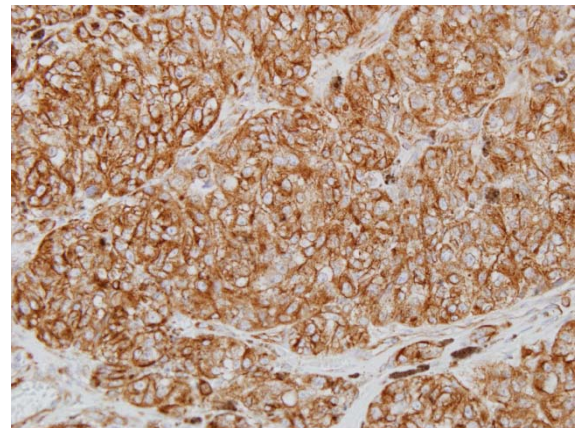
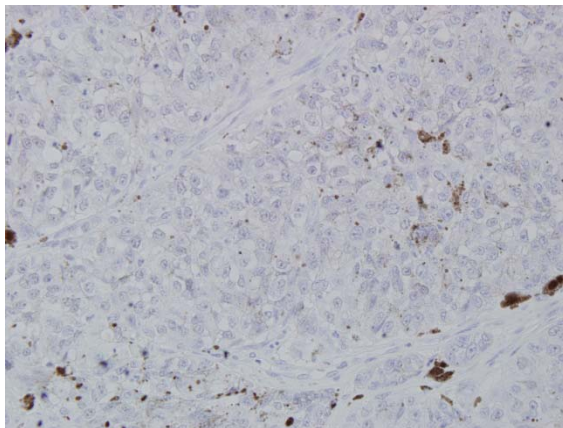
melanoma H7
STAG2 (+)



melanoma D9
STAG2 (-)



melanoma E1
STAG2 (-)

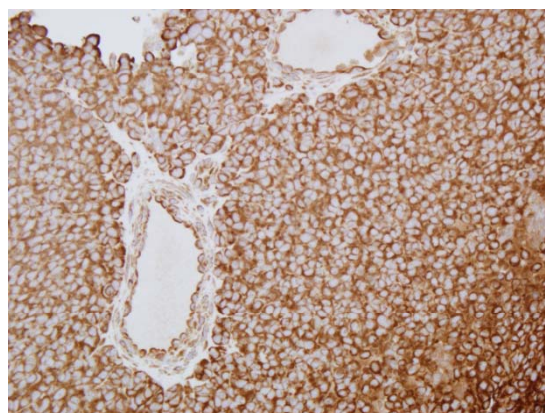
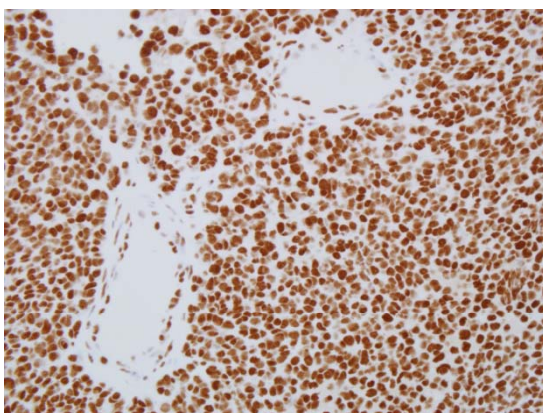


Supplementary Figure 19

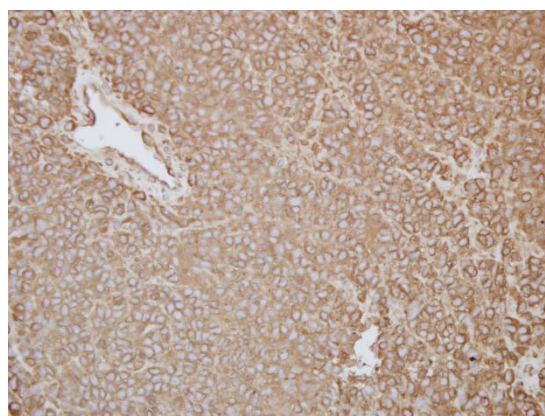
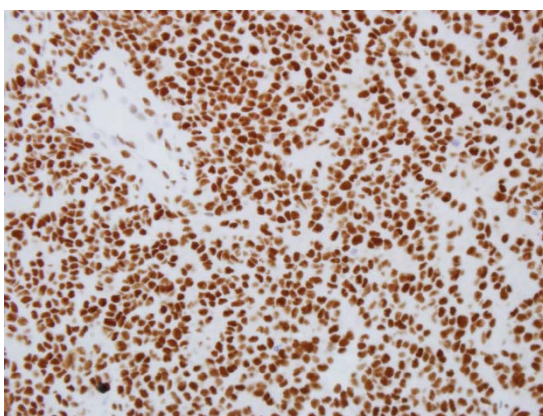
STAG2

α -tubulin

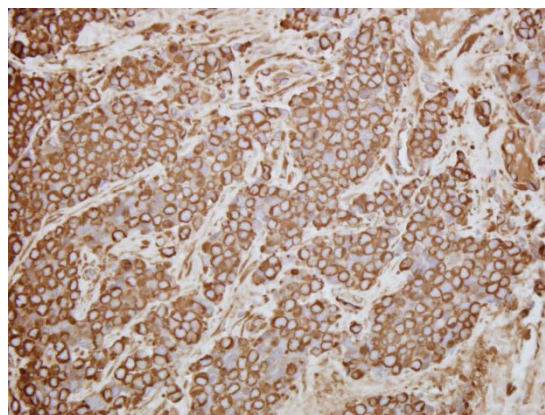
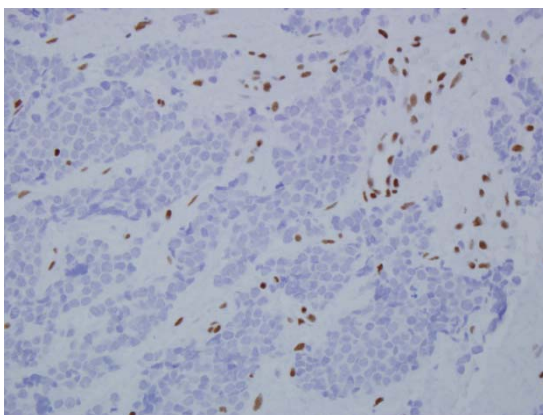
Ewing's P0253
STAG2 (+)



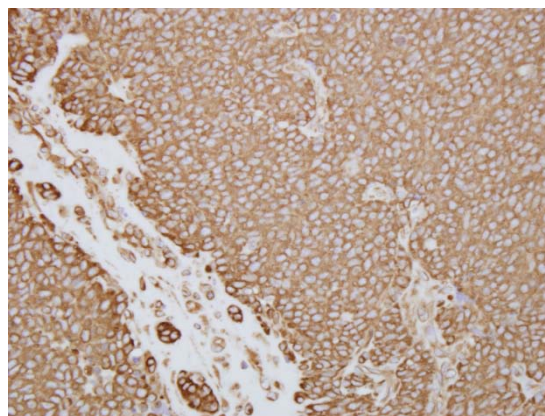
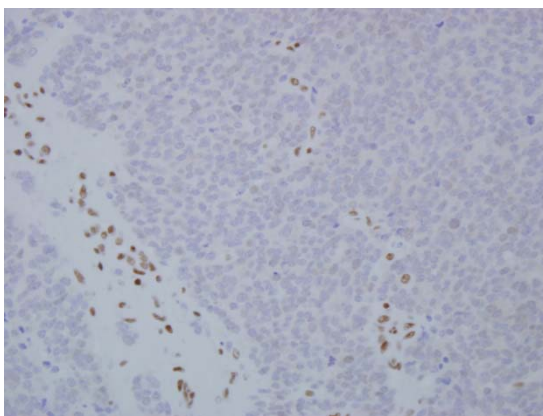
Ewing's P1013
STAG2 (+)



Ewing's P0309
STAG2 (-)



Ewing's P0748
STAG2 (-)

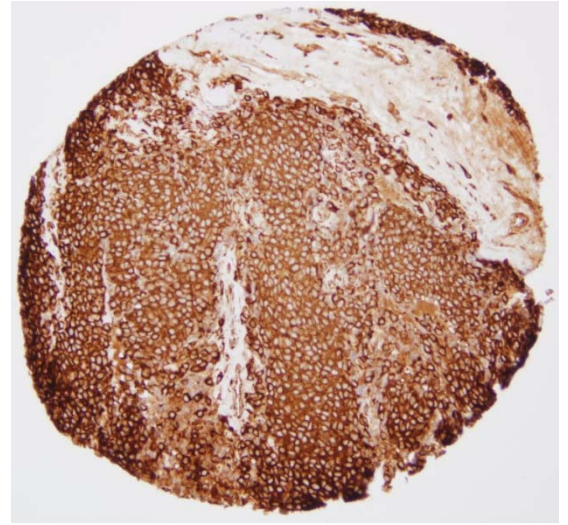
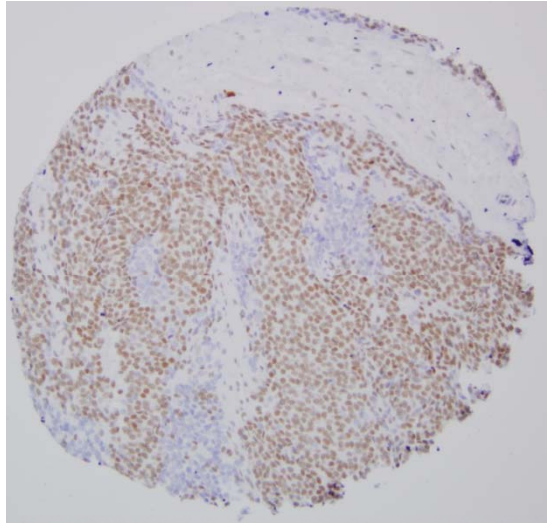


Supplementary Figure 20

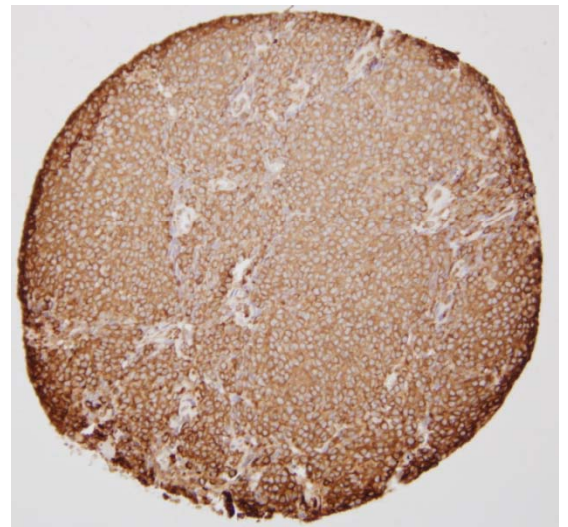
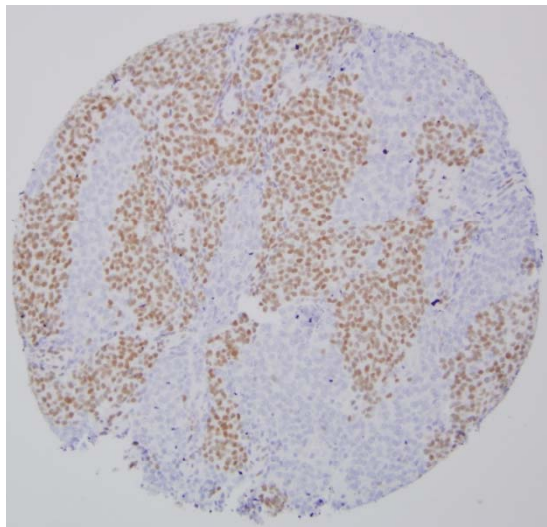
STAG2

α -tubulin

Ewing's G11
STAG2 (+/-)



Ewing's H11
STAG2 (+/-)

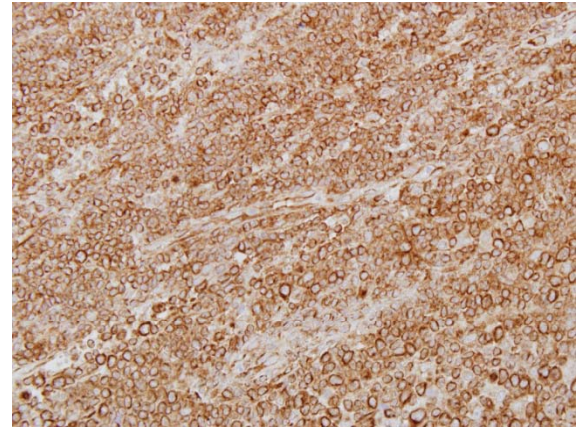
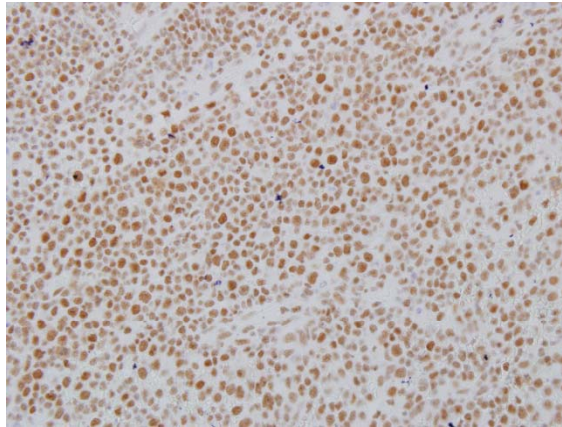


Supplementary Figure 21

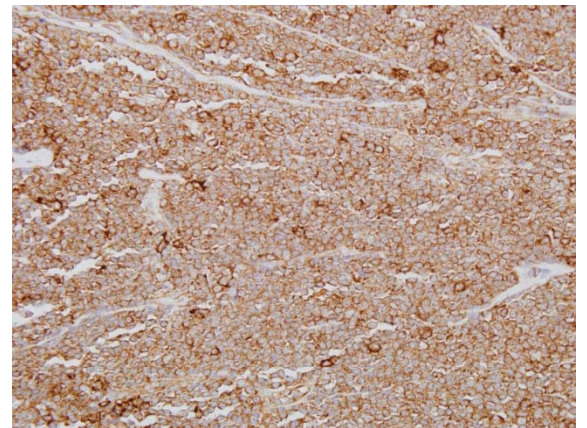
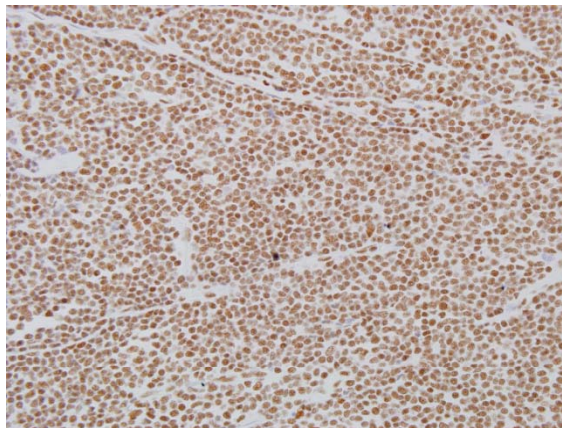
STAG2

α -tubulin

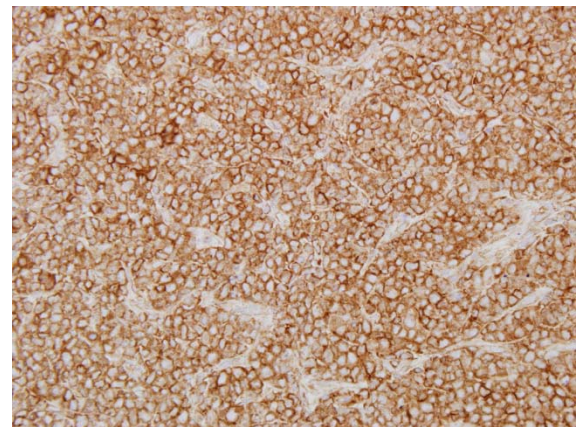
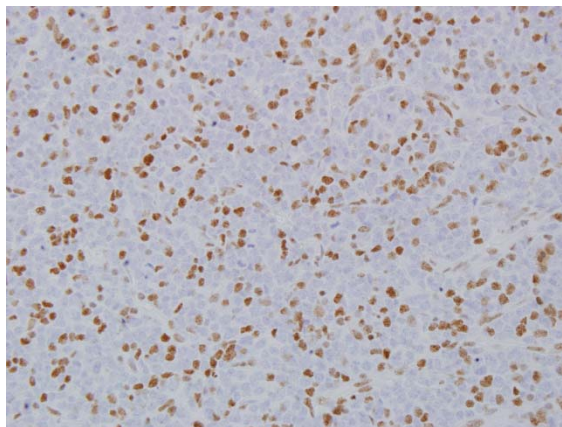
lymphoma A2
STAG2 (+)



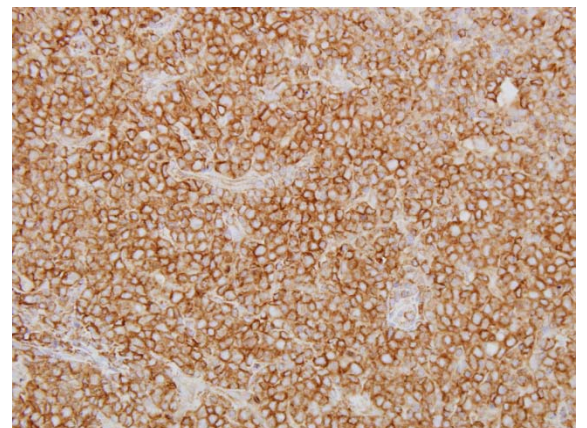
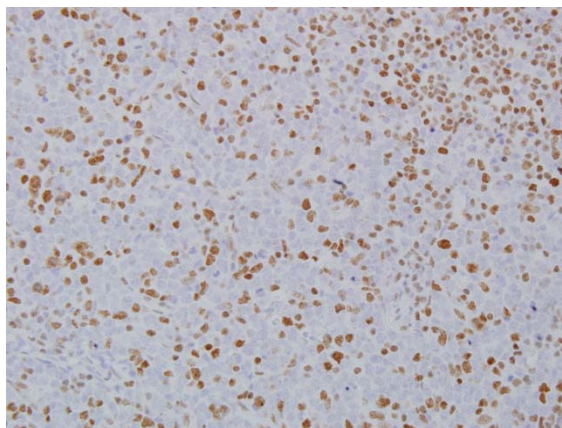
lymphoma G3
STAG2 (+)



lymphoma A11
STAG2 (+/-)



lymphoma B11
STAG2 (+/-)

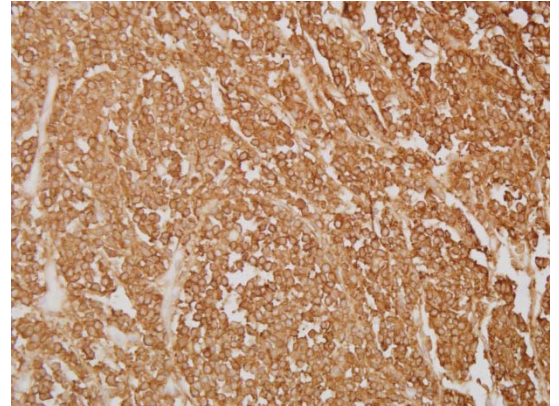
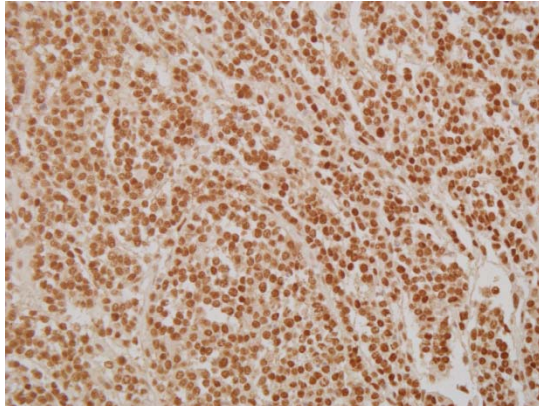


Supplementary Figure 22

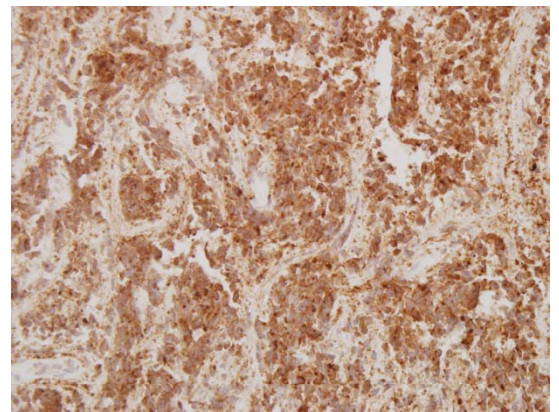
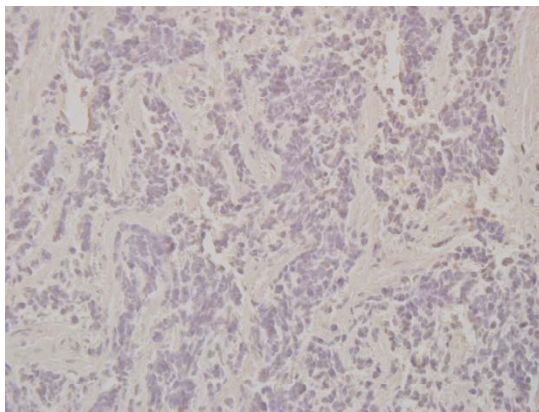
STAG2

α -tubulin

medulloblastoma A3
STAG2 (+)



medulloblastoma D7
STAG2 (-)

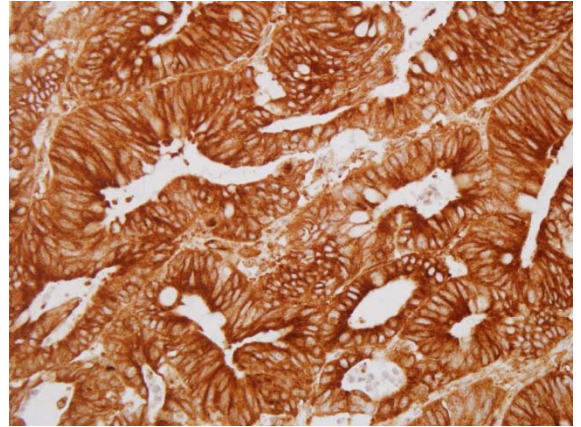
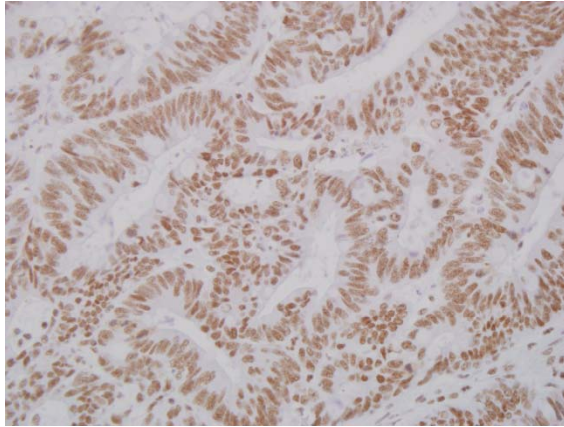


Supplementary Figure 23

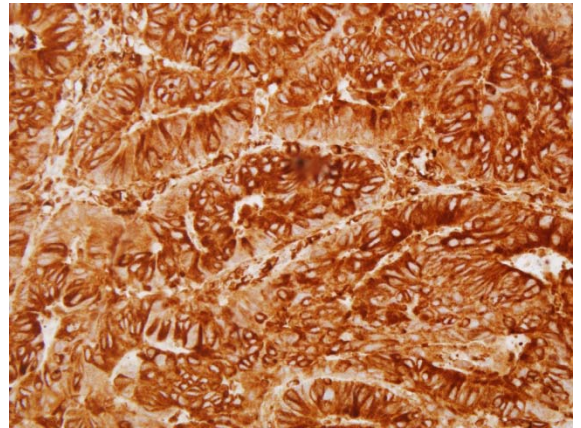
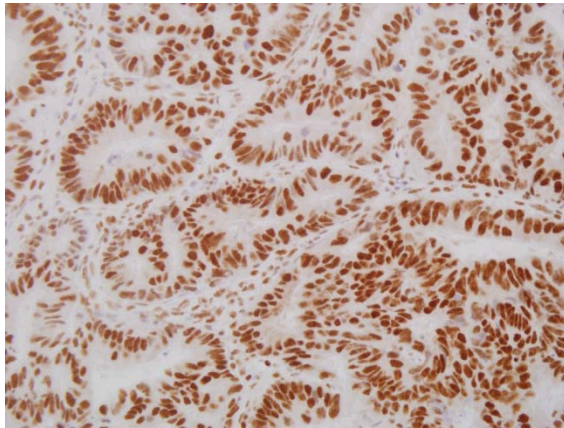
STAG2

α -tubulin

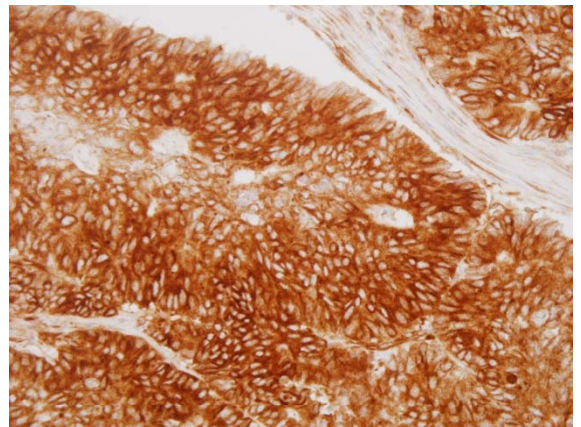
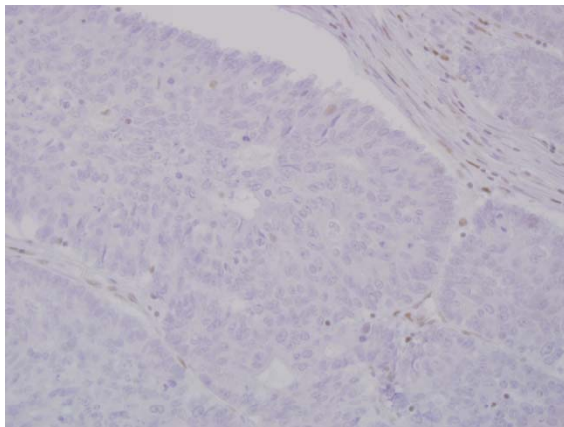
CRC AD3
STAG2 (+)



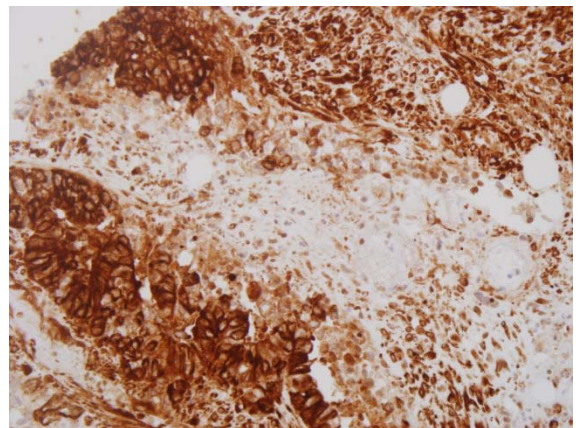
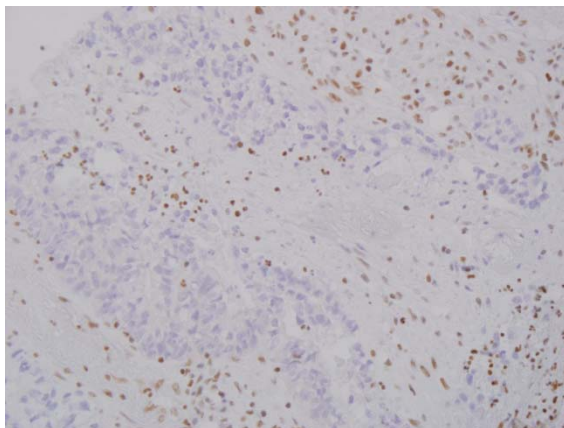
CRC DB7
STAG2 (+)



CRC CD1
STAG2 (-)

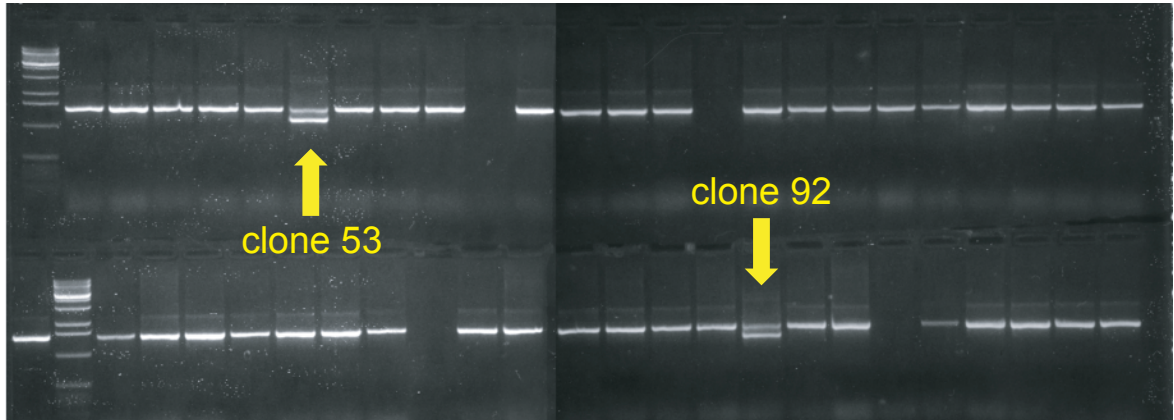


CRC DA7
STAG2 (-)



A

PCR screen of candidate 42MGBA STAG2 knock-in clones



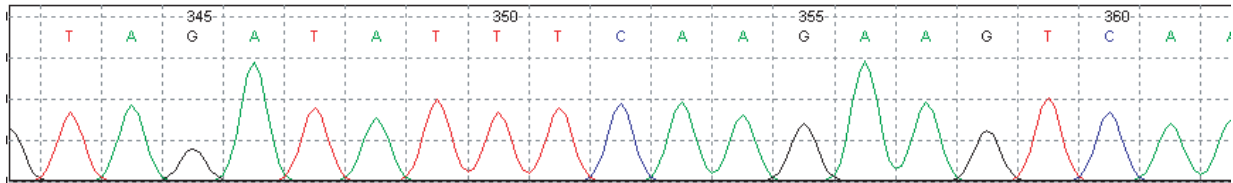
B

amino acid translation

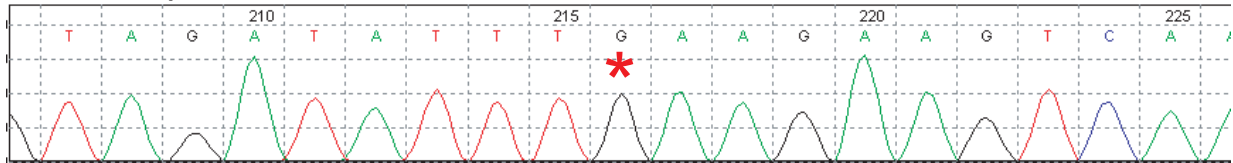
Reference
42MGBA

650								655	
V	D	I	S	R	S			S	Q
V	D	I	X	R				S	Q

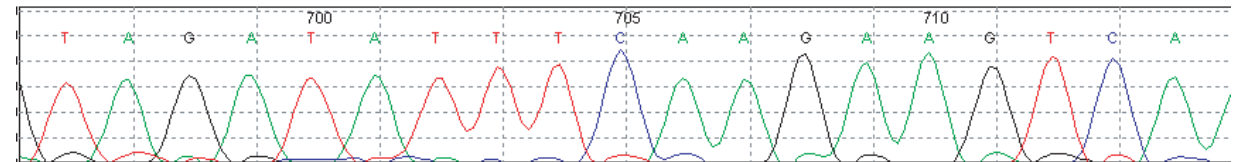
Reference



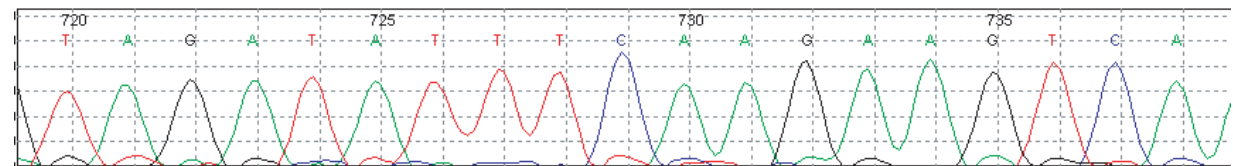
42MGBA parental cells



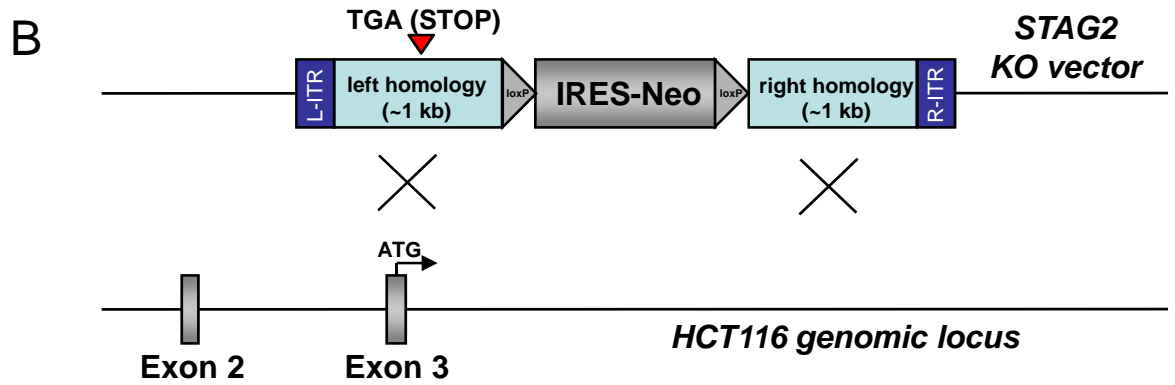
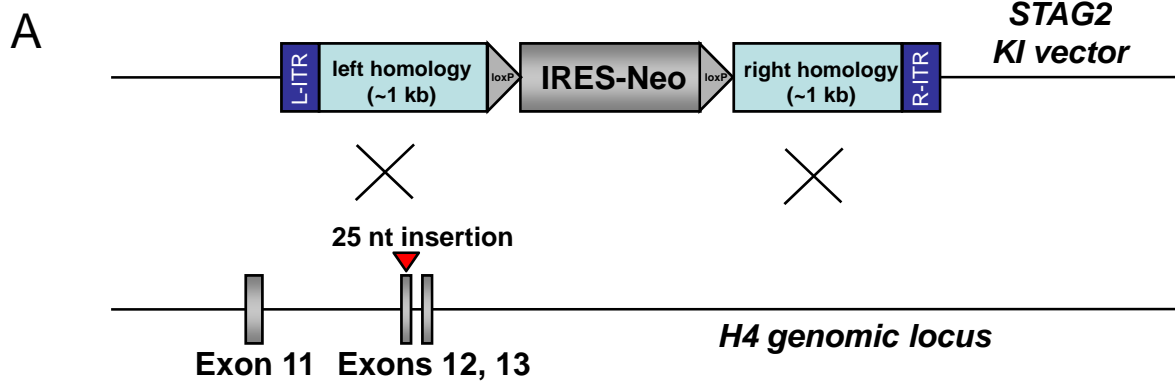
42MGBA STAG2 KI clone 53

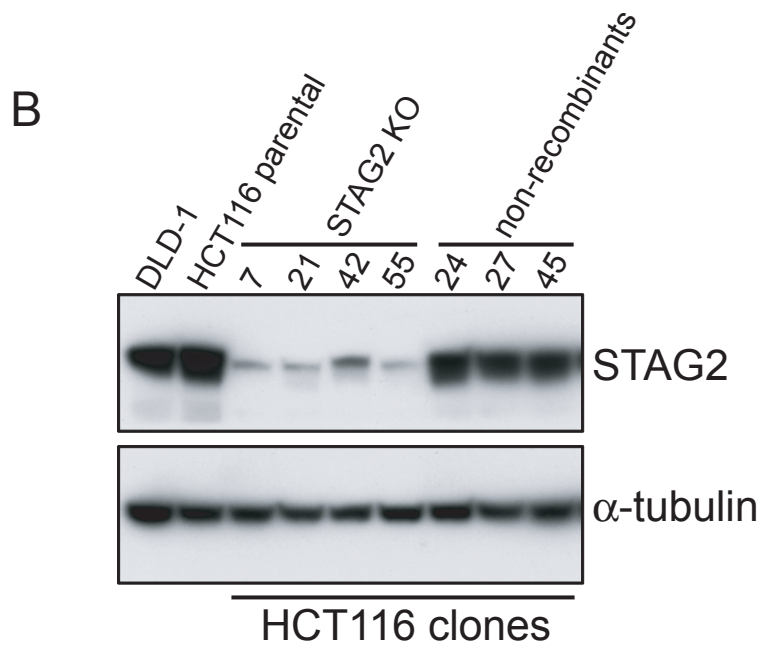
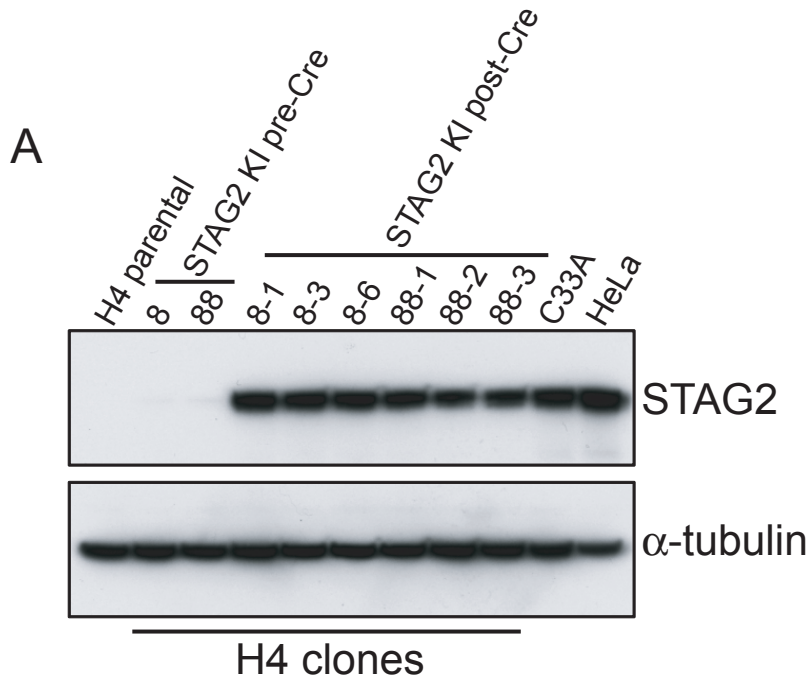


42MGBA STAG2 KI clone 92

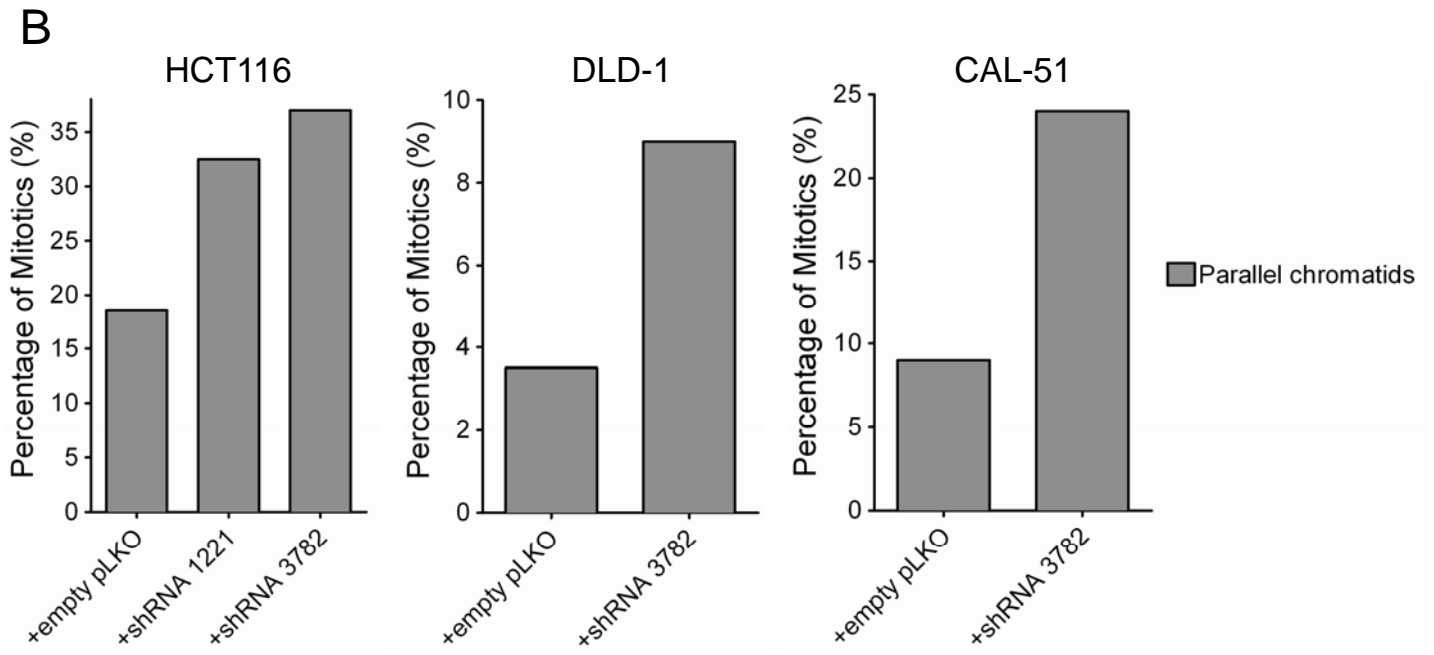
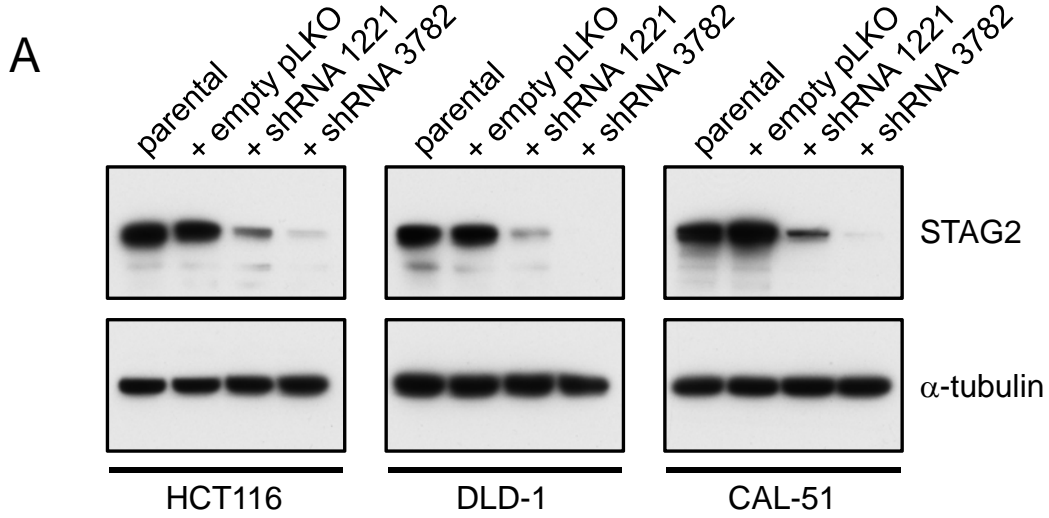


Supplementary Figure 25

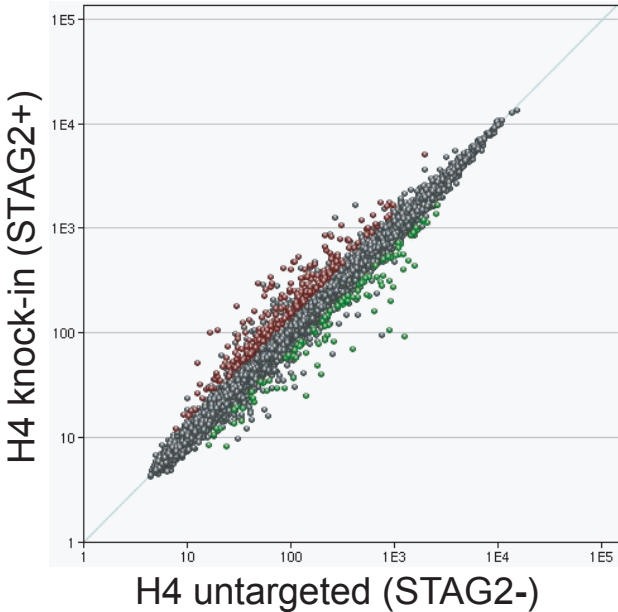




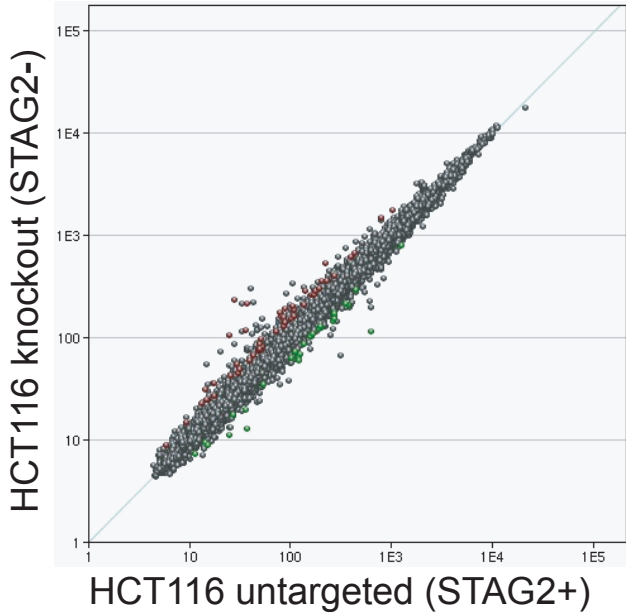
Supplementary Figure 27



A



B



Supplementary Table 3

Group 1: H4 parental cells and non-recombinant clones 10 and 12

Group 2: H4 STAG2 knock-in clones 8-1, 8-3, and 88-1

Statistics: t-test

Correction: Benjamini and Hochberg

Data Transformation: Log Transformed

Grp1 Mean	Grp1 SEM	Grp2 Mean	Grp2 SEM	Ratio	Direction	p-value	Gene ID	Gene Name
10.2712	0.3675	6.5456	0.3165	13.23	Down	0.002	MMP3	Matrix metalloproteinase 3 (stromelysin 1, progelatinase)
9.7974	0.2751	6.7493	0.1257	8.27	Down	0.001	ST8SIA4	ST8 alpha-N-acetyl-neuraminide alpha-2,8-sialyltransferase 4
5.5683	0.1801	8.2272	0.1509	6.32	Up	0.000	FRMD4B	FERM domain containing 4B
4.8819	0.4679	7.4870	0.2946	6.08	Up	0.009	FAP	Fibroblast activation protein, alpha
4.0628	0.1991	6.6555	0.6868	6.03	Up	0.022	TAC1	Tachykinin, precursor 1
4.2749	0.1639	6.7521	0.3655	5.57	Up	0.003	DCN	Decorin
8.6153	0.8492	6.1471	0.1015	5.53	Down	0.045	OR51B4	Olfactory receptor, family 51, subfamily B, member 4
7.1050	0.3730	4.6572	0.2281	5.46	Down	0.005	RGS18	Regulator of G-protein signaling 18
5.9822	0.5267	8.4280	0.0463	5.45	Up	0.010	DAPK1	Death-associated protein kinase 1
7.6110	0.2287	5.3149	0.1626	4.91	Down	0.001	CYB5A	Cytochrome b5 type A (microsomal)
6.4001	0.5292	8.6927	0.4043	4.90	Up	0.026	AMTN	Amelotin
6.0177	0.5928	8.2370	0.1396	4.66	Up	0.022	GABRQ	Gamma-aminobutyric acid (GABA) receptor, theta
6.8620	0.4401	9.0668	0.1181	4.61	Up	0.008	LEPREL1	Leprecan-like 1
6.7176	0.1232	8.9105	0.0206	4.57	Up	0.000	STAG2	Stromal antigen 2
5.8429	0.4912	8.0132	0.1146	4.50	Up	0.013	ANK3	Ankyrin 3, node of Ranvier (ankyrin G)
9.8246	0.4899	7.6652	0.2323	4.47	Down	0.016	ADAMTS19	ADAM metalloproteinase with thrombospondin type 1 motif, 19
6.7761	0.4615	8.9092	0.1903	4.39	Up	0.013	MGP	Matrix Gla protein
5.9754	0.3864	8.0889	0.4034	4.33	Up	0.019	SRGN	Serglycin
3.6503	0.0985	5.6848	0.3286	4.10	Up	0.004	-	
5.7741	0.3952	7.8069	0.3620	4.09	Up	0.019	MME	Membrane metallo-endopeptidase
6.6259	0.2985	8.6509	0.1496	4.07	Up	0.004	LPAR1	Lysophosphatidic acid receptor 1
7.7160	0.2965	9.7379	0.1819	4.06	Up	0.004	DNER	Delta/notch-like EGF repeat containing
9.3063	0.3424	7.3361	0.4572	3.92	Down	0.026	PTGS2	Prostaglandin-endoperoxide synthase 2 (prostaglandin G/H synthase)
5.1012	0.4226	6.9820	0.0511	3.68	Up	0.012	PREX2	Phosphatidylinositol-3,4,5-trisphosphate-dependent Rac exchange factor 2
5.4503	0.5498	7.3222	0.1496	3.66	Up	0.030	EPB41L3	Erythrocyte membrane protein band 4.1-like 3
7.4863	0.3523	5.6156	0.1405	3.66	Down	0.008	CDH7	Cadherin 7, type 2
8.2359	0.3763	10.0819	0.0660	3.60	Up	0.008	CD24	CD24 molecule
10.5931	0.3318	8.7751	0.1800	3.53	Down	0.009	TXNIP	Thioredoxin interacting protein
9.9060	0.3948	8.1060	0.0619	3.48	Down	0.011	SEMA3D	Semaphorin 3D
7.9164	0.3761	9.7034	0.2032	3.45	Up	0.014	ALDH1A3	Aldehyde dehydrogenase 1 family, member A3
5.3140	0.3832	7.0540	0.4864	3.34	Up	0.048	-	Gamma-aminobutyric acid (GABA) A receptor, epsilon
8.0258	0.1959	6.3615	0.2293	3.17	Down	0.005	AOAH	Acyloxyacyl hydrolase (neutrophil)
7.7192	0.0992	9.3762	0.0779	3.15	Up	0.000	TNFRSF21	Tumor necrosis factor receptor superfamily, member 21
4.9307	0.3210	6.5731	0.2368	3.12	Up	0.015	SCN3A	Sodium channel, voltage-gated, type III, alpha subunit
4.6102	0.3729	6.2208	0.2955	3.05	Up	0.028	C7orf69	Chromosome 7 open reading frame 69
7.0668	0.5354	8.6585	0.1891	3.01	Up	0.049	TOX	Thymocyte selection-associated high mobility group box

Ontologies

proteolysis
protein amino acid glycosylation

biopolymer catabolic process
positive regulation of acute inflammatory response, natriuresis
organ morphogenesis, peptide cross-linking via chondroitin 4-sulfate glycosaminoglycan
G-protein coupled receptor protein signaling pathway
regulation of G-protein coupled receptor protein signaling pathway
protein kinase, anti-apoptosis
electron transport chain
cell adhesion, biomineral formation
ion transport
oxidation reduction

cell cycle, chromosome segregation

signal transduction, establishment of protein localization
proteolysis
cartilage condensation
negative regulation of bone mineralization

proteolysis
G-protein coupled receptor protein signaling pathway
neuron migration
fatty acid biosynthetic process
G-protein coupled receptor protein signaling pathway
cortical actin cytoskeleton organization
homophilic cell adhesion
response to hypoxia
response to oxidative stress
nervous system development
kidney development, optic cup morphogenesis
ion transport, GABA signaling pathway
lipid metabolic process, inflammatory response
apoptosis, signal transduction
sodium ion transport

DNA binding

Supplementary Table 4

Group 1: 42MGBA parental cells and pre-Cre clones 53 and 92

Group 2: 42MGBA STAG2 knock-in clones 53-1, 53-7, and 92-6

Statistics: t-test

Correction: Benjamini and Hochberg

Data Transformation: Log Transformed

Grp1 Mean	Grp1 SEM	Grp2 Mean	Grp2 SEM	Ratio	Direction	p-value	Gene ID	Gene Name
6.1588	0.3866	7.6770	0.2608	2.86	Up	0.031	ITGA6	Integrin, alpha 6
4.2746	0.3004	5.3110	0.1912	2.05	Up	0.044	KITLG	KIT ligand
4.5495	0.1372	5.4141	0.2706	1.82	Up	0.046	PLCB4	Phospholipase C, beta 4
7.7872	0.2043	6.9765	0.0411	1.75	Down	0.018	BDKRB1	Bradykinin receptor B1
4.4900	0.2242	5.2741	0.0829	1.72	Up	0.030	CARD16	Caspase recruitment domain family, member 16
6.2648	0.2173	7.0278	0.1582	1.70	Up	0.047	EPS8	Epidermal growth factor receptor pathway substrate 8
6.2226	0.1259	5.4879	0.0834	1.66	Down	0.008	-	ncrna: ENSG00000210467
6.6446	0.0747	5.9433	0.2342	1.63	Down	0.046	TSHZ1	Teashirt zinc finger homeobox 1
4.7247	0.2282	4.0496	0.0467	1.60	Down	0.044	NT5E	5-nucleotidase, ecto (CD73)
4.8573	0.0934	5.5255	0.2091	1.59	Up	0.043	-	chromosome 6 open reading frame 155
5.6906	0.1293	6.3526	0.0752	1.58	Up	0.011	UQCRFS1	Ubiquinol-cytochrome c reductase, Rieske iron-sulfur polypeptide 1
4.5136	0.0734	5.1756	0.0836	1.58	Up	0.004	-	
5.7196	0.0943	6.3651	0.1795	1.56	Up	0.033	ELMO1	Engulfment and cell motility 1
7.2171	0.0293	7.8291	0.0759	1.53	Up	0.002	ALDH1L2	Aldehyde dehydrogenase 1 family, member L2
5.9287	0.1098	5.3120	0.0929	1.53	Down	0.013	-	ncrna: ENSG00000199568
7.6471	0.0472	7.0578	0.1564	1.50	Down	0.023	FBLN5	Fibulin 5

Ontologies

cell-matrix adhesion, signal transduction

hematopoiesis, cell survival and proliferation

lipid catabolic process, signal transduction

G-protein coupled receptor, regulation of inflammation and vascular tone

proteolysis, regulation of apoptosis

signal transduction, cell proliferation

regulation of transcription, developmental pattern formation

purine nucleotide biosynthetic process

cellular metabolism, electron transport chain

cell motility, phagocytosis, apoptosis

metabolic process

cell-matrix adhesion

Supplementary Table 5

Group 1: HCT116 STAG2 non-recombinant clones 24 and 27

Group 2: HCT116 STAG2 knockout clones 7 and 21

Statistics: t-test

Correction: Benjamini and Hochberg

Data Transformation: Log Transformed

Grp1 Mean	Grp1 SEM	Grp2 Mean	Grp2 SEM	Ratio	Direction	p-value	Gene ID	Gene Name
4.8069	0.1443	7.8713	0.0645	8.37	Up	0.003	ANGPT2	Angiopoietin 2
5.2230	0.1343	7.7417	0.0497	5.73	Up	0.003	ITGB8	Integrin, beta 8
9.2903	0.0076	6.8549	0.2890	5.41	Down	0.014	STAG2	Stromal antigen 2
4.6207	0.0605	6.7285	0.1329	4.31	Up	0.005	TM4SF18	Transmembrane 4 L six family member 18
5.1775	0.1844	6.8892	0.1114	3.28	Up	0.015	SCML1	Sex comb on midleg-like 1
5.2243	0.1772	3.7052	0.1321	2.87	Down	0.021	-	ncrna: ENSG00000200662
7.7983	0.0275	9.0658	0.1807	2.41	Up	0.020	EGR1	Early growth response 1
6.3049	0.0087	7.4512	0.0886	2.21	Up	0.006	SLCO3A1	Solute carrier organic anion transporter family, member 3A1
4.6207	0.1529	3.4761	0.0503	2.21	Down	0.019	-	ncrna: ENSG00000207356
3.8346	0.1619	4.9552	0.1310	2.17	Up	0.033	SLC40A1	Solute carrier family 40, member 1
6.4773	0.1765	7.5855	0.1829	2.16	Up	0.049	C4orf34	Chromosome 4 open reading frame 34
7.1029	0.0904	8.1371	0.0864	2.05	Up	0.014	TP53INP1	Tumor protein p53 inducible nuclear protein 1
4.1376	0.0279	5.1599	0.1105	2.03	Up	0.012	RASGRP1	RAS guanyl releasing protein 1
6.9081	0.2230	5.8948	0.0487	2.02	Down	0.047	-	zinc finger protein 487
6.3336	0.0267	7.3363	0.1681	2.00	Up	0.028	DAPK1	Death-associated protein kinase 1

Ontologies

signal transduction, negative regulator of angiogenesis

ganglioside metabolic process, cell-matrix adhesion

cell cycle, chromosome segregation

membrane function

anatomical structure morphogenesis, transcriptional regulation

negative regulation of transcription from RNA polymerase II promoter

ion transport

iron transport and homeostasis

protein binding, membrane component

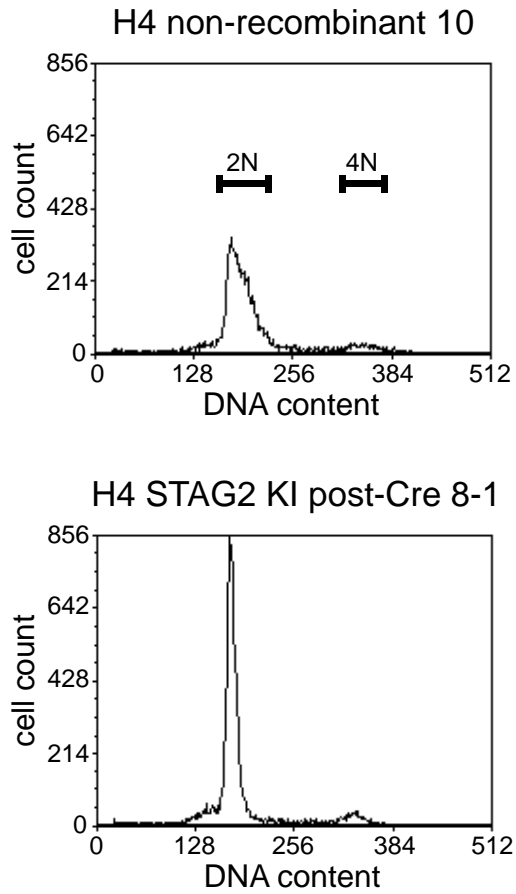
induction of apoptosis, cell cycle arrest

Ras protein signal transduction, cell differentiation

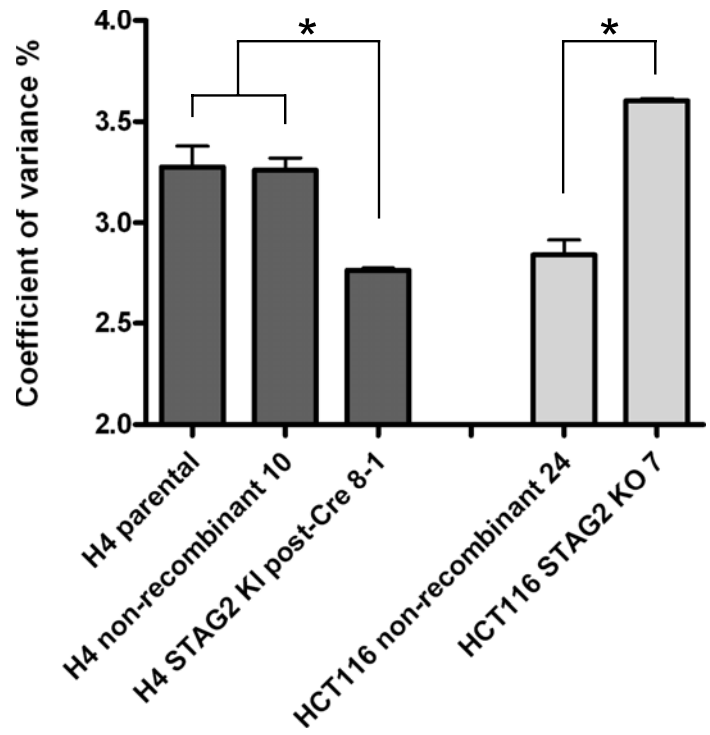
protein kinase, anti-apoptosis

Supplementary Figure 29

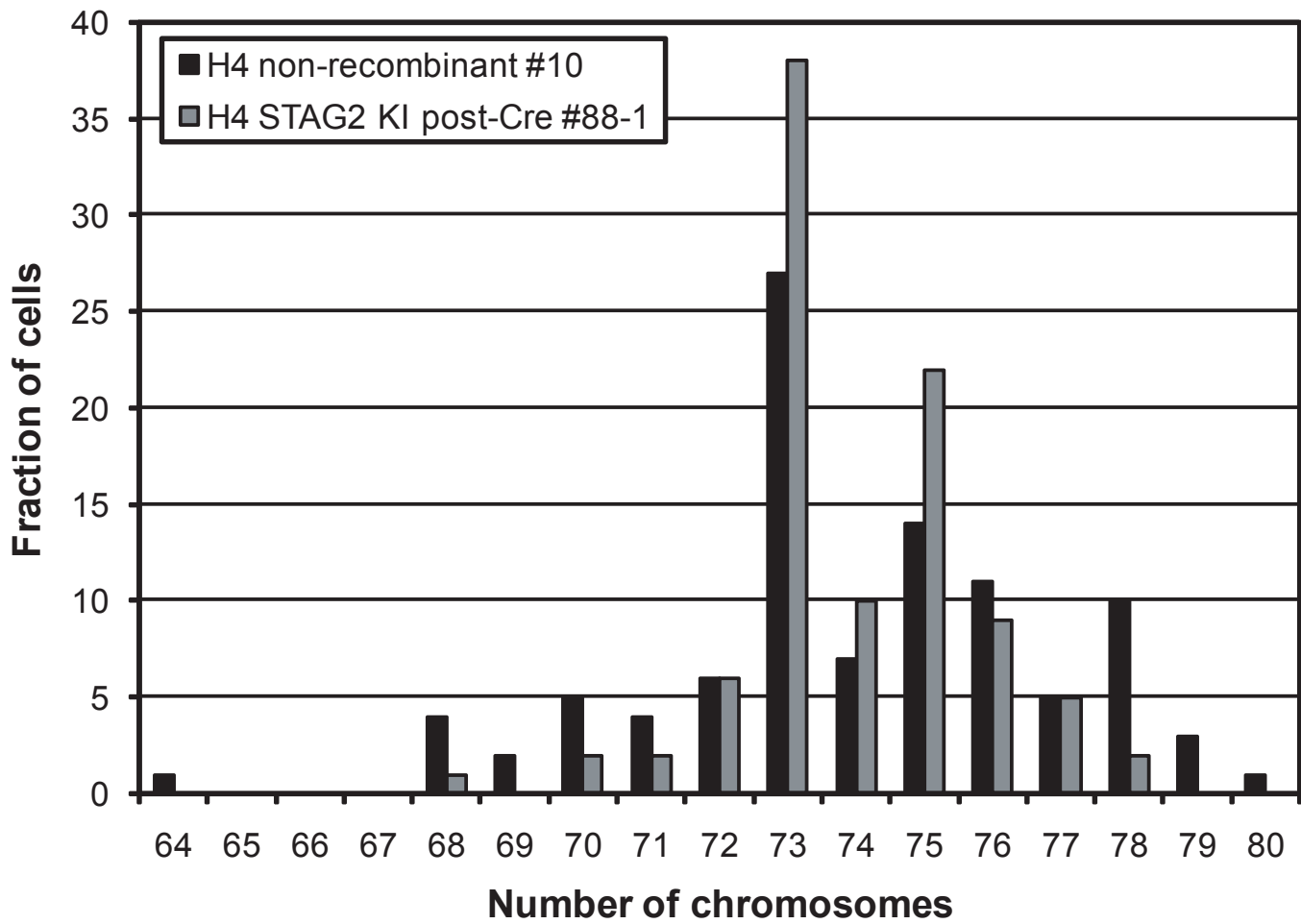
A



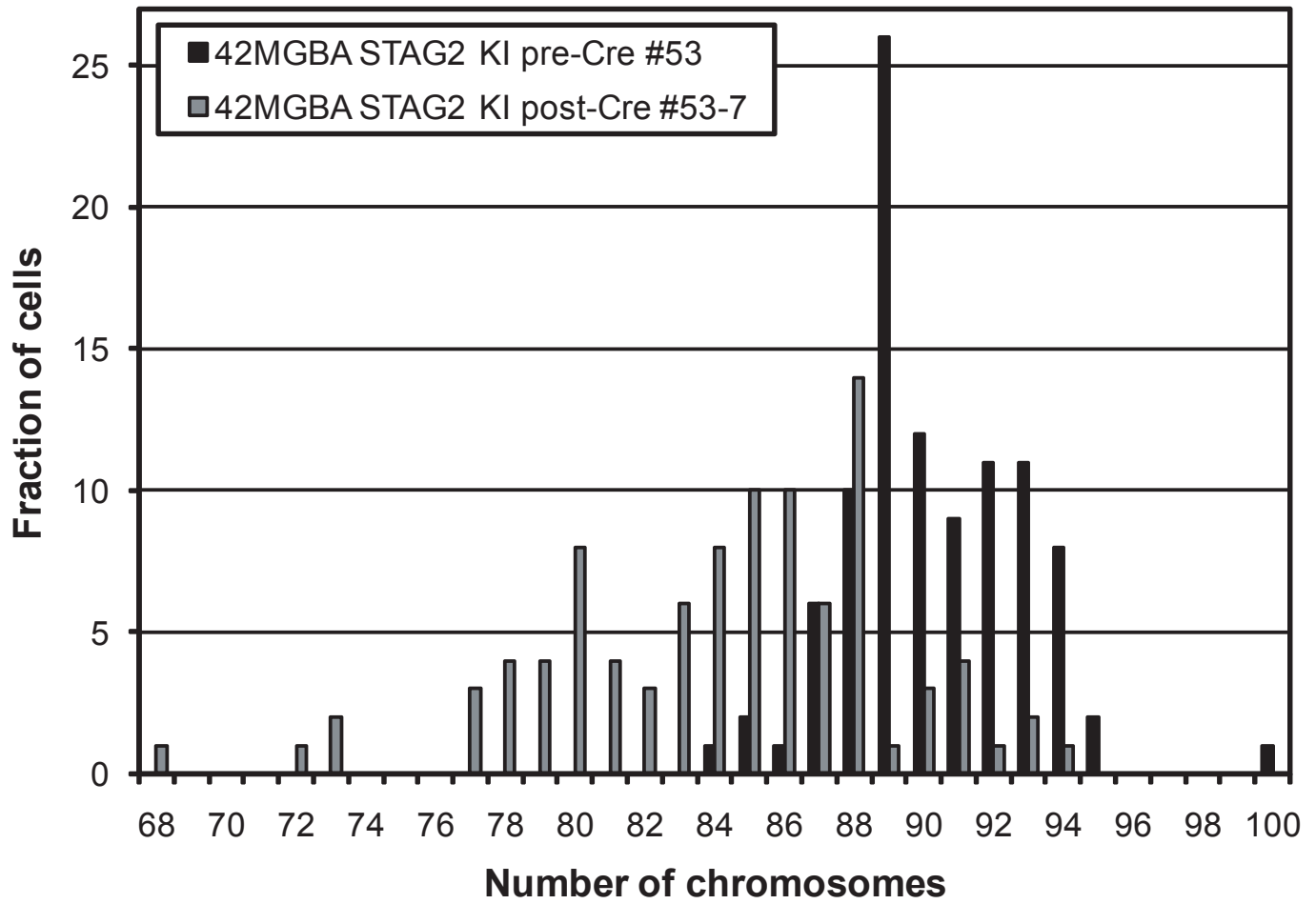
B



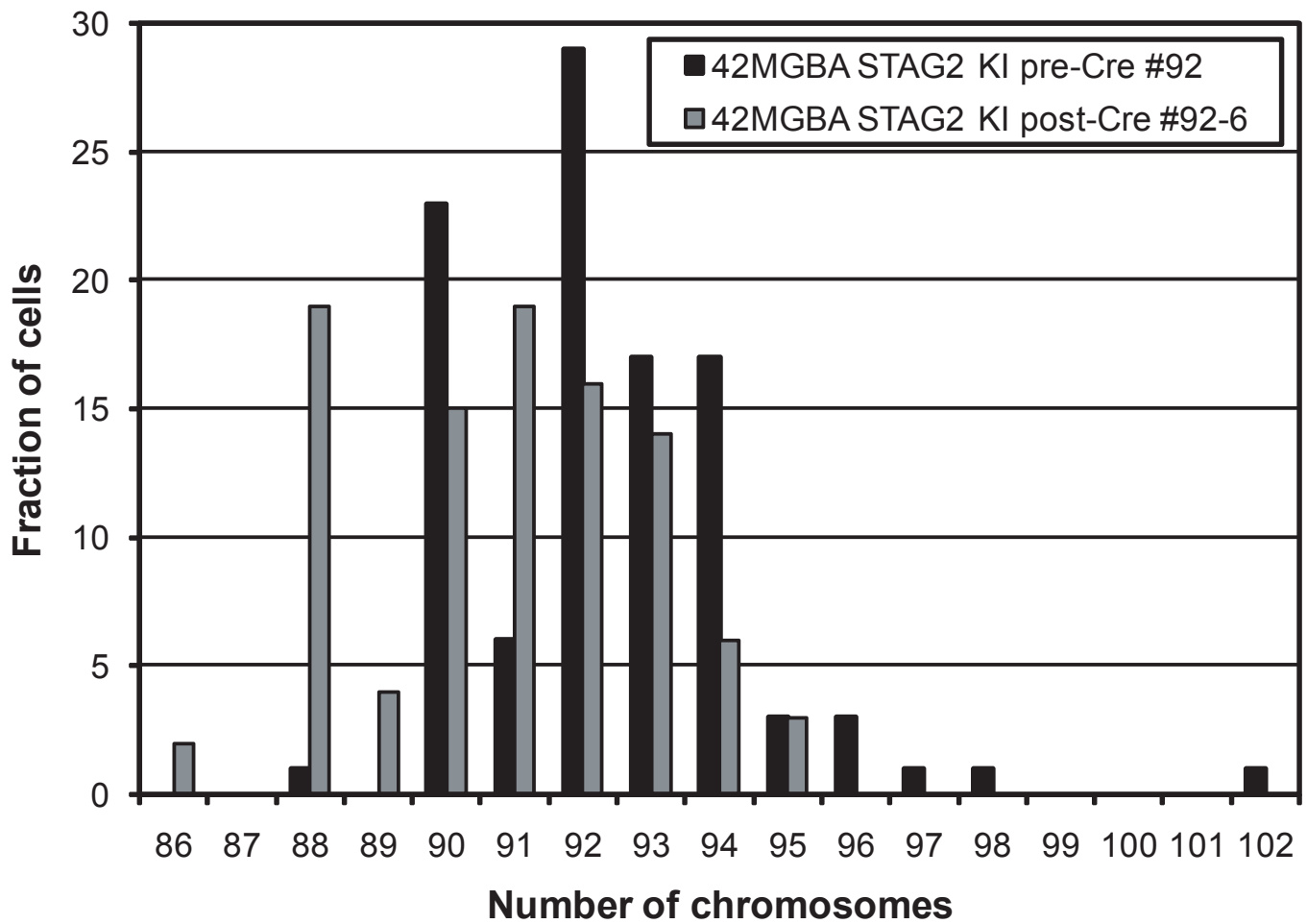
Supplementary Figure 30A



Cell line	# of cells counted	Range of chromosomes per cell	Mean #	Average variation from mean #	<i>p</i> value
H4 non-recombinant 10	100	64-80	74.0	2.3	<0.0001
H4 STAG2 KI post-Cre 88-1	100	68-78	73.9	1.4	

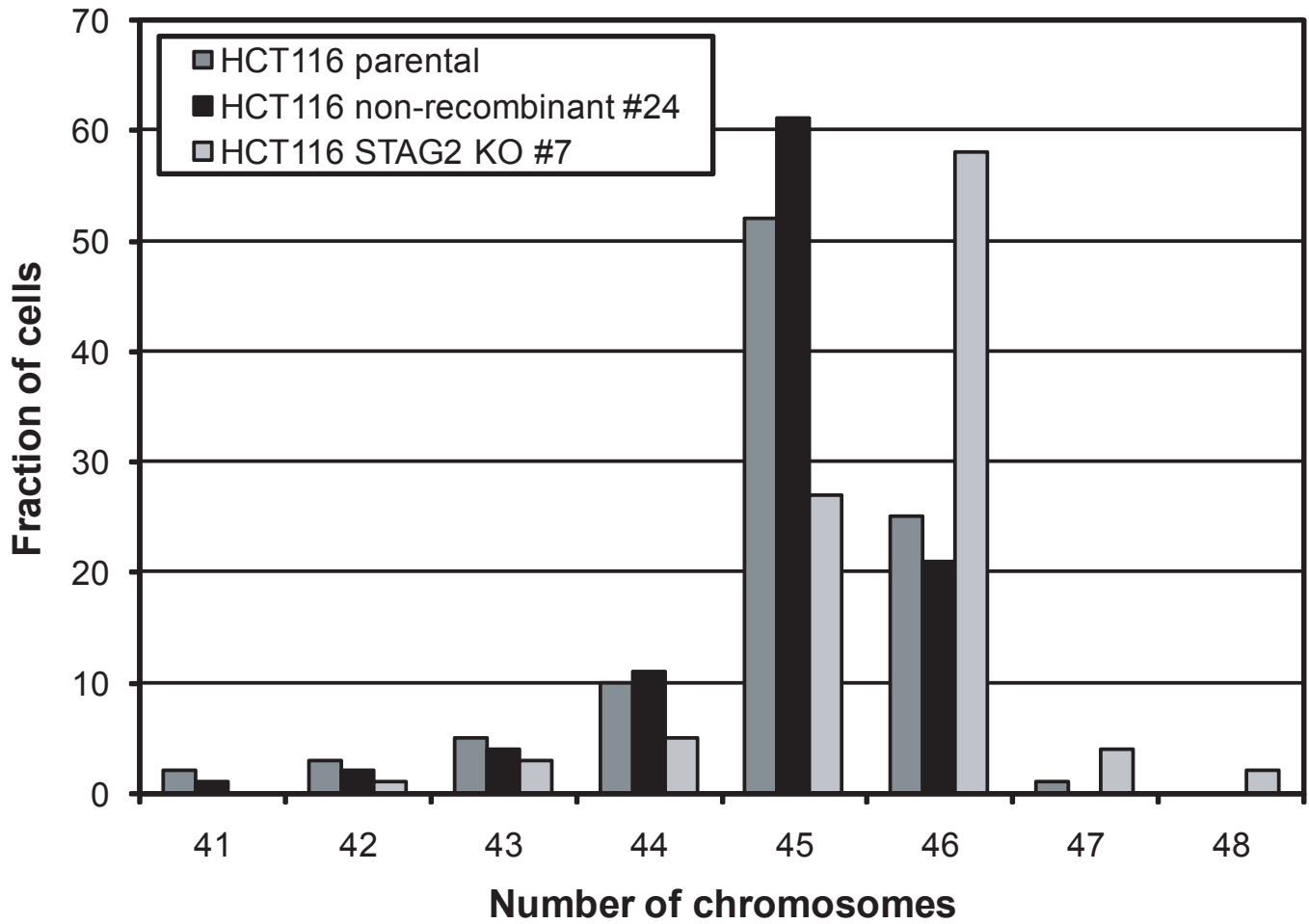


Cell line	# of cells counted	Range of chromosomes per cell	Mean #	<i>p</i> value
42MGBA STAG2 KI pre-Cre 53	100	84-100	90.3	<0.0001
42MGBA STAG2 KI post-Cre 53-7	100	68-94	84.2	



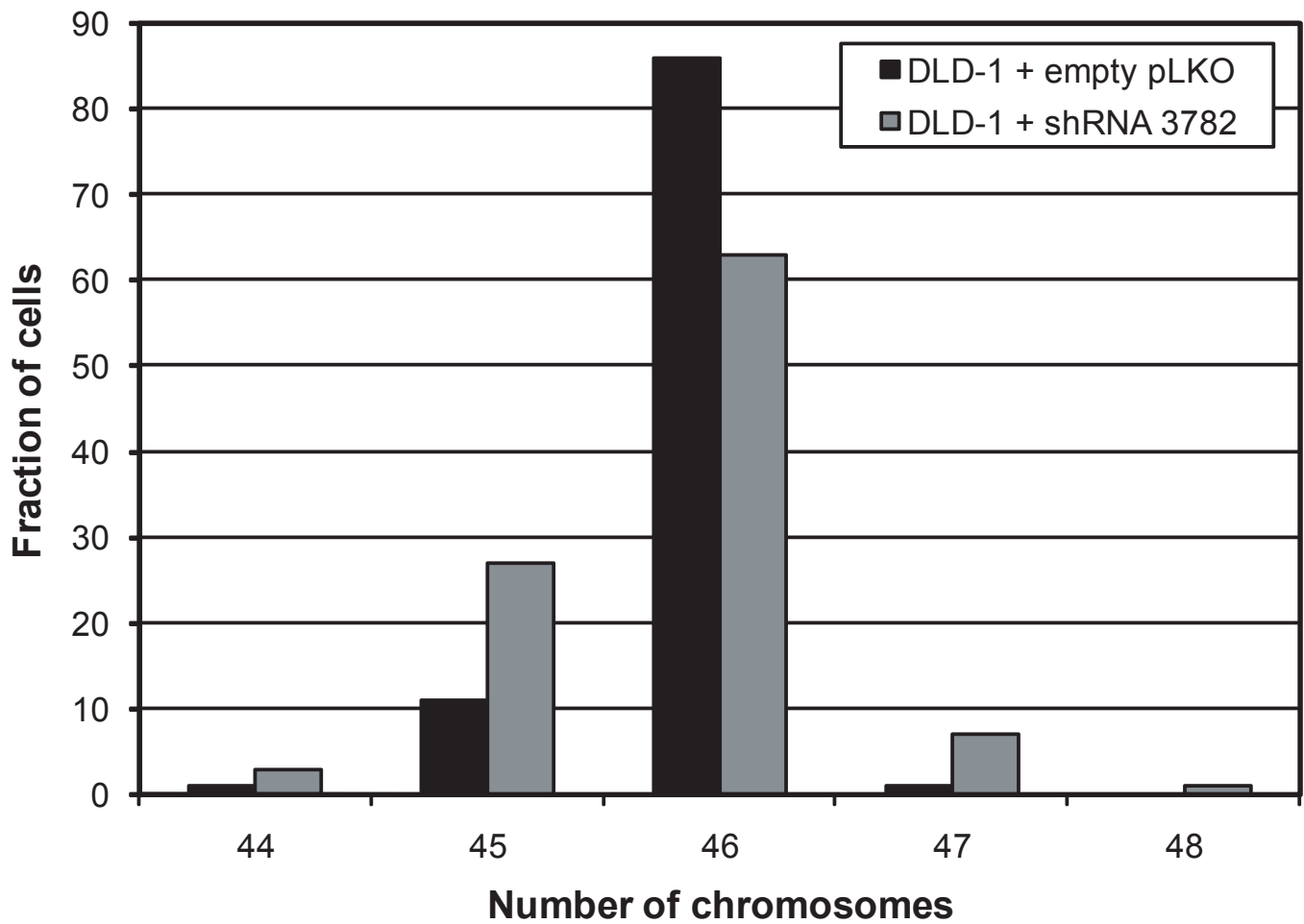
Cell line	# of cells counted	Range of chromosomes per cell	Mean #	<i>p</i> value
42MGBA STAG2 KI pre-Cre 92	100	88-102	92.4	<0.0001
42MGBA STAG2 KI post-Cre 92-6	100	86-95	90.8	

Supplementary Figure 30D



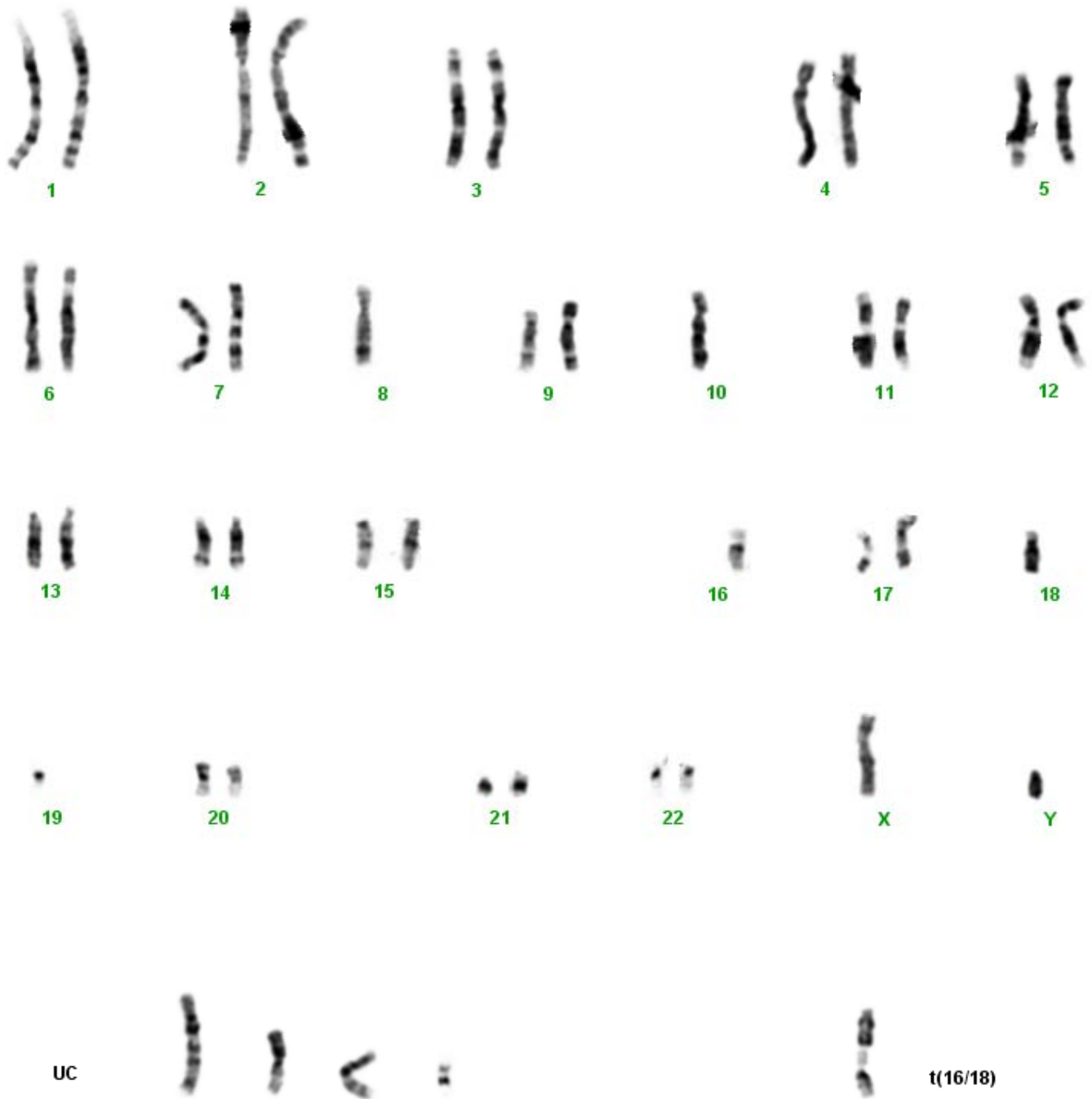
Cell line	# of cells counted	Range of chromosomes per cell	Modal #	Mean #	<i>p</i> value
HCT116 parental	100	41-47	45	44.9	-
HCT116 non-recombinant 24	200	41-46	45	45.1	<0.0001
HCT116 STAG2 KO 7	200	42-48	46	45.8	

Supplementary Figure 30E



Cell line	# of cells counted	Range of chromosomes per cell	Mean #	Average variation from mean #	<i>p</i> value
DLD-1 + empty pLKO	100	44-47	45.9	0.23	<0.0001
DLD-1 + shRNA 3782	100	44-48	45.8	0.51	

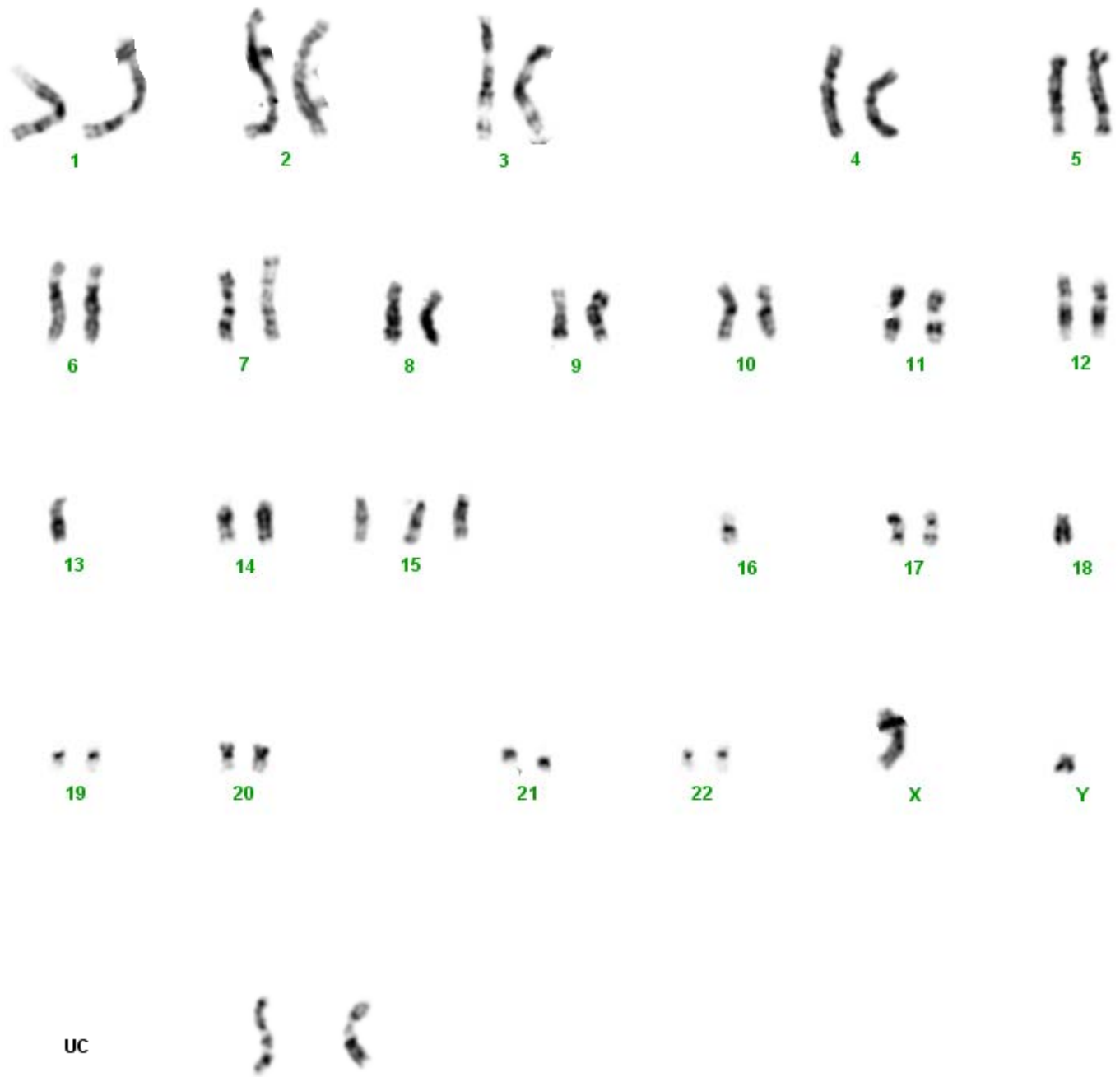
Supplementary Figure 31A



Supplementary Figure 31B



Supplementary Figure 31C



Supplementary Table 6

Primers for sequencing coding exons of STAG2 gene^{*,#}

Exon #	Forward primer	Reverse primer
3	M13F-GCACTGGGGAATTTAACTTTTG	CAGAGCCTTGATGAGTGCTG
4	M13F-TCTTGTGTGTTTGGTAACGTGC	GCTTACCATACCAATCAGCTCC
5	M13F-GGACACCACAAAGAGGCTGT	TGCAATTAGAAAAATCAGAGCTACA
6	TTGACTTCCATAGTTTCCACATTC	M13F-AAAGTGCTAACAACATCTCTTTAGGTG
7	AGTAAAGTGAGTCAGGTAGAAATGGC	M13F-CATGCCCAGCCTAATGCTTAC
8	M13F-GGATTTATTGGAGAAGAAAGGTGAG	AATTCGCAGGAGGGATGG
9	M13F-CATTTGTAGCAGCTGCATCTTTT	TGTTGGGCAAATAGTTTGAAATG
10	CCAATCAAATATTTTCAAGGTATTAAGGG	M13F-TGACTCAGTGGCACTAATGGAG
11	GTGAGCAAAGGCTGGGATATG	M13F-GGAGGCTTCCAGAAATGTGTC
12	TCTGAAGGAATGCTATGGTATGAAA	M13F-TGTCAAGGGTCATAGACACAATTC
13	TTTACCAGTCGGTTCAAGGTTAG	M13F-TTCTATGGTTCCTTCTTCCTGTG
14	GGACGTTACTAAAAGCACCTGTT	M13F-CCCAGCCTACATTTCCCTTT
15	TGTGCCATGTTGGATGATATTG	M13F-GGGTGGCTCTCCATTCTATTG
16	GCAAGCAAATAAGGCAGTTTC	M13F-ATAAAGAATGTTGACAGCAATTACATC
17	GGCAGATTCTGTTTACAGGCAG	M13F-TCAAATTTCTCAAATTGCTAATGC
18	ACCATCTGAAGGTAGAGTTGGTTAG	M13F-AAAGCATTATAATATTCTGTGAGGCA
19	M13F-TGGCCCTTCTCAGTTATTAGC	CAAAGGGAAGCATCATTACCG
20	M13F-CCATGGTGGTATGGTCATGTAG	CTGCTAGGGACTATCACCAAGAC
21	M13F-CCCAGCCATATTGCCTTAAAT	CCCACAACGACAACAACAAT
22	CGTTGTGGGGGCATTTTA	M13F-GCAAGTTGCCAAAGGATTACA
23	M13F-AAATGGAGACATGCCTGAGC	AACCACAGATTATGCCACCTTC
24	TTAAGGCTGCAATTTGGTGAG	M13F-CAAGATATTTCTGCTTTGCTCAAT
25	GCCTTATACAAATATAAGCATTTCGTTG	M13F-GCTGGAATATATACCTGTGTTTCACG
26	TGGAGTGATTAGTTCCATTTG	M13F-CCTTAAAGAATTCAATGGCAGC
27	M13F-GGTTTCAGTAACATTCTTTCCTGC	ACTTTGCCCAATTTCAACTGC
28	M13F-CAGTGCCTCATTATTGAACACC	AATTGAGATAGCACTGTAAGTGGTTC
29	GCTTGGCAAAGGAAGTAGTGAG	M13F-AATGCAATCCTACAATTCTGTGTG
30	M13F-ATGCCTATGCTCGCACAATA	TTTGTAAGCTATTATTGAACACATCTCA
31	M13F-CAGGGACTGCCCTTACATA	TTGCCTTGCTTCCTCTTGTT
32	M13F-TCCAATGCAGACTGAACATCA	TGCTTTTCTGTTGGAAAGACC
33	M13F-AGAGAGCCACATACTGCTGCC	GGATCTACCACCTTCACCAACC
34	TGTGTCAGGTACACTTGAATCAC	M13F-CCTCCCCTGAAATCCTGC
35	TGAGGTAAGTAGCATCTTGATTAGTCC	M13F-CCTCAATGCACTTGATCTTGG

*The exon numbering is annotated according to ENSEMBL transcript ENST00000218089.

#M13F denotes the universal sequencing primer, 5'-GTAAAACGACGGCCAGT-3'

References and Notes

1. D. Hanahan, R. A. Weinberg, Hallmarks of cancer: The next generation. *Cell* **144**, 646 (2011). [doi:10.1016/j.cell.2011.02.013](https://doi.org/10.1016/j.cell.2011.02.013) [Medline](#)
2. C. Lengauer, K. W. Kinzler, B. Vogelstein, Genetic instabilities in human cancers. *Nature* **396**, 643 (1998). [doi:10.1038/25292](https://doi.org/10.1038/25292) [Medline](#)
3. L. A. Loeb, Mutator phenotype may be required for multistage carcinogenesis. *Cancer Res.* **51**, 3075 (1991). [Medline](#)
4. D. P. Cahill *et al.*, Mutations of mitotic checkpoint genes in human cancers. *Nature* **392**, 300 (1998). [doi:10.1038/32688](https://doi.org/10.1038/32688) [Medline](#)
5. K. Nasmyth, Segregating sister genomes: The molecular biology of chromosome separation. *Science* **297**, 559 (2002). [doi:10.1126/science.1074757](https://doi.org/10.1126/science.1074757) [Medline](#)
6. D. A. Solomon *et al.*, Identification of p18^{INK4c} as a tumor suppressor gene in glioblastoma multiforme. *Cancer Res.* **68**, 2564 (2008). [doi:10.1158/0008-5472.CAN-07-6388](https://doi.org/10.1158/0008-5472.CAN-07-6388) [Medline](#)
7. D. A. Solomon *et al.*, Mutational inactivation of PTPRD in glioblastoma multiforme and malignant melanoma. *Cancer Res.* **68**, 10300 (2008). [doi:10.1158/0008-5472.CAN-08-3272](https://doi.org/10.1158/0008-5472.CAN-08-3272) [Medline](#)
8. Materials and methods are available as supporting material on *Science Online*.
9. I. Sumara, E. Vorlaufer, C. Gieffers, B. H. Peters, J. M. Peters, Characterization of vertebrate cohesin complexes and their regulation in prophase. *J. Cell Biol.* **151**, 749 (2000). [doi:10.1083/jcb.151.4.749](https://doi.org/10.1083/jcb.151.4.749) [Medline](#)
10. C. H. Haering, A. M. Farcas, P. Arumugam, J. Metson, K. Nasmyth, The cohesin ring concatenates sister DNA molecules. *Nature* **454**, 297 (2008). [doi:10.1038/nature07098](https://doi.org/10.1038/nature07098) [Medline](#)
11. M. J. Walter *et al.*, Acquired copy number alterations in adult acute myeloid leukemia genomes. *Proc. Natl. Acad. Sci. U.S.A.* **106**, 12950 (2009). [doi:10.1073/pnas.0903091106](https://doi.org/10.1073/pnas.0903091106) [Medline](#)
12. K. L. Goringe *et al.*, Are there any more ovarian tumor suppressor genes? A new perspective using ultra high-resolution copy number and loss of heterozygosity analysis. *Genes Chromosomes Cancer* **48**, 931 (2009). [doi:10.1002/gcc.20694](https://doi.org/10.1002/gcc.20694) [Medline](#)
13. J. Rocquain *et al.*, Alteration of cohesin genes in myeloid diseases. *Am. J. Hematol.* **85**, 717 (2010). [doi:10.1002/ajh.21798](https://doi.org/10.1002/ajh.21798) [Medline](#)
14. J. S. Kim, C. Bonifant, F. Bunz, W. S. Lane, T. Waldman, Epitope tagging of endogenous genes in diverse human cell lines. *Nucleic Acids Res.* **36**, e127 (2008). [doi:10.1093/nar/gkn566](https://doi.org/10.1093/nar/gkn566) [Medline](#)
15. E. Lara-Pezzi *et al.*, Evidence of a transcriptional co-activator function of cohesin STAG/SA/Scc3. *J. Biol. Chem.* **279**, 6553 (2004). [doi:10.1074/jbc.M307663200](https://doi.org/10.1074/jbc.M307663200) [Medline](#)
16. K. S. Wendt *et al.*, Cohesin mediates transcriptional insulation by CCCTC-binding factor. *Nature* **451**, 796 (2008). [doi:10.1038/nature06634](https://doi.org/10.1038/nature06634) [Medline](#)

17. M. H. Kagey *et al.*, Mediator and cohesin connect gene expression and chromatin architecture. *Nature* **467**, 430 (2010). [doi:10.1038/nature09380](https://doi.org/10.1038/nature09380) [Medline](#)
18. N. Zhang *et al.*, Overexpression of Separase induces aneuploidy and mammary tumorigenesis. *Proc. Natl. Acad. Sci. U.S.A.* **105**, 13033 (2008). [doi:10.1073/pnas.0801610105](https://doi.org/10.1073/pnas.0801610105) [Medline](#)
19. D. J. Baker, F. Jin, K. B. Jeganathan, J. M. van Deursen, Whole chromosome instability caused by Bub1 insufficiency drives tumorigenesis through tumor suppressor gene loss of heterozygosity. *Cancer Cell* **16**, 475 (2009). [doi:10.1016/j.ccr.2009.10.023](https://doi.org/10.1016/j.ccr.2009.10.023) [Medline](#)
20. P. V. Jallepalli *et al.*, Securin is required for chromosomal stability in human cells. *Cell* **105**, 445 (2001). [doi:10.1016/S0092-8674\(01\)00340-3](https://doi.org/10.1016/S0092-8674(01)00340-3) [Medline](#)
21. R. Sotillo *et al.*, Mad2 overexpression promotes aneuploidy and tumorigenesis in mice. *Cancer Cell* **11**, 9 (2007). [doi:10.1016/j.ccr.2006.10.019](https://doi.org/10.1016/j.ccr.2006.10.019) [Medline](#)
22. H. Rajagopalan *et al.*, Inactivation of hCDC4 can cause chromosomal instability. *Nature* **428**, 77 (2004). [doi:10.1038/nature02313](https://doi.org/10.1038/nature02313) [Medline](#)
23. Z. Wang *et al.*, Three classes of genes mutated in colorectal cancers with chromosomal instability. *Cancer Res.* **64**, 2998 (2004). [doi:10.1158/0008-5472.CAN-04-0587](https://doi.org/10.1158/0008-5472.CAN-04-0587) [Medline](#)
24. T. D. Barber *et al.*, Chromatid cohesion defects may underlie chromosome instability in human colorectal cancers. *Proc. Natl. Acad. Sci. U.S.A.* **105**, 3443 (2008). [doi:10.1073/pnas.0712384105](https://doi.org/10.1073/pnas.0712384105) [Medline](#)
25. K. W. Kinzler, B. Vogelstein, Gatekeepers and caretakers. *Nature* **386**, 761, 763 (1997). [doi:10.1038/386761a0](https://doi.org/10.1038/386761a0) [Medline](#)

Supporting References and Notes

1. A. Pandita, K. D. Aldape, G. Zadeh, A. Guha, C. D. James, Contrasting in vivo and in vitro fates of glioblastoma cell subpopulations with amplified EGFR. *Genes Chromosomes Cancer* **39**, 29 (2004). [doi:10.1002/gcc.10300](https://doi.org/10.1002/gcc.10300) [Medline](#)
2. C. Giannini *et al.*, Patient tumor EGFR and PDGFRA gene amplifications retained in an invasive intracranial xenograft model of glioblastoma multiforme. *Neuro-oncol.* **7**, 164 (2005). [doi:10.1215/S1152851704000821](https://doi.org/10.1215/S1152851704000821) [Medline](#)
3. R. G. W. Verhaak *et al.*, Integrated genomic analysis identifies clinically relevant subtypes of glioblastoma characterized by abnormalities in PDGFRA, IDH1, EGFR, and NF1. *Cancer Cell* **17**, 98 (2010). [doi:10.1016/j.ccr.2009.12.020](https://doi.org/10.1016/j.ccr.2009.12.020) [Medline](#)
4. L. H. Palavalli *et al.*, Analysis of the matrix metalloproteinase family reveals that MMP8 is often mutated in melanoma. *Nat. Genet.* **41**, 518 (2009). [doi:10.1038/ng.340](https://doi.org/10.1038/ng.340) [Medline](#)
5. H. Y. Huang *et al.*, Ewing sarcomas with p53 mutation or p16/p14ARF homozygous deletion: A highly lethal subset associated with poor chemoresponse. *J. Clin. Oncol.* **23**, 548 (2005). [doi:10.1200/JCO.2005.02.081](https://doi.org/10.1200/JCO.2005.02.081) [Medline](#)
6. D. A. Solomon *et al.*, Identification of p18 INK4c as a tumor suppressor gene in glioblastoma multiforme. *Cancer Res.* **68**, 2564 (2008). [doi:10.1158/0008-5472.CAN-07-6388](https://doi.org/10.1158/0008-5472.CAN-07-6388) [Medline](#)

7. D. A. Solomon *et al.*, Mutational inactivation of PTPRD in glioblastoma multiforme and malignant melanoma. *Cancer Res.* **68**, 10300 (2008). [doi:10.1158/0008-5472.CAN-08-3272](https://doi.org/10.1158/0008-5472.CAN-08-3272) [Medline](#)
8. D. A. Solomon *et al.*, Sample type bias in the analysis of cancer genomes. *Cancer Res.* **69**, 5630 (2009). [doi:10.1158/0008-5472.CAN-09-1055](https://doi.org/10.1158/0008-5472.CAN-09-1055) [Medline](#)
9. T. Sjöblom *et al.*, The consensus coding sequences of human breast and colorectal cancers. *Science* **314**, 268 (2006). [doi:10.1126/science.1133427](https://doi.org/10.1126/science.1133427) [Medline](#)
10. D. Douglas *et al.*, BMI-1 promotes Ewing sarcoma tumorigenicity independent of CDKN2A repression. *Cancer Res.* **68**, 6507 (2008). [doi:10.1158/0008-5472.CAN-07-6152](https://doi.org/10.1158/0008-5472.CAN-07-6152) [Medline](#)
11. J. S. Kim, C. Bonifant, F. Bunz, W. S. Lane, T. Waldman, Epitope tagging of endogenous genes in diverse human cell lines. *Nucleic Acids Res.* **36**, e127 (2008) Solomon et al. [doi:10.1093/nar/gkn566](https://doi.org/10.1093/nar/gkn566) [Medline](#)
12. J. F. Giménez-Abián, L. A. Díaz-Martínez, K. G. Wirth, Regulated separation of sister centromeres depends on the spindle assembly checkpoint but not on the anaphase promoting complex/cyclosome. *Cell Cycle* **4**, 1561 (2005). [doi:10.4161/cc.4.11.2146](https://doi.org/10.4161/cc.4.11.2146) [Medline](#)
13. T. Kanda, K. F. Sullivan, G. M. Wahl, Histone-GFP fusion protein enables sensitive analysis of chromosome dynamics in living mammalian cells. *Curr. Biol.* **8**, 377 (1998). [doi:10.1016/S0960-9822\(98\)70156-3](https://doi.org/10.1016/S0960-9822(98)70156-3) [Medline](#)